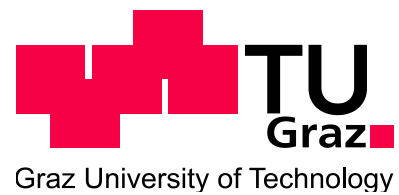


Development and Optimization of Organic – Inorganic Hybrid Nanocomposite Solar Cells

Dissertation



vorgelegt von DI Eugen Maier

an der Technischen Universität Graz

Institut für Chemische Technologie der Materialien (ICTM)

zur Erlangung des akademischen Grades eines Doktors der technischen
Wissenschaften

Graz, Mai 2008

Betreuer: Univ. Doz. DI Dr. Gregor Trimmel

Senat: Ao.Univ.-Prof. Dipl.-Ing. Dr. Robert Saf

Ao.Univ.-Prof. Dipl.-Ing. Dr. Ferdinand Hofer

Acknowledgements

The current work was performed under the supervision of Univ. Doz. DI Dr. Gregor Trimmel and Univ. Prof. DI Dr. Franz Stelzer on the Institute for Chemistry and Technology of Materials (ICTM) at Graz Technical University, who gave me the opportunity to write my thesis on an exciting topic. A big thank you for the friendly supervision and scientific support! An overall compliment to the whole ICTM-crew, I very much enjoyed the open and collegial atmosphere at the institute. In particular I want to thank Thomas Rath for the formidable collaboration from the very beginning and Andi Pein for animating discussions on numerous occasions. It was my pleasure to enjoy the company of Nadja, Luke and Stefan – on the balcony or off it.

Many people contributed to the scientific quality of the work. Special thanks – again - to Thomas Rath, who did all the SEM analyses at Tallin, Robert Saf for carrying out the MS investigations, Martin Schmuck for performing the CV-analyses and Jörg Albering for assistance on the XRD measurements. My gratitude goes to the people of the Resel group at the Institute of Solid State Physics, Oliver Werzer for his support on XRD annealing experiments and Heinz Georg Flesch for his XRR-efforts. Wernfried Haas is acknowledged for permanent endeavor to obtain high-quality TEM results, Martin Tscherner helped us out with our LabView conflicts.

I would also like to express my esteem to the cooperation partners from ISOVOLTA AG, who gratefully financed my research together with FFG. Thanks to Albert Plessing and Andi Ruplitsch for their enduring endorsement for the sake of hybrid solar cells, I also would like to thank Dieter Meissner for his invaluable ideas and suggestions.

Finally I want to state my cordial gratitude to my family and to my friends. Their enduring support and empathy is the basis not just for this work.

Abstract

Development and Optimization of Organic-Inorganic Hybrid Nanocomposite Photovoltaic Devices

The current work deals with the in-situ preparation of organic-inorganic semiconductor composites and their application in hybrid heterojunction photovoltaic devices. Chalcogenide semiconductors are obtained by reaction of metal precursor salts, which are dispersed within a conjugated polymer, with a reactive sulfur species that is obtained by thermal decomposition of a sulfur source. During a moderate annealing step under inert atmosphere the sulfur source is decomposed and the composite layer is obtained. In a second part, stability of organic solar cells was investigated. For this purpose, a multi-channel permanent testing setup was constructed.

Blends of a binary sulfide semiconductor and a conjugated polymer were prepared by thermal decomposition of thiourea. Metal salts of Cd, Pb and Zn, respectively, were dissolved in a solution containing a polythiophene and thiourea. This precursor solution was deposited using wet chemical deposition techniques, upon annealing the composite layer was obtained with networks in the nm-range. Following this approach, composites of poly-3-(ethylbutanoate)thiophene (P3EBT) with CdS, PbS and ZnS, respectively, were obtained. The composite films were tested as the active layer in bulk-heterojunction type hybrid solar cells.

The concept was extended for the formation of ternary semiconductors, CuInS_2 -P3EBT composites were obtained in the described fashion. The system was optimized for the use as active layer in hybrid solar cells. In a further step, quaternary $(\text{ZnS})_{2x}(\text{CuIn})_{1-x}\text{S}_2$ -type acceptor phases were prepared, which effectuated enhanced open circuit voltage in hybrid solar cells. Structural characterization was obtained by XRD and SEM, layer stoichiometry was analyzed using SEM-EDX. A special emphasis in this part was put on the analysis of the annealing process, which was investigated using online-XRD, TGA-MS and FT-IR spectroscopy. Chemical analysis of the decomposition process was performed using mass spectrometry, which revealed the formation of side products.

Stability testing of polymer based solar cells was performed on (1) polymer – PCBM devices and on (2) polymer – CuInS₂ devices using the self-constructed testing setup. Photovoltaic performance was monitored to evaluate the durability of different conjugated polymers. Active layers of PCBM in combination with MEH-PPV, F8T2 and P3HT, respectively, were analyzed in series (1), in series (2) active layers of CuInS₂ in combination with PPV, MEH-PPV, MDMO-PPV and F8T2, respectively, were investigated.

Kurzfassung

Entwicklung und Optimierung von Organisch-Anorganischen Nanokomposit Hybrid solarzellen

Die vorliegende Arbeit behandelt die in-situ Herstellung organisch-anorganischer Halbleiterkomposite sowie deren Anwendung als Aktivschicht in Hybrid-Heterojunction Solarzellen. Chalkogenid-basierende Halbleiter werden durch Reaktion von Metallsalzen, die in einem konjugierten Polymer dispergiert sind, mit thermisch generiertem Schwefel erhalten. Die Thermolyse der Schwefelquelle findet unter Inertbedingungen bei moderaten Temperaturen statt. Der zweite Teil der Arbeit befasst sich mit der Stabilität organischer Solarzellen. Dafür wurde ein Mehrkanal-Dauerteststand errichtet.

Komposite aus binären sulfidischen Halbleitern und konjugierten Polymeren wurden durch thermische Zersetzung von Thioharnstoff generiert. Dabei wurde eine Precursurlösung, die jeweils ein Salz von Cd, Pb oder Zn, ein Polythiophen sowie Thioharnstoff enthielt, nass-chemisch auf geeigneten Substraten aufgebracht. In einem nachfolgenden Heizschritt wurde die anorganische Phase durch aus Thioharnstoff generierten Schwefel gebildet. Derart wurden Komposite aus Poly-3-(ethylbutanoat)thiophen (P3EBT) sowie CdS, PbS oder ZnS erhalten. Mittels XRD und TEM konnten Netzwerkstrukturen in der Größenordnung von einigen nm nachgewiesen werden. Letztlich wurden die Halbleiterkomposite als Aktivschichtmaterialien in Bulk-Heterojunction Hybrid solarzellen untersucht.

Die beschriebene Methode wurde in weiterer Folge zur Präparation von ternären Halbleitern verwendet, es wurden Komposite aus CuInS_2 und P3EBT derart hergestellt. Für dieses Materialsystem wurden Precursormaterialien, -zusammensetzung, Donor-Akzeptorverhältnis sowie Prozessierungsparameter hinsichtlich Anwendung in Hybrid solarzellen optimiert. In weiterer Folge wurden quaternäre Akzeptoren des Typs $(\text{ZnS})_{2x}(\text{CuIn})_{1-x}\text{S}_2$ präpariert. Dieses Material liefert in Kombination mit P3EBT als Donorphase größere Klemmspannungen in Hybrid solarzellen. Die strukturelle Charakterisierung erfolgte mittels XRD und SEM, die Stöchiometrie der Aktivschicht wurde

mittels SEM-EDX bestimmt. Ein besonderes Augenmerk lag auf der Untersuchung des Heizprozesses, der mittels online-XRD, TGA-MS sowie FT-IR Spektroskopie untersucht wurde. Bei der chemischen Analyse der Zersetzungsreaktion durch Massenspektrometrie konnte die Bildung von Nebenprodukten nachgewiesen werden.

Im letzten Abschnitt werden Stabilitätstests organischer Solarzellen beschrieben. Hier wurden zum einen verschiedene Polymere (F8T2, MEH-PPV, P3HT) mit PCBM als Akzeptor, andererseits verschiedene Polymer-CuInS₂ Kombinationen (F8T2, MDMO-PPV, MEH-PPV sowie F8T2) untersucht.

Contents

Acknowledgements	i
Abstract	ii
Kurzfassung	iv
1 Introduction	1
1.1 Energy Situation.....	1
1.2 Hybrid Solar Cells – A Very Short Introduction.....	3
1.3 Thesis Overview	4
2 Solar Cell Basics	6
2.1 General.....	6
2.2 Solar Cell Parameters.....	7
2.3 Device Aspects	9
3 Materials	19
3.1 Conjugated Organic Polymers	19
3.1.1 PPV-Type Polymers	19
3.1.2 Polythiophenes	20
3.1.3 Copolymers – Low Bandgap Polymers.....	21
3.2 Acceptor Phases.....	23
3.2.1 Fullerene Based Acceptors.....	23
3.3 Semiconductor Acceptors.....	25
3.3.1 ZnS.....	25
3.3.2 CdS	25
3.3.3 CuInS ₂	26
4 Experimental	29
4.1 Preparations.....	29
4.2 Instrumental	30
4.3 Construction of a Multi-Channel Stability Testing Appliance.....	33
4.4 Chemicals.....	35
5 Preparation of Binary Semiconductor –	
Conjugated Polymer Composites and Solar Cells	36
5.1 Introduction	36
5.2 Experimental.....	37
5.3 Results and Discussion.....	37
5.3.1 P3EBT-CdS Composites	37

5.3.2	P3EBT-PbS Composites	40
5.3.3	P3EBT-ZnS Composites	41
5.4	Conclusion.....	43
6	PPV – CuInS₂ Solar Cells.....	45
6.1	Introduction	45
6.2	Solar cell Preparation.....	46
6.3	Results and Discussion.....	47
6.3.1	Morphology and Structure of PPV-CIS Blend.....	47
6.3.2	PPV-CIS Solar Cells	48
6.4	Conclusion.....	52
7	P3EBT – CIS Composites and Solar Cells	53
7.1	Introduction	53
7.2	Proof of Principle – XRD analysis of an in-situ P3EBT – CIS composite ...	53
7.3	Bilayer Heterojunction Solar Cells and Optimization of CuInS ₂ Stoichiometry	54
7.3.1	Experimental	55
7.3.2	Results and discussion	56
7.4	P3EBT-CIS Bulk Heterojunction Solar Cells from Different Copper- and Indium Precursors	58
7.4.1	Introduction	58
7.4.2	CuI-InCl ₃ -TAA Precursor in Acetonitrile – Pyridine	58
7.4.3	CuAc - In(Ac) ₃ - TU - Pyridine Precursor	59
7.4.4	Copper(I)chloride- In(acac) ₃ - TU - Pyridine Precursor Solutions	60
7.4.5	CuAc – InCl ₃ – TU – Pyridine Precursor	61
7.4.6	Conclusion from Precursor Experiments	62
7.5	Investigation of Donor – Acceptor ratios and Concentration of the Precursor	63
7.5.1	Introduction	63
7.5.2	P3EBT-CIS Solar Cells with Different Donor and Acceptor concentrations.....	64
7.6	Analysis of the Annealing Process and Optimization of Heating Rates...66	
7.6.1	Introduction	66
7.6.2	Online XRD-Monitoring of CuInS ₂ Formation	66
7.6.3	Investigation of the Decomposition Process by TGA-MS	67
7.6.4	Analysis of the Annealing Process using Mass Spectrometry	71
7.6.5	Thermal Stability of P3EBT	73

7.6.6	Hybrid Solar Cells Using Different Annealing Procedures	75
7.6.7	Conclusion.....	76
7.7	Incorporation of Zn, Acceptor Phase Stoichiometry and Solar Cell Action	77
7.7.1	Introduction	77
7.7.2	Hybrid P3EBT-ZCIS Solar Cells	77
7.7.3	ZCIS-Precursor Stoichiometry - Active Layer Morphology - Active Layer Stoichiometry	79
7.8	Conclusion.....	82
8	Stability Testing of Plastic Solar Cells	84
8.1	Introduction	84
8.2	Stability of Polymer – PCBM Solar Cells.....	84
8.3	Stability of Polymer – CuInS ₂ Solar Cells.....	87
8.4	Conclusion.....	89
9	Summary and Outlook	91
10	Appendices	97
10.1	Appendix 10.1: P3EBT Data	97
10.2	Appendix 10.2: i-V Curves from P3EBT-CIS Devices with Different Donor and Acceptor Contents	98
10.3	Appendix 10.3: i-V Curves of P3EBT-CIS Devices Using Different Annealing Procedures	99
10.4	Appendix 10.4: TGA Data of Active Layer Components, Mass Spectra.....	101
10.5	Appendix 10.5: ZCIS-Stoichiometry: i-V Curves	103
10.6	Appendix 10.6: EDX-Analyses of P3EBT-ZCIS Active Layers with Different Stoichiometry.....	104
10.7	Appendix 10.7: Morphology of ZCIS-P3EBT Active Layers with Different Cu / In – morphology	110
10.8	Appendix 10.8: Stability Data of Plastic Solar Cells	111
11	List of Figures.....	116
12	List of Tables	122
13	Abbreviations	124
14	Bibliography	127
15	List of Pulications	146

1.1 Introduction Energy Situation

With the development of civilization and society its hunger for energy is ever increasing. There is a dramatic disparity in energy consumption between different regions and cultures, a resident in North America consumes more than 10 times the energy than an average Asian citizen (281 GJ vs. 25 GJ per person p. a. [1]). Between 1973 and 2007 world energy consumption has increased from 195.7 EJ to 346.9 EJ (+77 %) [2].

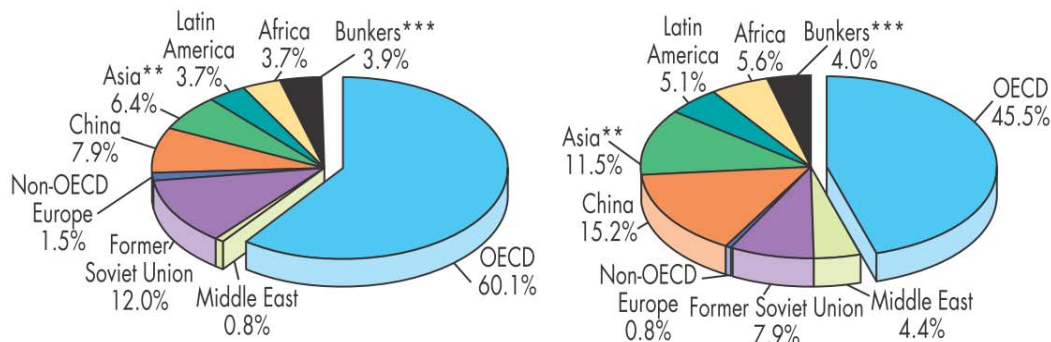


Figure 1: World energy consumption after region in 1973 (left) and 2007 (right) [2]

Predominantly fossil fuels, which today cover ca. 80% of the energy supply, are consumed, consequently emission of green house gases is augmenting and scenarios of global warming recommend the transition to a sustainable energy policy. The fossil carriers need to be replaced by alternative energies, which have a neutral CO₂-balance. From the options available photovoltaics has a huge potential, irradiation from the sun is providing 3.9 e⁶ EJ / a, an amount which could easily satisfy global energy consumption [3].

Table 1: Current use and potential of renewable energy forms [3]

Resource	Current use / EJ/a	Technical potential / EJ/a	Theoretical potential / EJ/a
Hydropower	9	50	147
Biomass energy	50	>276	2,900
Solar energy	0.1	>1575	3,900,000
Wind energy	0.12	640	6,000
Geothermal energy	0.6	5000	140,000,000
Ocean energy	n.e	ne.	7,400

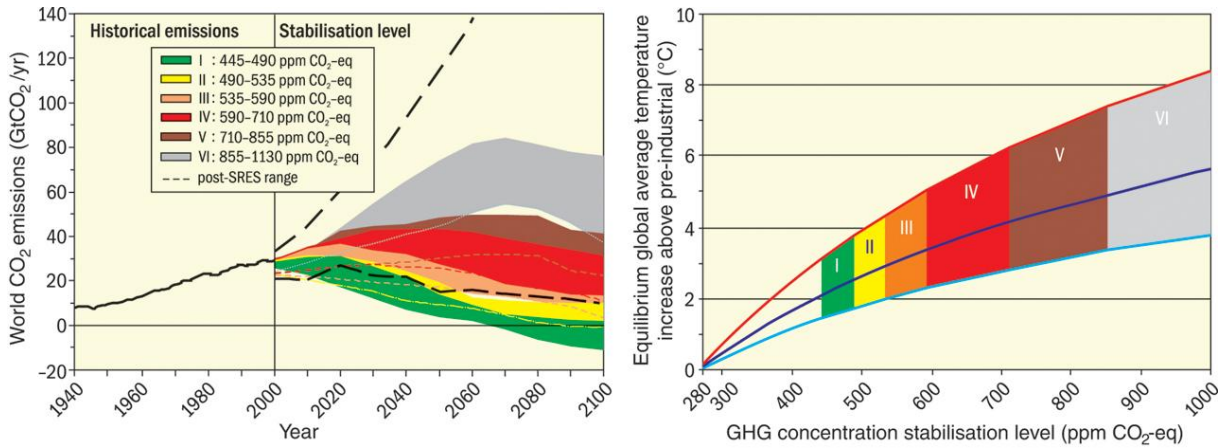


Figure 2: Left: Global CO₂ emissions and development scenarios for various CO₂ concentrations. Right: Prognostic elevation of likely world mean temperature above the pre-industrial at different CO₂ levels; there is no time axis because equilibration times are not reliably predictable [4]

Currently, renewable energy sources have a proportion of 2.2 % in the global energy mix (hydro power and traditional biomass not included) [1], a strikingly low number when considering the (future) CO₂ emissions and the concurrent rise in temperature (Figure 2). When photovoltaic technology shall play an important role in the future, it needs to comply with market requirements, which is up to now not the case. So far, development of the photovoltaic economy was driven by supporting policies of governments, e. g. the feed-in tariff models in Germany or Spain. The sector has seen a powerful growth during the last decades, with rapid progress of annual installed PV-capacity.

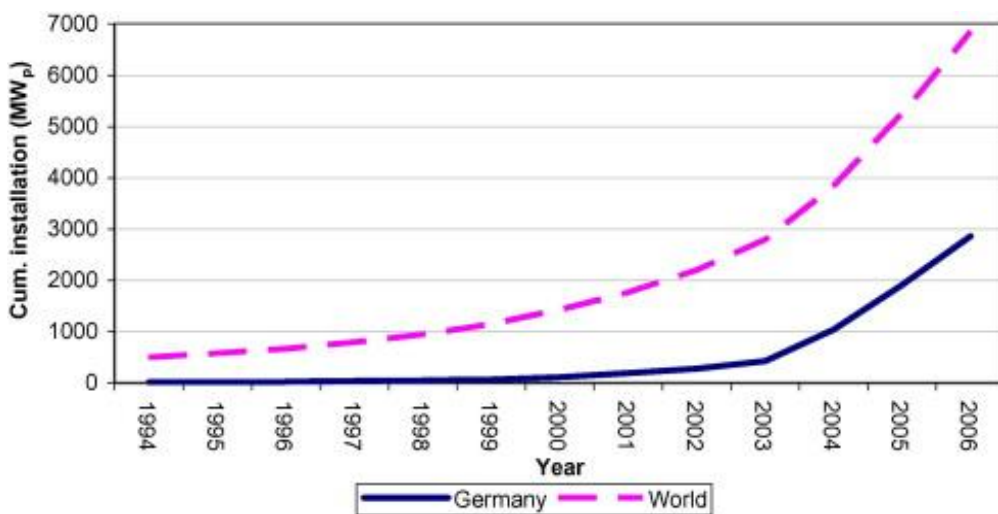


Figure 3: Cumulative PV installation in Germany / worldwide [5]

PV technology will be competitive, when grid parity is reached, however substantial cost reductions are necessary, opening the door for new technologies as e. g. polymer-based solar cells. Despite the failure of the Copenhagen Climate Council in 2009 extent of sustainable energy sources will augment in the future (probably with support from tomorrow fuel prices) and solar energy can play a major role in this process.

1.2 Hybrid Solar Cells – A Very Short Introduction

Within PV technology, organic heterojunction solar cells are a quite young member of the family, with the first scientific paper published in 1986 by Tang et al. [6] (photoeffect in excitonic homojunction setups was observed already in 1959, though with very low efficiency [7]). Organic solar cells are an appealing alternative to the established systems, materials consumption is low (layer thicknesses are in the 100-nm regime) and they can be fabricated using wet-chemical deposition techniques and roll to roll processes. After significant progress in development of conducting π -conjugated materials the subject received a considerable impulse from discovery of the Buckminster Fullerene [8], which was found to be an excellent electron acceptor and showed semiconducting properties. Since the publication of the charge transfer from a conducting polymer onto C_{60} by Sariciftci et al. in 1992 [9], the subject rapidly developed. In the following, many different material combinations were tested as active layer; a hybrid solar cell is obtained, when a nanostructured inorganic semiconductor is used in combination with an organic donor [10]. This concept bears the advantage that generation of charges can also take place in the acceptor phase, whereas C_{60} is a poor absorber.

Current Status

Considering hybrid systems, naturally a greater variety of possible donor-acceptor combinations exists. From the numerous semiconductors with suitable opto-electronic properties in particular II-VI systems have been developed as hybrid absorber components. Most effort was spent on research of CdSe acceptors in combination with various conjugated polymers [11-13], as band levels of CdSe are very suitable for photovoltaics ($E_g(\text{bulk}) = 1.75 \text{ eV}$). Depending on preparation conditions, different shapes

can be obtained, spheres, rods tetrapods or hyperbranched CdSe were reported [14]. This illustrates an additional tuning parameter of when nano-structured semiconductors are involved, as the geometry can affect electronic properties and has implications on the percolation in a composite layer. The sister components, CdS and CdTe also have been utilized in hybrid solar cells, though not as extensively [15],[16]. The second important materials class in context with hybrid solar cells are oxides, titanium oxide and zinc oxide have been thoroughly investigated as acceptor materials [17-19]. Current record efficiencies are in the range of 3%, which have been obtained with tetrapod-shaped CdSe acceptor phases in combination with MDMO-PPV [20]. Similar values have been obtained for a ZnO-P3HT [21] devices and a CdS-P3HT combination [22], when the acceptor phase is prepared in-situ with no surfactants present.

1.3 Thesis Overview

The subject of the current work is development and optimization of polymer – chalcopyrite composites, which are utilized as the active layer in hybrid solar cells; the acceptor phase is obtained via an in-situ formation process within the matrix of the conjugated polymer by decomposition of a sulfur source. In a second part the stability of plastic solar cells was investigated. For this task a testing unit was constructed, which allows multi-channel testing of solar cells under permanent illumination. Solar cell parameters as a function of time are calculated and logged by a custom made LabView-program.

The following two chapters deal with basic theoretical framework of organic solar cells and semiconducting materials, followed by a short part on general experimental procedures, detailed processing parameters etc. are given in the respective section. Special emphasis is put on aspects of conjugated polymers and CuInS₂ (CIS), which served as acceptor phase in the majority of the experiments. Hereafter findings are presented in the section “Results and Discussion”:

- Chapter 5 covers the in-situ formation of the CdS, PbS and ZnS polythiophene composites, the CdS composite was used as active layer in bulk heterojunction type hybrid solar cells. Structural and morphological characterization was performed using XRD, TEM and TEM-EDX, optical properties were investigated using UV-Vis spectroscopy.
- The next section deals with the PPV-CIS system [23]. The acceptor phase is formed in situ by decomposition of thioacetamide, which reacts with Cu- and In-ions present in a matrix of a PPV-precursor. The influence of the precursor age was probed in a subsection.
- Chapter 7 Investigations on polythiophene-CuInS₂ composites: The precursor route developed for binary semiconductor-polymer blends is adapted for the in-situ formation of CuInS₂. Thorough examination of the precursor system in terms of starting materials, metal stoichiometry, donor-acceptor ratio etc. was conducted. The annealing process was identified as a decisive process parameter and was studied using in-situ XRD, TGA-MS, FT-IR and MS, which also allowed the identification of a side-product of the annealing reaction (Melamine).
- Hybrid solar cells with a ZnS_{2x}.(CuIn)_{1-x}S₂ acceptor phase (section 7.7) were prepared using the developed route (polythiophene polymer, thiourea sulfur source). Systematic investigation of Cu- and In-stoichiometry was performed by SEM-EDX measurements, devices were optimized with respect to Zn-content. Active layer surface morphology was analyzed using SEM, charge generation was probed by EQE experiments.
- Stability testing (chapter 8): A multi-channel testing setup for permanent solar cell testing was constructed. The following systems were tested for their long-term stability: (1) P3HT - PCBM, (2) MEH-PPV – PCBM (3) F8T2 – PCBM; (4) PPV – CIS, (5) MEH-PPV – CIS, (6) MDMO-PPV – CIS, (7) F8T2 – CIS. Systems (5)-(7) were prepared using a novel in-situ formation route [24],[25].

A concluding remark at the end of the thesis gives a short review on the findings and outlines possible future directions. Part of the measurements is not presented within the main text and has been grouped into appendices.

2 Solar Cell Basics

2.1 General

At the centre of our planet system a star is shining with a surface temperature of approx. 5800 K – the sun. The earth, at a secure distance of $1.5e^{11}$ m, is orbiting around it. In the suns core hydrogen is converted into helium by nuclear fusion at temperatures of $15.6 e^6$ K, releasing an energy of 27 MeV for every ^4He core that is formed. The solar constant is assigned to $E_{\text{SC}} = 1367 \text{ W.m}^{-2}$, corresponding to the radiative flux incident to the earth [26].

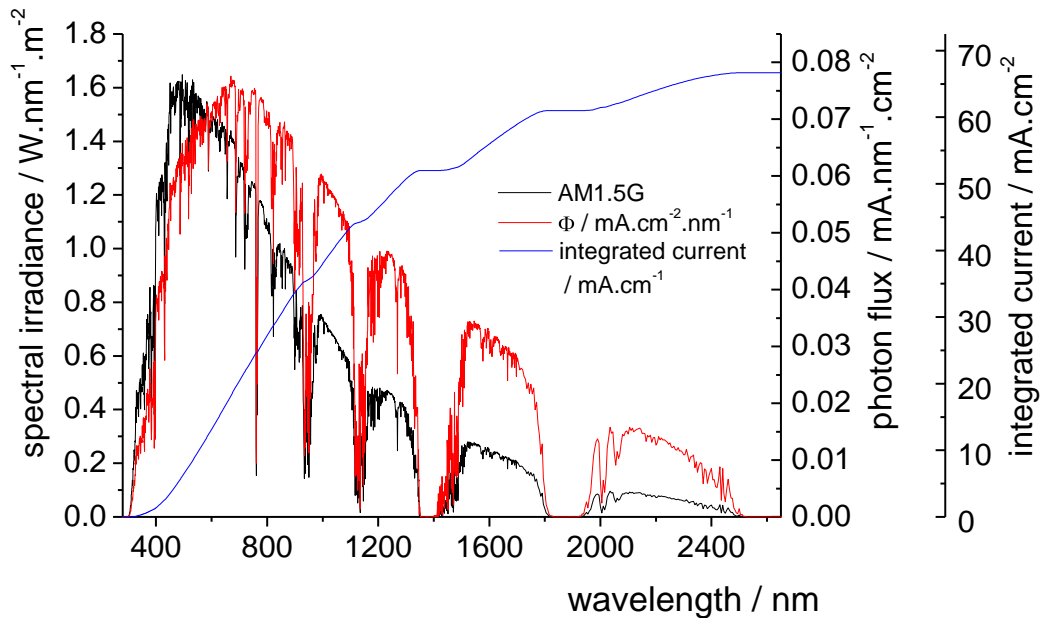


Figure 4: AM1.5G spectrum [27]. The red line corresponds to the number of photons, the blue line indicates the integrated current (every photon converted into a pair of charge carriers)

When the photons travel through the atmosphere, part of the radiation is lost due to scattering and absorption, hence the appearance of the spectrum on the earths surface is altered. Depending on the distance covered within the atmosphere, different AMx (AM = air mass) standards were defined; $x = \frac{1}{\cos \vartheta}$ (ϑ : angle of incidence). A widely used standard is AM1.5G, corresponding to a tilt angle of 37 °. Spectral irradiation in the AM1.5G standard is set to 1000 W.m^{-2} (actual value is 963 W.m^{-2}). The spectral

distribution is obtained, when the path of the light covered in the atmosphere is 1.5 times its thickness. The spectrum is plotted in Figure 4, together with the photon flux (red line). The integrated current (blue line) corresponds to quantitative conversion of photons into charge carrier pairs, representing the definitive limit for photocurrent.

Table 2: Integrated current at various wavelengths in the AM1.5G spectrum

λ / nm	500	600	650	700	750	800	900	1000	1250	1500
% of total photons	8	17.3	22.4	27.6	35.6	37.3	46.7	53	68.7	75
current / mA.cm^{-2}	5.1	11.1	14.3	17.6	20.8	23.8	29.8	33.9	43.9	47.9

Photon absorption and photovoltage of the device are governed by the bandgap of the semiconductor. Based on the bandgap value of the absorber material and thermodynamic limitations of solar cells [28], the theoretical limit for energy conversion in solar cells is 48%, limit for single-bandgap systems is 30% (Shockley-Queisser limit [29],[30]). Practically, a maximum (confirmed) PCE of 26% and 25% was reached for single layer absorber cells (GaAs thin film, Si single crystal [31]). Performance assessment for bulk heterojunction type solar cells naturally involves two materials (donor- and acceptor phase), the effective bandgap $E_g(\text{eff})$ ($\Delta E(\text{HOMO}_{\text{DONOR}}-\text{LUMO}_{\text{ACCEPTOR}})$) is the limiting value for the V_{OC} . Recent estimates on organic solar cells have shown possible PCE of ca. 10%, however, precisely engineered band offsets and high mobility materials are required [32]. Currently maximum (published) PCE for fullerene based solar cells is 7.4% [33], while the best polymer-hybrid systems show values around 3% [34],[22],[10].

2.2 Solar Cell Parameters

To determine the performance of a solar cell, the i-V curves of the device are recorded under dark and illuminated conditions. A diode-like shape is obtained (Figure 5). From the illuminated curve, the parameters of the solar cell are extracted. The intersection with the abscissa corresponds to the open circuit voltage (V_{OC}), intersection with the ordinate amounts the short circuit current density (i_{SC}). Power conversion efficiency (PCE) is obtained by evaluating the maximum power point (mpp), with current density- and voltage values i_{mpp} and V_{mpp} . Fill factor (FF) is obtained by division of ($V_{\text{mpp}} \times i_{\text{mpp}}$) by ($V_{\text{OC}} \times i_{\text{SC}}$) and reflects the quality of the diode (FF is the ratio of the two rectangles in Figure 5).

$$FF = \frac{V_{mpp} i_{mpp}}{V_{OC} i_{SC}} \quad PCE = \eta = \frac{P_{ex}}{P_{in}} = \frac{V_{OC} i_{SC}}{P_{in}} FF \quad (I)$$

External quantum efficiency (EQE, dimensionless) accounts for the conversion of photons into current at defined wavelengths (monochromatic irradiation), the spectral response (SR / mA.W⁻¹.nm⁻¹) practically covers the same aspect. The internal quantum efficiency (IQE) is related to EQE when reflection / transmission of the device are considered. Integration of the spectral response basically should return the i_{SC} -value [35].

$$EQE = \frac{\#(e(\lambda))}{\#(phot(\lambda))} = \frac{hc}{qe\lambda} \frac{i_{sc}(\lambda)}{P_{in}(\lambda)} \quad SR = \frac{qe}{hv} EQE \quad IQE = \frac{EQE}{(1-R-T)} \quad (II)$$

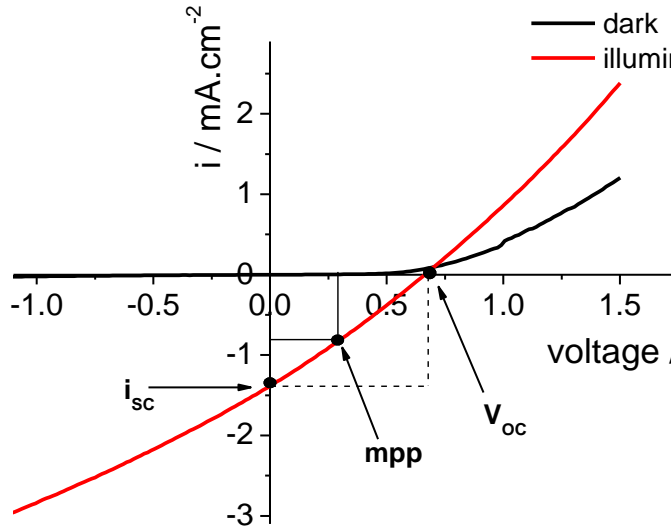


Figure 5: i-V curve of a solar cell under dark and illuminated conditions

In order to ensure parameters to be comparable, testing should be performed under standard reporting conditions (SRC), which for solar cells are defined by the standards ASTM E948, EUR-7078 EN, IEC 60904-1, IEC 60904-3 [36-39]. Requirements to be met are spectral irradiance / distribution (AM1.5G @ 1000 W.m⁻²) and temperature (25 °C device temperature), which requires irradiation with a solar simulator. The deviation of the emission spectrum of the light source from the reference spectrum is taken into account by the spectral mismatch factor M, where SR is the spectral response, E is the irradiance, subscript R refers to the reference cell, T to the tested cell S to the light source and ref to the reference spectrum the tested cell [40].

$$M = \frac{\int SR_R(\lambda) E_{ref}(\lambda) d\lambda}{\int SR_T(\lambda) E_{ref}(\lambda) d\lambda} \frac{\int SR_T(\lambda) E_S(\lambda) d\lambda}{\int SR_R(\lambda) E_S(\lambda) d\lambda} \quad (III)$$

Proper i_{SC} value is obtained by division with the mismatch factor. While for silicon devices the difference is often neglectable ($M \approx 1$), strong deviations from unity can be obtained for plastic solar cells, as reference cells are usually made of Si or GaAs [41]. Additional features of new solar cell systems not contained in the established standards include slow device response (especially for DSSC), bias-dependent hysteresis and edge- / shading effects [42],[43]. When organic solar cells exhibit i_{SC} values higher than 11 mA.cm^{-2} (corresponding to *quantitative* current generation from all photons up to 600 nm, compare Table 2), or EQE/IQE values close to 100% are reported (especially when current is higher at negative bias), care should be taken (e. g. [23],[44],[45] and [46-48]).

2.3 Device Aspects

Semiconductor Junctions

Common structure of solar cells comprises an active layer in junction with suitable interface layers and electrodes. From the energy of the photons, semiconductor materials are the choice for the active layer, correspondingly solar cell behaviour is very closely related to the physics of semiconductor junctions. One of the most common semiconductor structures is the p-n junction, where a p- and a n-doped semiconductor of the same material (homojunction) are in contact:

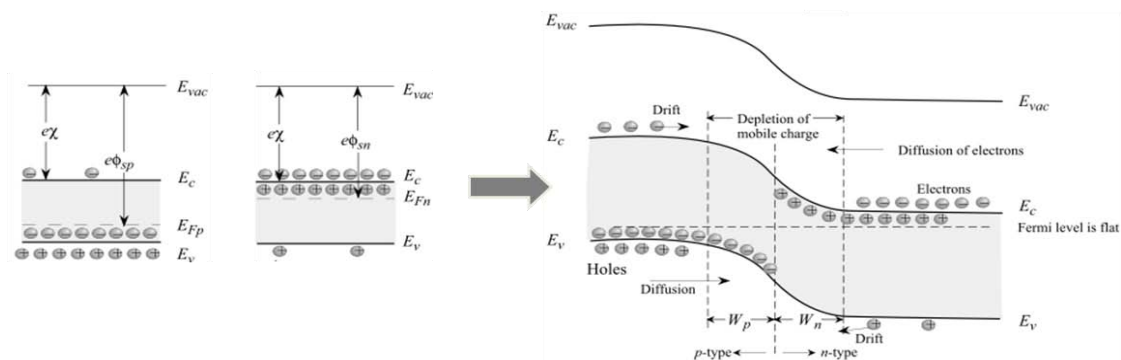


Figure 6: Scheme of p-n junction formation [49]

Doping of the material moves the Fermi level towards the respective band edge, when the p- and n-type doped regions of the material are in intimate contact the bands bend, as flat Fermi level / equal electrochemical potential is the condition for equilibrium [49],[50]. The majority carriers diffuse towards the interface, a depletion region (“space charge”) is formed which is accompanied by the formation of an electrical field (built-in field E_{bi}). Considering heterojunctions, principally the same rules apply, however, according to the relative band levels, workfunctions ϕ , electron affinities χ and carrier densities a greater variety of band structures is possible (e. g. band offsets, band discontinuities).

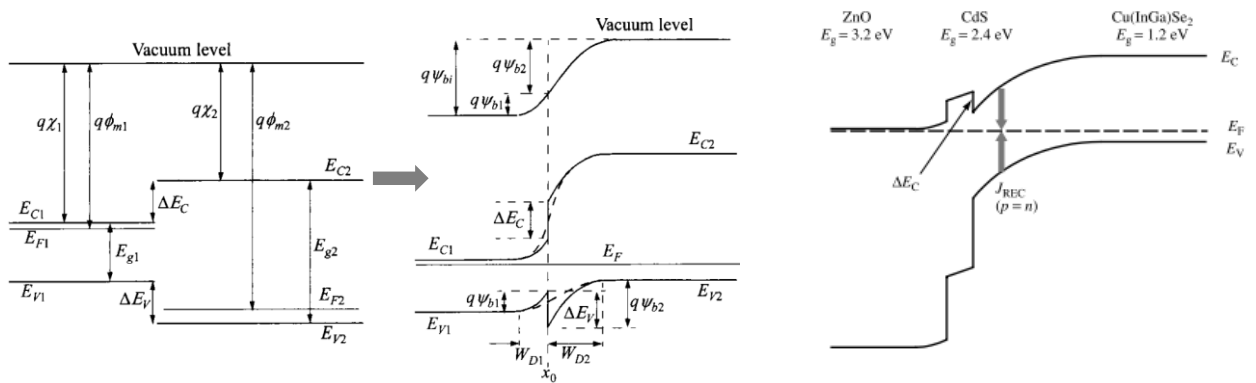


Figure 7: Left side, middle: Band profile formation of two materials of different bandgap, workfunction and electron affinity [51]; right side: band profile of the ZnO-CdS-CIGS heterojunction at short circuit [35]

Figure 7, left side, shows an example for the band profile of an anisotype type-I heterojunction, where the bandgap of the n-type material is smaller than that of the p-type material, whereas on the right side the anisotype type-II heterojunction of a CIGS solar cell is displayed.

Organic Semiconductors

With the discovery of doped polyacetylene in the 70s by Shirakawa et al. [52] the topic of polymeric / organic semiconductors started, in the meantime organic electronics has become a dynamic inter-disciplinary branch of science. Physical properties with relevance to device applications are based on conjugated delocalized π -electron systems, which account for a great part of the optoelectronic properties of the materials. Comparison of conjugated polymers with inorganic semiconductors shows apparent differences:

- Semiconductors are crystalline and ordered (which is a requirement), while conducting polymers usually are partially crystalline or amorphous
- Carrier mobilities of organic semiconductors are several orders of magnitude below the values of inorganic semiconductors
- Exciton binding energies of organic semiconductors are large compared to kT (25 meV) while they are not in inorganic semiconductors

Electron-phonon coupling is a major aspect in organic semiconductors [53], consequently charge transport is determined by polarons rather than free carriers, as in the case of inorganic semiconductors [54]. Additionally there is a lack of periodicity in π -conjugated materials and band like (delocalisation of the wavefunction) transport mechanisms do not apply. Standard transport models include two contributions to the carrier mobility, tunnelling transport and hopping transport, which is thermally activated [54]. High exciton binding energies (in the order of 0.1 - 0.5 eV) and ϵ_r values of approx. 2-4 result in the generation of bound electron hole pairs rather than free carriers. Exciton diffusion radii and lifetimes are in the range of nm and ns [55],[56] (considerable higher values are possible for triplet excitons [57-59], respectively, which needs to be considered in the architecture of organic devices.

Table 3: Typical properties of singlet excitons in conjugated polymers

properties		processes	
charge	neutral	fluorescence	$S_1 \rightarrow S_0 + h\nu$
spin multiplicity	1	ISC	$S_1 \rightarrow T_1$
lifetime	0.01-10 ns	internal conversion	$S_1 \rightarrow S_0 + \text{heat}$
Diffusion length	1-20 nm	quenching	$S_1 + X \rightarrow S_0 + \dots$

Heterojunctions of Organic Semiconductors

As exciton binding energy is large compared to kT , heterojunction designs are necessary to achieve generation of free carriers / polarons in conjugate organic materials, as was demonstrated by Tang in 1986 ("Tang Cell") [6]. Organic homojunctions generally do not show a substantial photoeffect [7]. The presence of the acceptor phase is an essential condition for organic solar cells, the band offset between the LUMO energies of donor

and acceptor component needs to exceed the exciton binding energy (exciton dissociation) [60-63]. This is realized by intimate contact of the conjugated material (donor phase) with the acceptor phase, which has staggered FOs (type II heterojunction). In the bilayer heterojunction approach, donor and acceptor material are part of adjacent layers, whereas in the bulk heterojunction system a composite of the two phases (interpenetrating network) makes up the active layer; intermediate forms, e. g. diffuse bilayer heterojunction, are also known [64],[65].

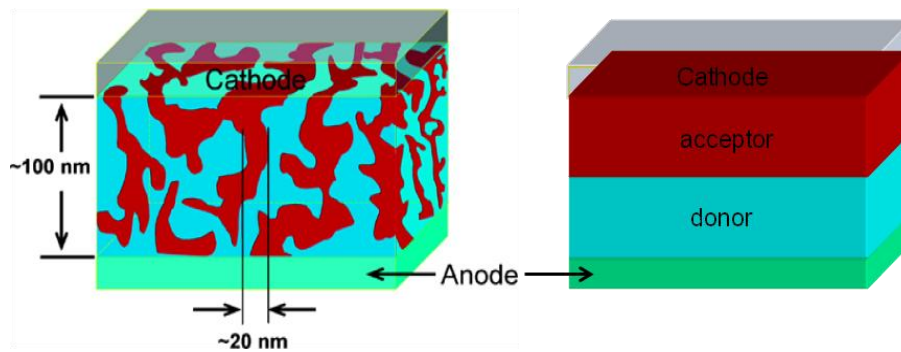


Figure 8: Schematic drawing of bulk- and bilayer-heterojunction architectures (adapted from [21])

Considering the FO profile of organic heterojunction solar cells, the picture drawn so far needs refinement. Under the prerequisite of interfacial charge transfer, i. e. formation of a surface dipole and vacuum level shifting, level alignment is has been observed in various systems (surface transfer doping), including organic-metal junctions [66] and P3HT-based systems [67],[68] or ITO-PEDOT [69],[70].

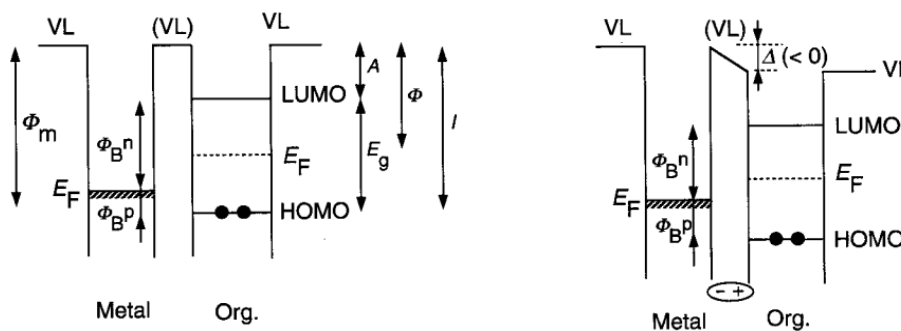


Figure 9: Level alignment of a metal – organic semiconductor interface; right: common vacuum level (VL); left: formation of an interface dipole and vacuum level shifting (Δ) note the changed injection barriers Φ

[66]

While band alignment is a well established phenomenon, band *bending* in systems involving organic semiconductors is highly disputable. It is suggested that bands are linear due to low carrier densities and small length scales in organic semiconductor films [66],[71],[72]. Following the argument, electronic structure of organic solar cells can be reasonably approximated using the MIM (metal-insulator-metal) picture, assuming no band bending and linear band profiles (compare Figure 10) [73].

Charge Generation

When light is absorbed by a solar cell charge carriers are created and extracted at the electrodes. The balance of the process described the continuity equations [51],

$$\frac{\partial p}{\partial t} = -\frac{1}{q_e} \nabla J_p + g_p - r_p \quad (\text{IV})$$

$$\frac{\partial e}{\partial t} = \frac{1}{q_e} \nabla J_e + g_e - r_e \quad (\text{V})$$

where J is the current density, q_e is the elementary charge, g refers to the generation rate, r to the recombination rate, e and p stand for electrons and holes. Currents can be described using the drift-diffusion model [51],

$$J_e = q_e n \mu_e E + q_e D_e \frac{\partial e}{\partial x} \quad (\text{VI})$$

$$J_p = q_e p \mu_p E + q_e D_p \frac{\partial p}{\partial x} \quad (\text{VII})$$

which can be inserted into the continuity equations (D and μ refer to the diffusion coefficient / mobility, p and n is the number of holes / electrons). Device behaviour can be calculated using above equations, when appropriate boundary conditions reflecting the properties of the materials (μ , ϵ , D_i) and the device (contacts, thickness, morphology, ...) are found and the local electrical field is calculated using Poisson equation [74],[75].

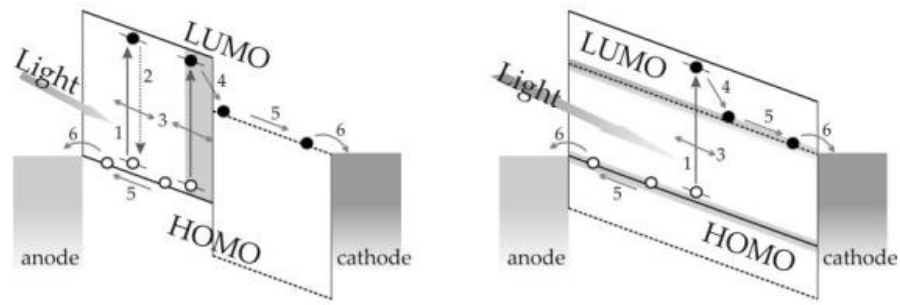


Figure 10: Current generation in organic heterojunction solar cells (bilayer: left, bulk: right) [76]

Photovoltaic current generation in organic solar cells is summarized by the following steps:

- absorption of light, formation of excitons
- exciton diffusion to interface / recombination
- exciton dissociation, generation of free carriers / polarons
- charge transport
- charge collection at electrodes

Absorption of light is the preliminary condition for current generation, low bandgap organic materials ($E_g < 2\text{eV}$) are at the center of interest, when more than 20% of the incident photons shall be absorbed (compare Table 2). Practically, due to low mobility values, the thickness of the active layer is limited to some hundred nms, which is a limitation for quantitative absorption over the entire range of the polymer, even though absorptions coefficients of conjugated polymers are high ($\epsilon_{\text{max}} \approx 1\text{e}^5 \text{cm}^{-1}$ [65],[77],[78]).

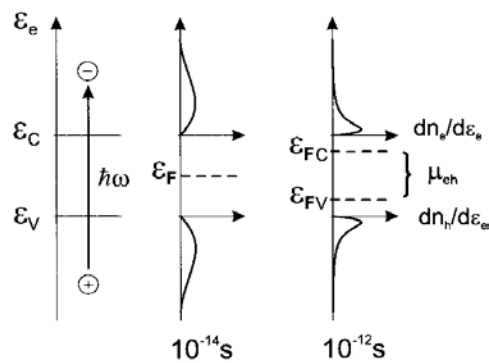


Figure 11: Absorption of photons, thermalization and splitting of the Fermi level [50]

The hot carriers thermalize and form excitons which have mean lifetimes and diffusion radii in the ns / nm range (singlet excitons, compare Table 3; higher values for triplet excitons [57]). Within this time, they need to reach an interface where they can dissociate, if not recombination takes place. Exciton dissociation involves the formation of bound electron hole pair at the interface (= geminate electron hole pair, charge transfer exciton [79]), which can dissociate into free charge carriers or recombine [76],[79],[80], the dependence from thermal motion and from the electric field present in the device can be described using a modified Onsager theory [81-83]. From a thermodynamic point of view, the Fermi level of the compound is split up into two quasi-Fermi levels, that is the conversion of photon energy into chemical energy. The splitting of the levels is corresponding to the electrochemical potential μ ($\mu_i = \left(\frac{\partial G}{\partial n_i}\right)_j + v_i F \Phi$ [84]) of the electron-hole pair, which is the energy that can be transformed by the device [28],[50]; excitonic effects in context of this model are reviewed in [85].

Once the free carriers / polarons are generated, they need to be transported to the respective electrode. High mobility materials are essential to avoid bimolecular recombination (which is dominant over geminate recombination only in low-mobility materials or thick layers) [86-88], balanced mobilities prevent the formation of space charges [89]. Using the bulk-heterojunction architecture, continuous pathways of the donor and the acceptor phase to the respective electrode is an additional condition for efficient charge transport, as islands / dead ends cannot contribute to charge extraction. Phase separation (which should occur on nm-scale) of the components is influenced by their solubility and chemical interaction [90],[91], hence optimization of materials, solvent / solvent additives and processing conditions, are major ingredients for efficient solar cells [92-98]. Additional tuning of the blend morphology can be achieved by application of an annealing step where the material reorganizes [99-105].

The charges are extracted at the electrodes, anode materials are transparent conducting oxides (TCOs) [106], most frequently indium-tin oxide on various substrates (glass, PET, polyimide) is used. Workfunction modification and tuning of injection / extraction barriers can be performed using (polymeric) interface layers or self assembled monolayers (SAMs)

[107-109]. PEDOT-PSS (compare section 3.1.2) is a standard interface layer for its hole-transport properties [110], another successfully implemented polymeric interface layer in plastic electronics is PANI (Polyaniline) [111-113]. As the materials can exhibit high conductivity (conductivity of up to 900 S.cm^{-1} [114]) application of purely polymeric electrodes has been examined, especially in inverted device setups [115],[116]. Electrodes are made up of a low-workfunction metal like Ca, Al or Ag. In the MIM picture (assuming no Fermi level pinning) the difference in workfunctions of the electrodes exhibits the built-in field E_{bi} of the device. V_{OC} values are dependent from the workfunction of the cathode, it has been shown however, that i - V curves of devices with different electrodes are practically identical when normalized to the built-in field of $(V_{OC}-V_{applied})$ the device [117].

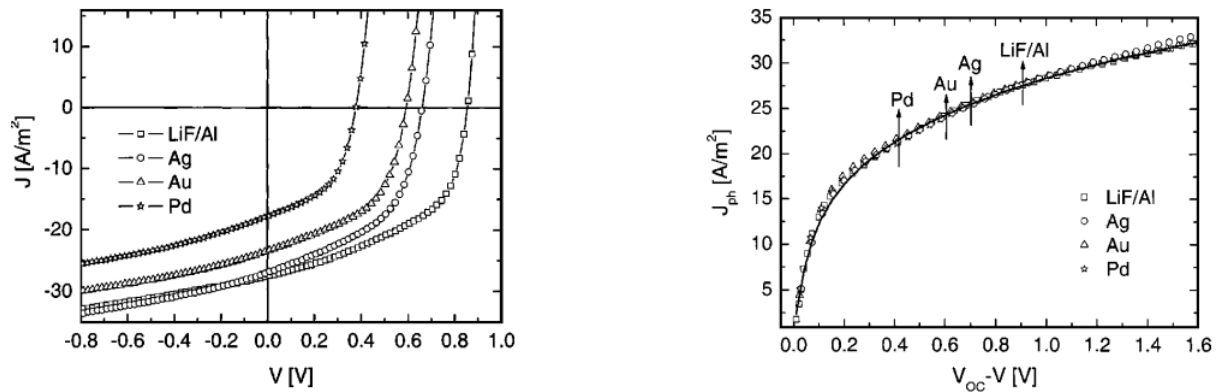


Figure 12: i - V curves of MDMO-PPV – PCBM devices with different cathode; left: i - V curves; right: i - V curves normalized to the built-in field of the device [117]

Cathode interface layers are utilized for contact modification (ohmic contacts with LiF interlayer [73],[118]) and tuning of the electronic structure by surface transfer doping [60]; additional benefits are increased device stability [119] and enhanced optical absorption (node of electric field vector displaced from reflecting electrode [120]).

Solar Cell Operation

Depending on the applied voltage charge carriers are extracted or injected, the electronic levels follow the potential of the source / voltage drop at the load.

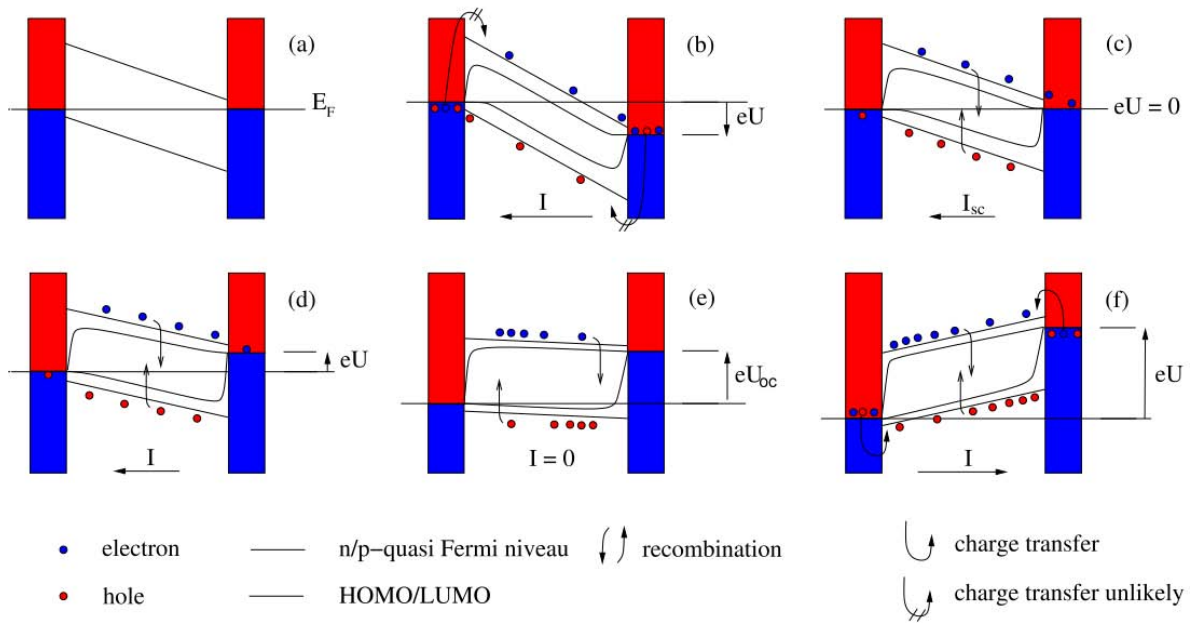


Figure 13: Solar cell with asymmetric contacts at different bias voltages (see text) [121]

- (a) Darkness; solar cell at short circuit, Fermi level is flat
- (b) Illumination under reverse bias causes Fermi level splitting, charge carriers are extracted at the electrodes
- (c) Short circuit under illumination; extraction
- (d) Illumination with attached load; extraction
- (e) Device under illumination at open circuit; Fermi levels are flat (flatband condition); carrier recombination
- (f) Forward Bias, carrier injection

A more detailed description is given in [121]. At reverse bias (b) the built in field is large and carriers are extracted rapidly. When the mean free path of carriers is higher than the thickness of the device, carriers are extracted quantitatively, the current (saturation current) is corresponding to the generation rate of the device (compare equations IV and V) [49]. Practically (solar cell operation) (d) applies, the device is at a moderate internal field, charges are extracted at the electrodes, pass the load and reenter the circuit. At open circuit, built-in field is zero, electron-hole pairs recombine, in organic solar cells excitons cannot dissociate due to their strong binding energy (one reason for comparably low fill factors in plastic solar cells). At forward bias (f), charges are injected and

luminescence can be observed given proper device architecture / materials (direct bandgap semiconductors). The slope of the i-V curve indicates the different stages of device operation.

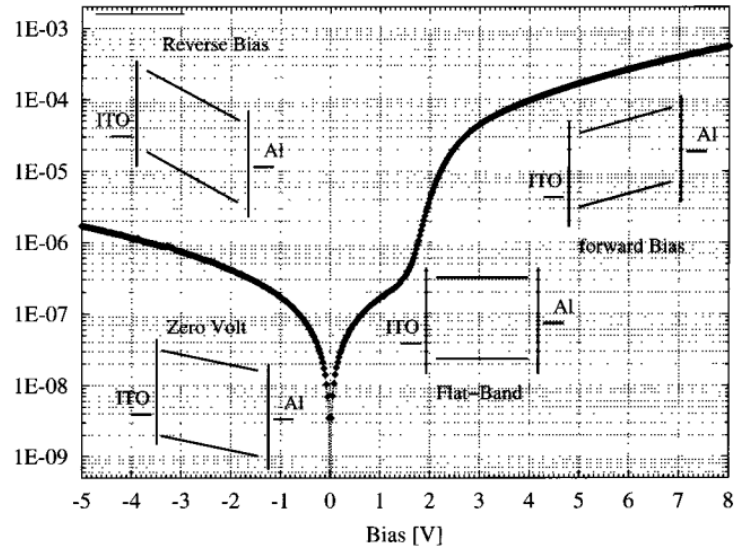


Figure 14: Dark i-V curve of a bulk-heterojunction device in logarithmic scale [77].

3 Materials

3.1 Conjugated Organic Polymers

As outlined in section 2, organic conjugated materials can be utilized as donor phase in heterojunction-type solar cells. Besides absorption of light / exciton generation and subsequent transfer of an electron to the acceptor phase, hole transport is the principal task of the donor phase. Following this simple conceptual argument, prerequisites for a good donor material are high absorption coefficients, suitable bandgap and high mobility values. Considering the interaction with the acceptor phase, FO energy and chemical compatibility with the acceptor material as well are necessary prerequisites. In the following, a short review on the most popular substance-classes within the vast topic of conjugated polymers is given.

3.1.1 PPV-Type Polymers

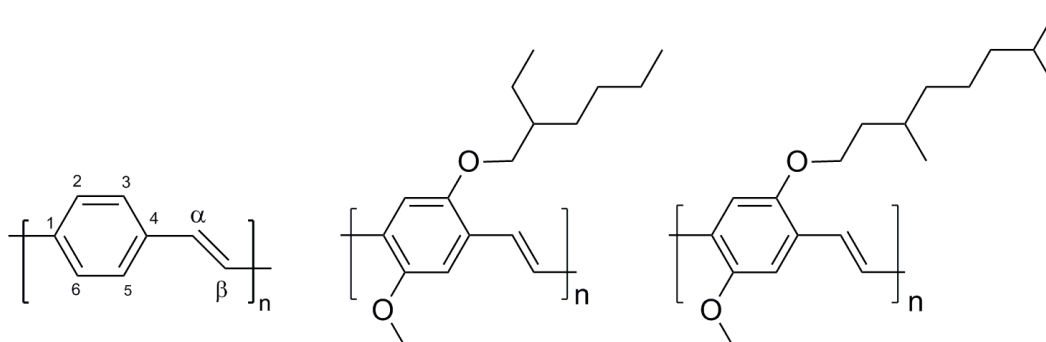


Figure 15: Structure of PPV (with numbering scheme), MEH-PPV and MDMO-PPV (left-middle-right)

While the synthesis of Poly-para-vinylene-phenylenes (PPV) was already developed in the 60s [122],[123] (more recent preparation routes are outlined in [124-126]), it was in the 80s, after the publication of the high conductivity of doped polyacetylene by Shirakawa et al. in 1977 [52], when the field of plastic electronics started and interest turned on PPV-type materials [127],[128], especially in connection with PLEDs, as high luminescence quantum yields have been reported [129],[130]. Non-substituted PPV is not soluble in common solvents, however PPV films can be obtained from precursor materials, where

the conjugated system is obtained by thermal elimination of a leaving group, usually in benzyl-position (α -position in Figure 15) [131]. When side groups are attached to the PPV-backbone soluble materials can be obtained, making them processable in common aprotic solvents like chloroform, toluene or chlorobenzene. Electronic levels are affected due to the interaction of the electron density of side chain atoms with the molecular orbitals of the backbone and due to steric interaction of the sidechain influencing π -overlap of the conjugated system (“bandgap tuning” [132]). PPV bandgaps are ranging from 2.1 to 3.0 eV [78],[133], depending on substituents, substituent-position, synthesis and measurement technique (e. g. CV, UPS or optical measurement, compare Table 4). The most prominent materials in context with organic photovoltaics are MEH-PPV (Poly(2-methoxy-5-{2'-ethylhexyloxy}-1,4-phenylene vinylene) and MDMO-PPV (Poly(2-methoxy-5-{3',7'-dimethyloctyloxy}-1,4-phenylene vinylene), with maximum PCE values ranging from 2-3% in combinations with fullerene-based acceptor species [134],[135].

3.1.2 Polythiophenes

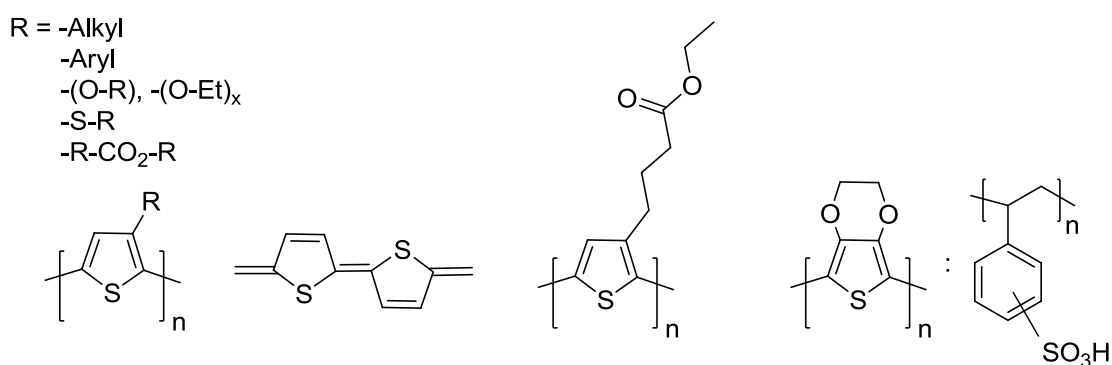


Figure 16: Left: Polythiophene structure; left-middle: quinoid form of PT; right-middle: P3EBT; right: PEDOT-PSS

Synthesis of polythiophenes (PT) and application in plastic electronics started in the 1980s, similarly to PPV-type materials non-substituted polythiophene is not soluble in common solvents (poly-3-butylthiophene is the first compound in the series of poly-alkyl-thiophenes soluble in common solvents [136]). Besides a great variety of functionalities attachable in 3- or/and 4-position (compare [137-139] for a review of modern syntheses of PTs), poly-3-alkyl-thiophenes (P3ATs) so far attracted greatest interest with applications in OFETs [140-142], sensor systems [143],[144] and organic solar cells [105],[145]. A

notable exception in this regard is PEDOT (Poly-3,4-ethylenedioxythiophene), historically used as an antistatic coating for celluloid films [146]. A variety of highly conductive dispersions (usually PEDOT-PSS (compare Figure 16) in water based solutions) are available from numerous manufacturers (e.g. H. C. Starck (Clevios®), Agfa (Orgacon®)). PEDOT-PSS films are used as e. g. transparent polymeric electrodes, hole injection layers in OLEDs, or as electron blocking layer in plastic photovoltaics [110]. As the building block in P3ATs is non-symmetric, several regiochemical possibilities arise when combining P3AT monomer units (compare Figure 17).

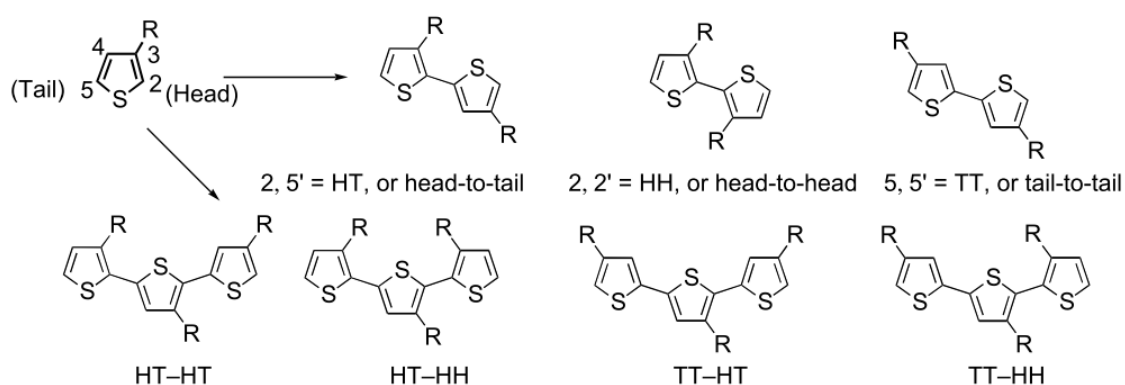


Figure 17: Coupling of 3-substituted thiophene units in different geometries [147]

In regioirregular compounds (containing 2,2' i.e. head-to-head couplings) the vicinity of the side groups causes a torsion of the polymer backbone reducing π -overlap, hence transport properties are inferior compared to regioregular structures (2,5' or head-to-tail coupling) [147]. When synthesis- and production parameters [105] are well controlled, P3ATs are excellent solar cell materials, combining high carrier mobility (mobilities of up to $0.1 \text{ cm}^2 \cdot \text{V}^{-1} \cdot \text{s}^{-1}$ are reported for P3HT [148]) and good stability, making P3HT-PCBM the most researched materials system in organic photovoltaics.

3.1.3 Copolymers – Low Bandgap Polymers

One of the initial driving forces in developing new polymeric conductors for plastic photovoltaics was bandgap reduction, in the quest of a synthetic metal with zero bandgap (which, however, is unrealistic due to Peierls distortion / Jahn Teller effect [149],[150]). A

review of Roncali points out the various options for band engineering on a molecular scale, with contributions from bond length alternation (BLA), resonance energy (RES), substituents (SUB), torsional angle (θ) and intermolecular contributions (inter) to the bandgap [132]:

$$E_g = E_{BLA} + E_{RES} + E_{SUB} + E_{\theta} + E_{inter} \quad \text{(VIII)}$$

Practically a huge variety of low bandgap polymers was synthesized for plastic PV applications, as is elaborated in several excellent reviews [151-153]. Polyfluorene copolymers were amongst the first copolymer-materials which were tested as donor phase, e.g. polymers of the APFO family or F8T2 [154],[17].

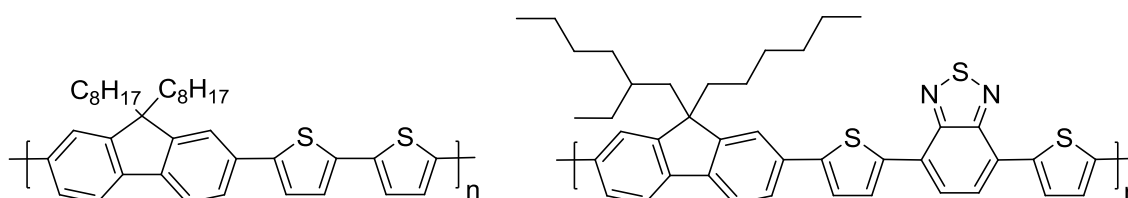


Figure 18: Structures of F8T2 and APFO-3 [154],[17]

A review by Cheng et al. [155] giving an overview of the most common building groups on low-bandgap systems used in plastic photovoltaics facilitates the task of keeping track of the numerous (successfully used) systems.

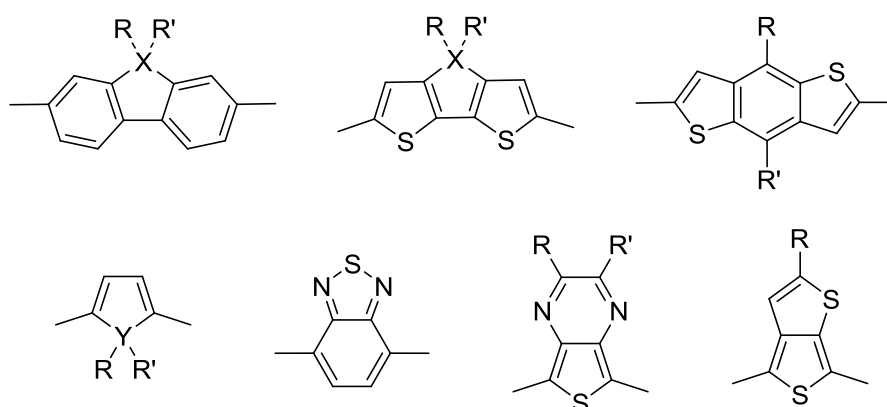


Figure 19: Frequently used building blocks of low bandgap polymers in photovoltaics (X = C, N, Si; Y = S, Se, Si); upper row: fluorene (X=C), BDT (benzo(1,2-b:4',5'-b)dithiophene); lower row: thiophene (Y=S), benzothiadiazole, thieno(3,4-b)pyrazine, thieno[3,4-b]thiophene

Fluorene based polymers (upper left in Figure 19, X = C) in combination with a thiophene-acceptor-thiophene unit are the building blocks for APFO-type polymers, when a N-(heptadecan-9-yl)-carbazole block is used instead of the fluorene unit in APFO-3 (Figure 18), PCDTBT (poly[N-9''-hepta-decanyl-2,7-carbazole-alt-5,5-(4',7'-di-2-thienyl-2',1',3'0-benzothiadiazole)), is obtained, which was very successfully used in plastic solar cells [156]. An alternating copolymer of BDT and a thienothiophene acceptor (Figure 19) was used in a device with a PCE of 7.4 %, illustrating the potential of low-bandgap donors for plastic solar cells [33].

Table 4: FO energies and bandgap values and mobilities for selected conjugated polymers

material	E_g / eV	HOMO / eV	LUMO / eV	μ / $\text{cm}^2 \cdot \text{V}^{-1} \cdot \text{s}^{-1}$	Ref.
PPV	2.5	5.2	2.7	n.d.	[157]
MEH-PPV	2,2	5,0	2,8	$1e^{-4} - 1e^{-3}$	[73]
MDMO-PPV	2,5	5,3	2,8	n.d.	[78]
P3HT	1,7	5,2	3,6	$1e^{-6} - 1e^{-4}$	[148]
P3EBT	1,9	5,70	3,65	n.d.	¹ (see footnote)
F8T2	2,93	5,41	2,48	$2e^{-4}$	[158],[159]
APFO-3	2.3	3.4	5.7	n.d.	[160]
PCDTBT	1.85	3.6	5.45	$1e^{-3}$	[161]

3.2 Acceptor Phases

In the following, acceptor phases used in the present work will be briefly described. After a section on fullerene based materials, the basic properties of ZnS, CdS and CuInS₂ are briefly reviewed.

3.2.1 Fullerene Based Acceptors

Since its discovery in 1985 the C₆₀ molecule and its derivatives have been thoroughly explored, ending up with applications in materials chemistry [162],[163], biochemistry [164] and biology [165]. C₆₀ fullerene is a strong electron acceptor which can take up up to 6 electrons [166],[167] and an efficient fluorescence quencher as was demonstrated in

¹ determined by CV (Appendix 10.1)

1992 by Sariciftci et al. in combination with MEH-PPV [9]. After a patent filed in 1992 [168], the first polymer-fullerene paper was published in 1993 [169]. Due to mediocre solubility of C₆₀ in many common solvents, chemically modified fullerenes are most commonly used in solution processing for organic electronics, among the numerous derivatives already synthesized [170],[91], PCBM ([6,6]-phenyl-C₆₁-butyric acid methyl ester (i=60, 70)) is by far the most popular. Higher fullerenes (C₇₀, C₇₆, C₇₈, C₈₄ and C₉₀ structures are known) show different absorption behaviour compared to C₆₀, due to the lower symmetry there are allowed transitions in the Vis-region with extinction coefficients of $\epsilon \sim 1e^4.cm^{-1}$, whereas C₆₀ is only weakly absorbing in the visible region [171]. Application in solar cells however is limited to C₇₀-species, as availability of higher fullerenes is very limited and optically pure samples are difficult to obtain for the C₇₆ and C₇₈ compounds (5 resp. 24 known isomers [172]).

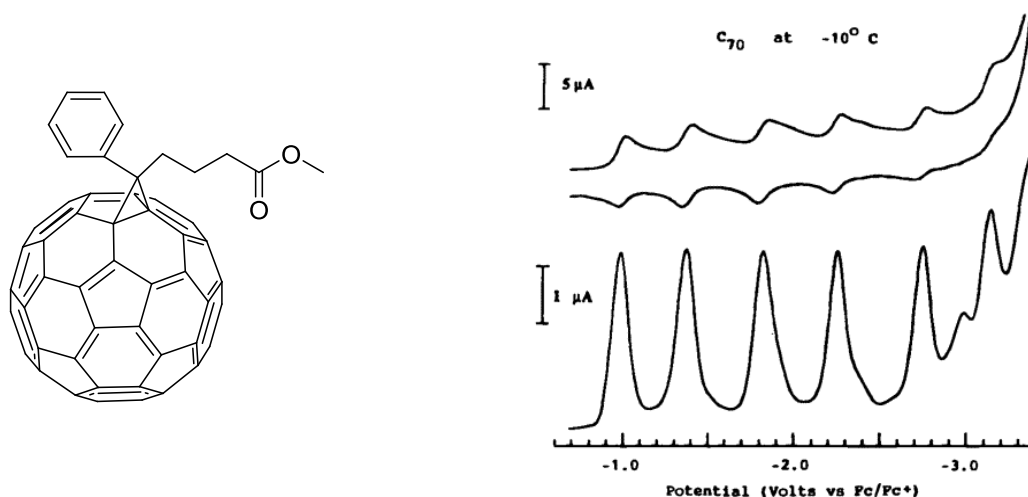


Figure 20: C₆₀-PCBM (right side) and cyclic voltammogram of C₇₀ in acetonitrile-toluene [173]

3.3 Semiconductor Acceptors

3.3.1 ZnS

Zinc sulfide is a well known wide bandgap semiconductor ($E_g = 3.6$ eV (direct bandgap, bulk value for sphalerite) [174]) with two polymorphs, sphalerite (cubic) and wurtzite (hexagonal). It is an efficient phosphor and widely used in optoelectronic applications as a detector material or in CRTs [175], ZnS-CuInS₂ heterojunctions play an important role in CdS-free CIGS thin film solar cells [176],[177]. Numerous publications report on synthesis and application of nano-scaled ZnS [178-180], application of in hybrid solar cells however is limited due to the large bandgap of the compound.

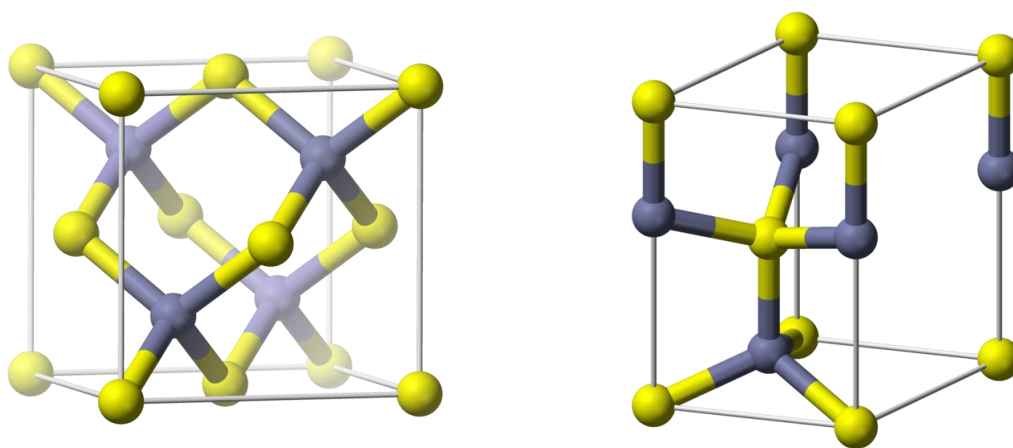


Figure 21: Sphalerite and wurtzite unit cells (Zn: grey, S: yellow)

3.3.2 CdS

Cadmium sulfide is direct bandgap semiconductor with a bandgap of 2.4 eV [174] showing hexagonal wurtzite (the predominant modification) or cubic sphalerite structure. It shows pronounced photoconductivity and is correspondingly used as photoresistor, other applications include transistors, CRTs, phosphors and pigments [175],[181],[182]. It can be used as a solar cell material (one of the first solar cells published in 1954) together with p-type Cu_xS [183], is employed as interface layer in CIGS thin film solar cells [184],[185] and has been used in efficient hybrid solar cells [34],[186],[187]. Its sister compound, CdSe is

one of the most widely studied semiconductors in nanotechnology and, due to the favourable bandgap of 1.73 eV intensively studied as active layer material in hybrid solar cells [188],[20],[189].

3.3.3 CuInS₂

CuInS₂ (CIS) is a direct semiconductor with a bandgap value of 1.53 eV [190], that is, near the optimum value of 1.3 eV predicted for a single bandgap absorber (Shockley-Queisser limit [191]). Development of CIS was inspired by early promising results on CuInSe₂, 12.5%-efficient CuInSe₂-CdS heterojunction solar cells were fabricated as early as 1975 [192],[193]. Modern thin film solar cells utilizing this materials system often are referred to as CIGS-cells, a compound semiconductor of Cu, In, Ga, S and Se is used in a heterojunction with a CdS, In₂S₃, ZnS or ZnO buffer layer on molybdenum substrates [35]. Variation of the stoichiometry allows to vary the bandgap from 1.0 eV (CuInSe₂) to 1.68 eV (CuGaS₂) or to produce bandgap graded absorber layers. Despite inferiority compared to CuInSe₂, CuInS₂ was developed as a solar cell material, high radiation endurance, the possibility to manufacture flexible modules and cheaper raw material (S instead of Se) makes the material an interesting candidate for (spacecraft-) solar cell applications [194]. Whereas the material is very well researched in context with thin film solar cells and nanoscience, very few reports exist on application in hybrid solar cells (e. g. Arici et al. report on CuInSe₂- polymer and CuInS₂ -polymer solar cells [195],[196]).

CuInS₂ compound has a tetragonal unit cell and shows chalcopyrite structure at ambient conditions. The compound is stable in a quite wide range of stoichiometries in the pseudo-binary system CuS – In₂S₃ [197]. Intrinsic CuInS₂ films show high resistivities, deviation from stoichiometry (Cu-excess results in p-type compounds, In-excess in n-type compounds; $\{([Cu] + 3[In]) / 2[S]\} - 1 \gtrless 0$ (> 0 : n-type, < 0 : p-type) [194]) results in films with higher conductivities; thin film solar cells generally use p-type CuInS₂ as absorber. Moreover the material exhibits a complex defect chemistry (defect concentrations in the order of $> 1e^{19} \text{ cm}^{-3}$ in doped CuInS₂), which is still not fully understood, especially its implications on heterojunction formation and solar cell action [198-201].

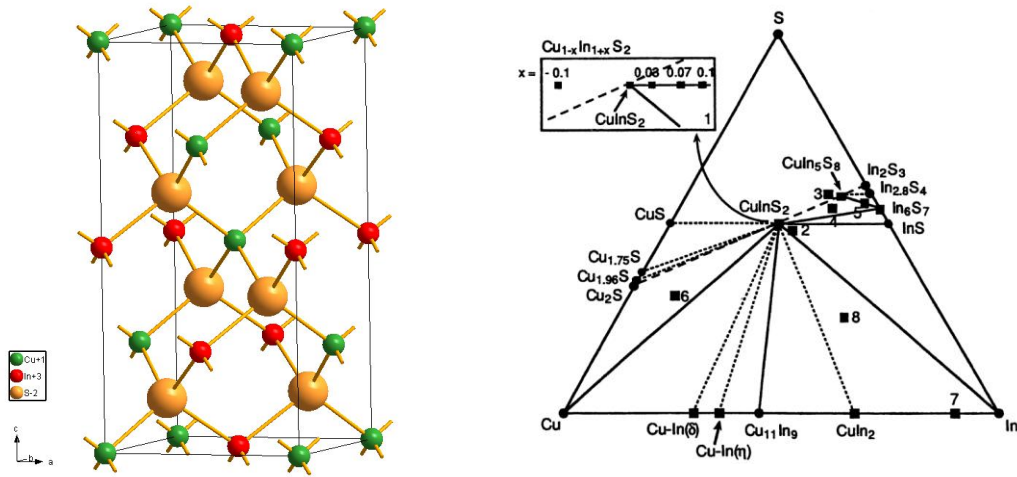


Figure 22: Chalcopyrite-type unit cell of CuInS₂ (left) and ternary phase diagram of the Cu-In-S system [194]

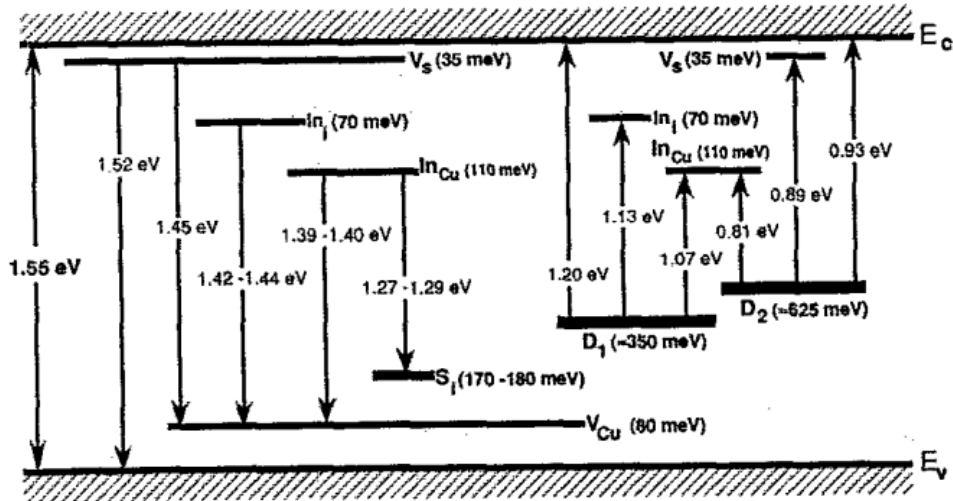


Figure 23: CIS defect levels determined by Brewster-angle- / photoluminescence spectroscopy [201]

CuInS₂ – ZnS System

Incorporation of an additional metal species into the semiconductor lattice causes a modification of the optoelectronic properties of the material, e. g. the incorporation of Cd in Ag-doped ZnS can be used to tune the emission from the UV to the Vis region of the spectrum [202]. For CuInS₂ incorporation of a variety of elements including Sn [203], As, P, Sb [204], Mn [205], Mg, Cd and Zn has been demonstrated, application in thin-film solar cells was shown for CuInS₂:Cd, CuInS₂:Zn and CuInS₂:Mg alloys [198],[206-208].

Depending on valence, size and position of the inserted metal, p- or n-type conductivity can be observed, e. g. Zn- and Cd-insertion into the host lattice result in n-type CIS [206], which can be utilized in buried layer homojunction devices or as electron conducting acceptor phase in hybrid solar cells. Phase relations in the $\text{ZnS}_{2x}\text{-CuIn}_{1-x}\text{S}_2$ (ZCIS) system show chalcopyrite structure for $0 \leq x \leq 0.05$, for $0.05 \leq x \leq 0.2$ a two phase region exists, with tetragonal domains contained by a cubic matrix [209],[210]. A systematic study of the bandgap as a function of ZnS content revealed no substantial increase in the E_g -value until $x \leq 0.15$ ($E_g[(\text{ZnS})_{0.3}\text{-CuIn}_{0.85}\text{S}_2] = 1.57$ eV), at higher Zn-contents sphalerite bandgap of 3.6 eV is approached [207]. Application of ZCIS in thin film solar cells resulted in slightly increased V_{OC} -values, whereas serial resistivity of the devices increased [208].

4 Experimental

4.1 Preparations

Precursor / Polymer Solutions: Detailed description in the respective sections (sections 5.2, 6.2, 7.3, 7.4, 7.5 and 7.7)

Spin Coating: Spin coating of various layers was performed on a Karl Süss CT 62 spincoating unit. Detailed parameters of speed and acceleration are given in the respective sections. Solar cell active layers / anode interlayers were prepared on ITO-coated glass slides, which were received from Delta Technologies® (surface resistivity: 20-25 Ω / sq.).

Drop Coating: Sample preparation for experiments (TGA, MS, FT-IR, XRD) requiring high sample amounts (> 10 mg or thick layers) was performed by drop coating of the substance / precursor of interest the proper substrate. Typically, samples were dried in vacuum atmosphere in order to remove (part of) the solvent. Depending on experiment, the film was measured as prepared (FT-IR) or scraped off and then subject to the respective measurement.

Air Brushing: Part of the XRD-data was obtained directly from the film (sections 6.1 and 7.6.2). In order to ensure sufficient film thickness, typically 500 μ L of the precursor solution were air-brushed onto Si-wafers.

Curing / Annealing of Layers: PEDOT-PSS layers were cured in a N₂-containing glove box on a magnetic stirrer. Annealing of PPV-CIS layers was performed on a ceramic heating plate. P3EBT-metal-sulfide layers were annealed using a tube furnace (Heraeus Ro 4/25, Heraeus Re 1.1 controller).

Evaporation of Cathode Layer: Al-cathode layer was evaporated using a BalTec® MED-010 or BalTec MED-020 evaporation unit. Film thickness (typically 100 nm) was determined by means of a quartz micro balance, cathode area was 10 mm² unless otherwise stated.

Encapsulation of Solar Cells: Solar cells were encapsulated using a commercially available two-component epoxy resin (UHU® plus 5 min epoxy), which was used to adhere the device to the soda-lime glass cover (glass-glass epoxy encapsulation). The electrodes were contacted with aluminium stripes by means of conductive silver paint.

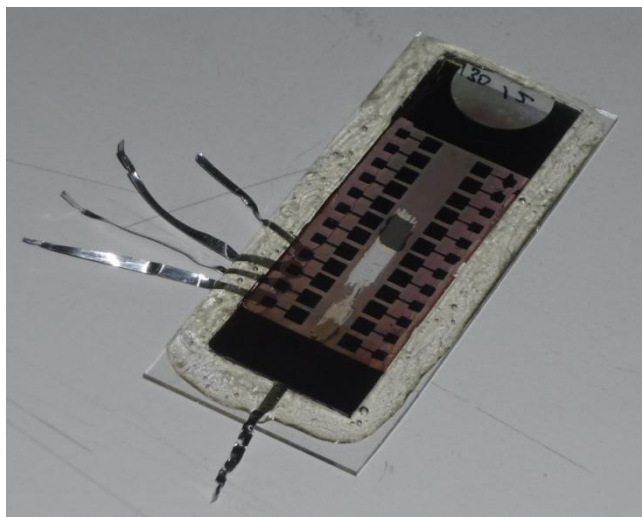


Figure 24: Encapsulated hybrid solar cell array

4.2 Instrumental

UV-Vis Spectra: Transmission spectra were obtained using a Shimadzu® UV-1800 spectrometer. Spectral data is represented in terms of absorbance, however the data were not corrected for contributions due to reflexion / scattering.

FT-IR Spectra: Transmission spectra were recorded using a Perkin-Elmer® Spectrum-One spectrometer. Data were analyzed (baseline correction, determination of peak area) using Perkin-Elmer Spectrum®-5.0 software.

TGA Analysis / Mass spectrometry: TGA-MS measurements were performed using a Netsch TG 449 F3 Jupiter® STA unit, which was coupled with an QMS 403 C Aëolos® quadruple mass spectrometer. Helium was used as carrier gas, mass spectra were obtained from 15-300 m/z. Samples were prepared by drop coating and scraped off for the measurement. Data evaluation was performed using Netsch Proteus-4 software.

Mass spectrometry was performed using a Waters Micromass GCT Premier spectrometer (EI ionisation, TOF mass analyzer). Samples were analogous to the STA-experiments, positioned onto a glass capillary and heated in the sample chamber. Data were analyzed using Waters MassLynx™ software.

XRD Data: Powder-diffraction data of polymer-metal sulfide composites were obtained using Siemens D-5005 (section 5) and Bruker D8 Discover (in combination with a Anton Paar Domed Hot Stage DHS900, section 7.6.2) powder diffractometers (Cu-K_α-source in all cases). Except for sections 6.1 and 7.6.2 (air brushing of samples, measurement as film) samples were prepared by drop coating and scraped off for the measurement. Data were analyzed using Bruker Diffrac-PLUS 2006 software. Primary crystallite sizes were estimated using the Scherrer relation,

$$d_{XRD} = \frac{K \lambda}{\Delta(2\theta) \cos \theta} \quad \text{(VIII)}$$

with $\Delta(2\theta)$ is the full width at half maximum (FWHM) of the peak in radians, 2θ is half of the scattering angle 2θ , λ the wavelength of the X-rays, and K is the shape factor ($K = 0.9$ for spherical particles).

CV: Cyclic voltammetry measurements were performed using an Autolab PGSTAT100 potentiostat at a sweep speed of 10 mV/s. The polymer was measured as thin film on a Pt-electrode, counter electrode was Pt and Ag/AgNO₃ served as reference electrode. Measurements were done using a acetonitrile-TEABF electrolyte, the system was referenced to Fe(cp)₂.

GPC: Weight average molecular weight (M_w) was determined using gel permeation chromatography on polymer-CHCl₃ solutions. STV-Gel columns (mean adsorbent diameter 5 μm) were loaded by a Merck-Hitachi L6200 Intelligent Pump, detection was performed using a Wyatt Technologies Optilab DSP differential refractometric detector. The setup was calibrated with polystyrene standards from Polymer Standard Service.

Electron Microscopy: SEM and SEM-EDX measurements were obtained using a Zeiss-Ultra 55 instrument. Transmission electron microscopy (TEM) investigations and selected area electron diffraction (SAED) patterns were acquired from a Tecnai 12 microscope (FEI Company, 120kV, LaB₆ Cathode). High resolution TEM-micrographs were obtained from a Tecnai F 20 microscope (FEI Company, 200 kV, Schottky emitter) equipped with a monochromator (FEI Company), a Gatan energy filter system and an UltraScan CCD camera.

I-V Measurements: I-V curves were obtained in a N₂-containing glovebox using a Keithley®-2400 source measurement unit operated by a custom made LabView® software. The solar cells were illuminated using a Philips® 150W GX5.3 Focusline halogen bulb (no spectral mismatch correction). Homogeneity was ensured using several scattering disks, intensity of the incoming light was set to 1000 W.m⁻² (determined using a KippZonen®-CMP-11 pyranometer).

EQE-Spectra: IPCE-measurements were obtained using a custom-made setup consisting of a Xenon-arc lamp and an AMKO Multimode-4 monochromator. After the monochromator, photons are guided to the device using a light-pipe, incoming intensity of the monochromatic light was determined using a calibrated Hamamatsu S1226-18BQ photodiode. The photocurrent of the tested device at a defined wavelength of the incident light was monitored using a Keithley®-2400 source measurement unit, the setup was controlled by a custom made LabView®-program.

4.3 Construction of a Multi-Channel Stability Testing Appliance

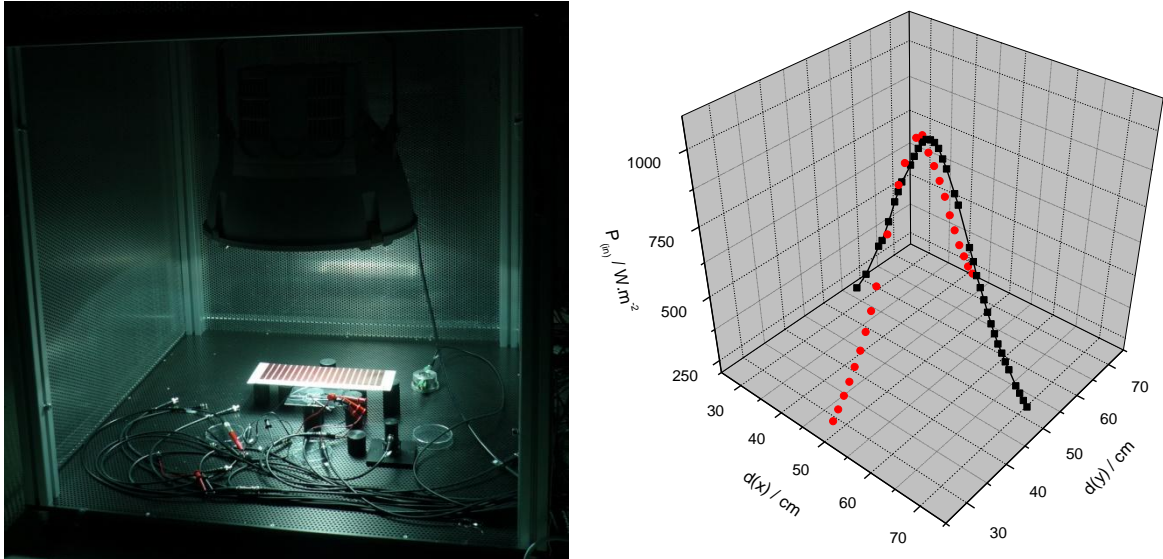


Figure 25: Photograph of permanent testing appliance (left), lateral intensity of the light source at sensor height (76 mm) (right)

Besides enhancement of PCE, one of the remaining issues to be resolved for organic solar cells to be market-ready is the increase of their operational lifetime. In order to address this topic, a multi-channel facility for permanent testing has been constructed, requirements were as follows:

- multi-channel testing
- testing in various operational modes of the device
- logging of light intensity / temperature

This was realized by using a setup consisting of a Keithley®3706-switch combined with a 3730 6x16 two-pole matrix card, which can be operated by up to six source-measurement units. Illumination intensity information was gained from a calibrated photodiode (Hamamatsu S1226-18BQ), which was referenced to the light source (LG PSH-07 sulfur plasma source) with a KippZonen® CMP-011 pyranometer, temperature information was obtained from a Pt-100 element connected to the digital multimeter unit of the switch.

Finally, a cage with an anodized aluminium ground plate with defined sample positions and dual-adjustment for the height of the light source was constructed for exact positioning of the devices.

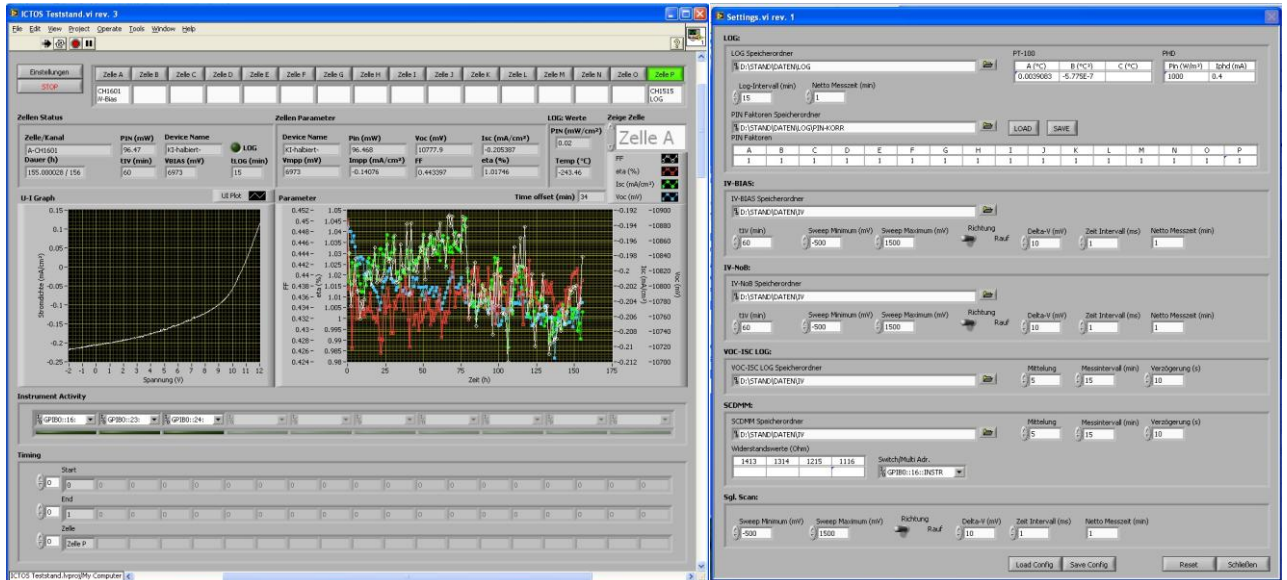


Figure 26: Screenshots of the stability-testing software; right side: operational display containing channel overview and results; left side: parameter settings

The software (programmed at Johanneum Research Forschungsgesellschaft m. b. H.) consists of three modules: (1) Logging of intensity / temperature, (2) non-biased testing, (3) biased testing of solar cells (either at defined voltage value or bias at actual mpp). Solar cell parameters are extracted automatically and logged vs. time. Device-name, -area, -position and testing time are input parameters; measurement range, -speed, -direction, -interval and frequency can be adjusted to the actual requirements in the settings menu.

4.4 Chemicals

All chemicals used are listed in Table 5. Unless otherwise stated, no extra purification steps were performed.

Table 5: List of chemicals

compound	purity, description	supplier
Acetonitrile	> 99.9%, Chromasolv Plus	Sigma-Aldrich
Cadmium-II-acetate.xH ₂ O	99.99%	Aldrich
Chloroform	99.9%, Chromasolv Plus	Aldrich
Copper-I-acetate	97%	Aldrich
Copper-I-chloride	anhydrous, ≥99.99%	Aldrich
Copper-II-chloride	99.999%	Aldrich
Copper-I-iodide	> 99%, purum	Riedel-deHaen
Indium-III-acetylacetonate	99.99%	Aldrich
Indium-III-chloride	100.00%	Aldrich
Lead-II-thiocyanate	99.99%	Aldrich
MEH-PPV	average M _w = 40000–70000 g.mol ⁻¹	Aldrich
MDMO-PPV		H. W. Sands
P3HT, Sepiolid P100	average M _w = 50000 g.mol ⁻¹	Rieke Metals / BASF
Poly(p-xylene tetrahydrothiophenium chloride)	0.25%, solution in H ₂ O	Aldrich
Pyridine	99.9%, Chromasolv Plus	Sigma-Aldrich
Thioacetamide	99.0%, ACS reagent	Aldrich
Thiourea	99%	Lancaster
Zinc-II-acetate	99.99%	Aldrich

5 Preparation of Binary Semiconductor - Conjugated Polymer Composites and Solar Cells

5.1 Introduction

This section deals with the preparation of nano-structured blends consisting of metal sulfides and conjugated polymers. The inorganic semiconductor is obtained directly within the matrix of the conjugated polymer using an in-situ solid state process.

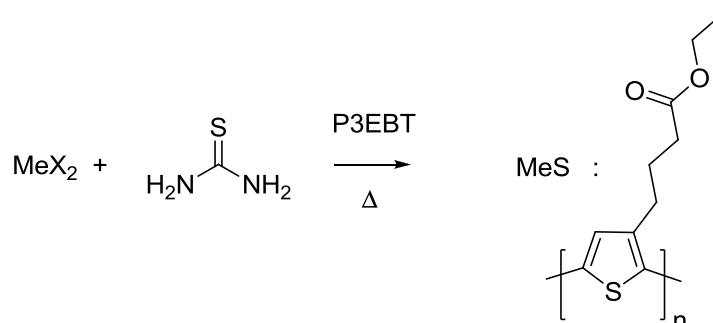


Figure 27: Reaction scheme for metal-sulfide - P3EBT composites

Thiourea (TU) is decomposed during a moderate heating step and is reacting with metal ions dispersed within the polymer (a more detailed description of the decomposition process is given in section 7.6). Overall, a composite consisting of an inorganic and an organic semiconductor is formed. By proper choice of materials and reaction conditions, nanostructured networks of the components are accessible. In this work, organic-inorganic blends consisting of P3EBT (poly-3-ethylbutanoate)thiophene and CdS, PbS or ZnS, respectively, were prepared. As prepared layers were used as active layer in bulk-heterojunction hybrid solar cells and were characterized optically. The structure of the composites was studied using XRD, TEM and AFM, the formation of the blend was studied using TGA.

5.2 Experimental

A precursor solution containing the respective metal salt, thiourea and the polymer was prepared by mixing the components in pyridine. Concentrations were chosen in a way that, given complete reaction, concentration of the components is $24 \text{ mg}\cdot\text{mL}^{-1}$ metal sulfide and $6 \text{ mg}\cdot\text{mL}^{-1}$ P3EBT, i.e. donor-acceptor ratio is 1/4. Following sequence was maintained during the preparation of the solutions to ensure good stability of the precursor: (1) metal salt + pyridine (following metal salts were used: $\text{Cd}(\text{Ac})_2 \cdot 1.08\text{H}_2\text{O}$, $\text{Pb}(\text{SCN})_2$, $\text{Zn}(\text{Ac})_2$), (2) P3EBT, (3) TU. Water content in $\text{Cd}(\text{Ac})_2 \cdot n \text{H}_2\text{O}$ was determined to be 7.8%, that is $n=1.08$.

Table 6: Concentrations and proportions of the precursor solutions

	$c(\text{P3EBT})/\text{mg}\cdot\text{mL}^{-1}$	$c(\text{MeX}_2)/\text{mg}\cdot\text{mL}^{-1}$	$c(\text{MeX}_2)/\text{mmol}\cdot\text{mL}^{-1}$	$c(\text{TU})/\text{mg}\cdot\text{mL}^{-1}$	$c(\text{TU})/\text{mmol}\cdot\text{mL}^{-1}$
CdS-P3EBT	6	41.5	0.17	63.2	0.85
PbS-P3EBT	6	32.6	0.10	38.2	0.50
ZnS-P3EBT	6	45.3	0.25	93.7	1.25

Precursor solution was coated onto suitable substrates (ITO-coated glass for hybrid solar cells and AFM samples, borosilicate glass for TGA and XRD measurements, NaCl single crystals for TEM samples), for the TEM-, and XRD- preparations the solution was diluted with pyridine 1/1 (vol) with pyridine. Layers were prepared by spin coating (hybrid solar cells, optical spectra, AFM) or drop coated (XRD) and subsequently heated in a tube furnace under vacuum using the following routine: $\text{RT} \xrightarrow{3 \text{ min}} 80^\circ\text{C} \xrightarrow{20 \text{ min}} 180^\circ\text{C} \xrightarrow{10 \text{ min}} 180^\circ\text{C}$. After the heating process the tube was removed, flooded with nitrogen and cooled down to RT within about 30 minutes. Solar cell cathode was made of aluminium (200 nm), which was evaporated using BalTec MED010 or MED020 at a pressure of ca. 10^{-6} torr.

5.3 Results and Discussion

5.3.1 P3EBT-CdS Composites

Structural Characterization

Figure 28 shows the diffraction pattern of the P3EBT- CdS composite. A comparison with the reference data (PDF Nos. 00-41-1049, 00-010-0454) reveals that from the two possible modifications of CdS only the hexagonal one is formed; the three peaks characteristic for wurtzite around 28° 2theta are present and no reflections from the cubic phase occur in the pattern. This is in good agreement with the SAED-data (Figure 29). SAED pattern too shows a very feature-rich diffraction pattern, with all major reflections of hexagonal CdS present in the measurement. Broadness of reflections implies a small material structure, using Scherrer formula and the (012) reflection at 36.70° 2theta, primary crystallite size is estimated to be 4.3 nm.

TEM micrographs (Figure 29) show a network of spherical CdS-particles within the polymer matrix. Particle diameters appear rather uniform and are in the range of 5-10 nm, which is a favourable length-scale for application in hybrid photovoltaics. HR-TEM shows the view onto an elongated nanoparticle, the measured spacing of 0.336 nm corresponds to the (002) plane spacing.

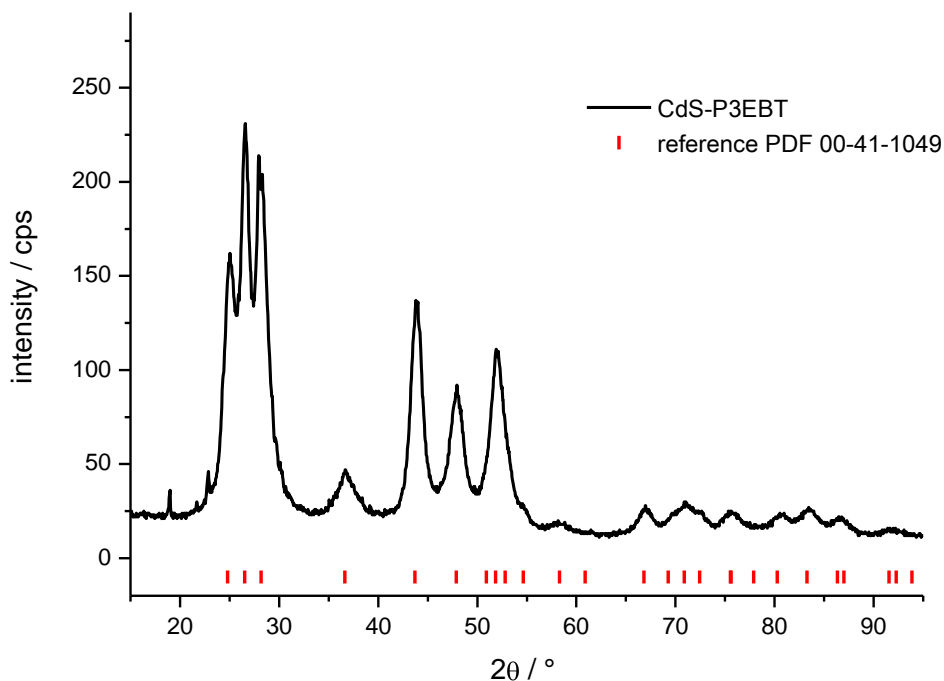


Figure 28: Diffraction pattern of P3EBT- CdS composite

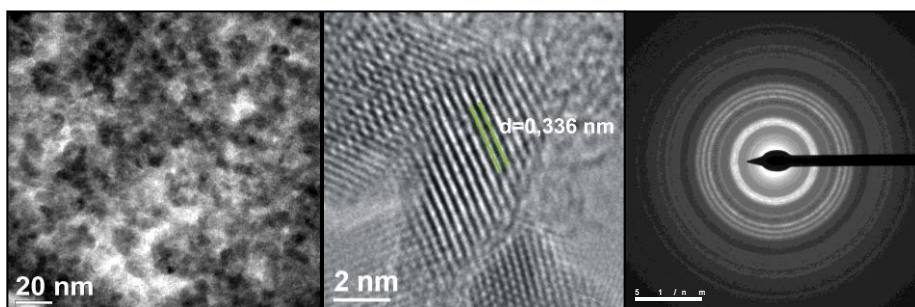


Figure 29: TEM, HR-TEM micrographs and SAED of the P3EBT-CdS composite

Hybrid Solar Cells and Optical Properties

Absorption properties of P3EBT-CdS blends were investigated by UV-VIS spectroscopy. Additionally to the 4/1 blend used as solar cell active layer, the 1/1 blend and a pristine P3EBT layer was investigated in order to elaborate the contribution of the inorganic phase with respect to absorption.

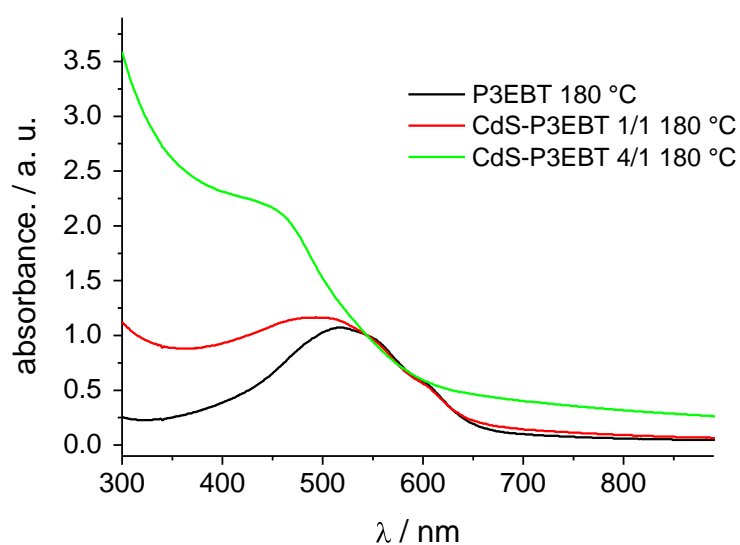


Figure 30: UV-VIS spectra of different P3EBT-CdS composites

In the 1/1 blend, there is an increased absorption at short wavelengths, but no additional features are present. CdS-P3EBT films with 4/1 ratio however show a strong increase of the absorption in the blue and display additional features in the absorption spectrum, indicative of excitonic states involved in the optical transitions [211]. Elevated baseline of the 4/1 blend is attributed to enhanced scattering effects by the high proportion of

nanoparticles within the material. Solar cells were built using the 4/1 precursor solution. A reasonable photovoltaic effect was observed, with efficiencies close to 0.1%.

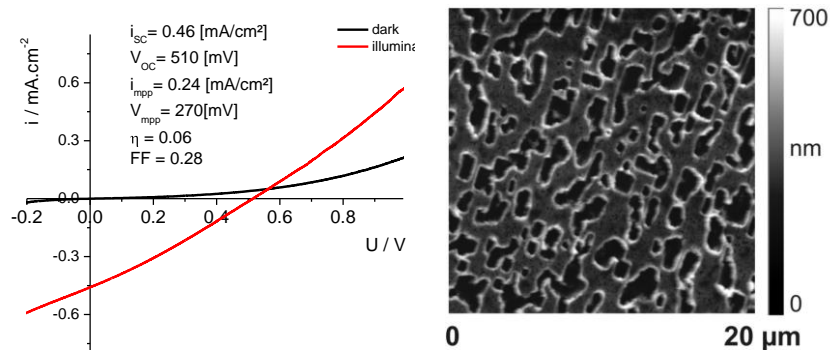


Figure 31: i-V curve and surface topography of P3EBT-CdS solar cell

An AFM tapping mode image of a solar cell active layer (Figure 31) shows a very rough surface and the formation of super-structures with length scales in the 10 μm regime. Negative implication on photovoltaic activity is possible, but superstructure action is still not fully understood. Figure 31 shows the i-V curve of a CdS-polymer solar cell. The small slope of the dark curve in forward bias implicates high serial resistivity of the device, FF value is correspondingly low (0.28). Current density of 0.5 mA and V_{OC} of 510 mV however are promising, though further optimization work is needed.

5.3.2 P3EBT-PbS Composites

Structural Characterization

Sample structure was characterized using XRD and TEM. Figure 32 shows XRD and TEM measurements of the sample. The XRD pattern shows no pronounced peak broadening, this indicates that primary crystallite size is above 100 nm. Peak positions are in very good agreement with the reference file PDF 00-005-0592, i.e. cubic Galena-type lead sulfide is obtained (which, actually is the only modification of PbS reported in the literature). This picture is consistent with the TEM data; TEM brightfield image shows crystals with diameters in the range of 0.5-1 μm . SAED reveals a single crystal diffraction pattern of a particle oriented on the [0 0 1] axis. Applicability as solar cell active layer is questionable:

differently to the CdS-P3EBT blends, particles are poorly connected and exhibit diameters in the micron range. In absence of quantum confinement effects (exciton Bohr radius in lead sulfide is 18 nm [212]) the bandgap remains at its bulk value of 0.4 eV, correspondingly no photovoltage can be expected by this material. For this reason no further investigations were performed on this material system.

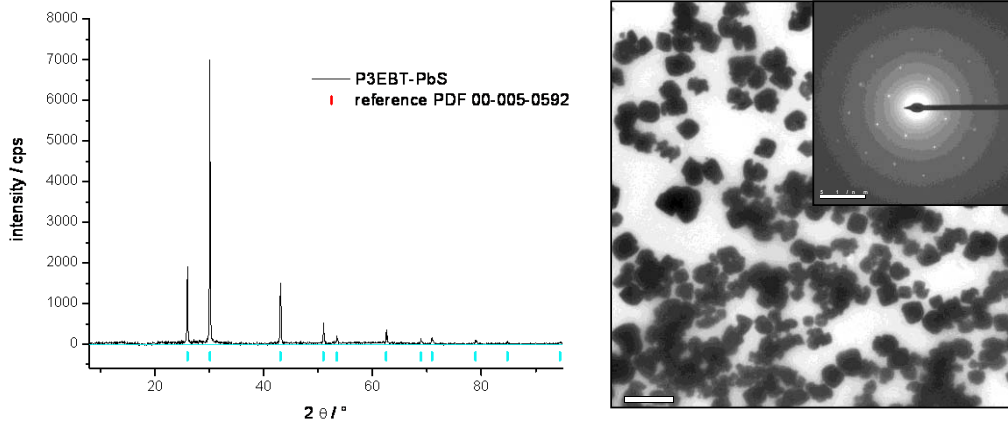


Figure 32: XRD and TEM-data of P3EBT-PbS composite structures

5.3.3 P3EBT-ZnS Composites

Structural Characterization

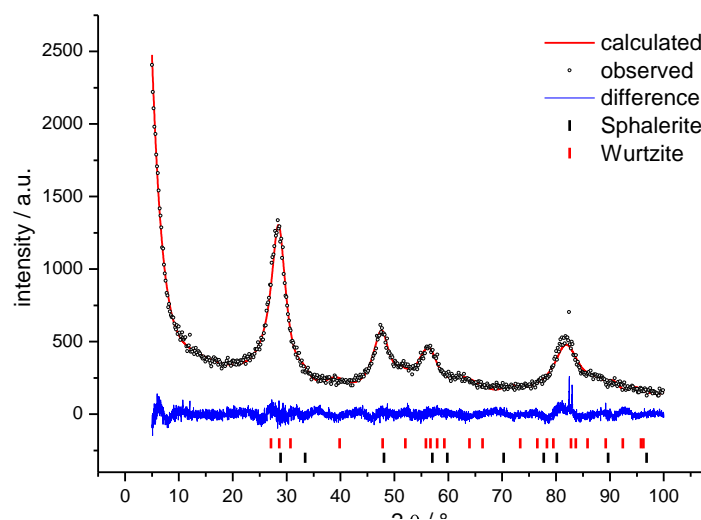


Figure 33: XRD-pattern of the P3EBT-ZnS composite

Analogous to P3EBT- CdS blends, P3EBT-CdS layers were obtained using zinc acetate as metal salt. A XRD-pattern of the nanocomposite material is shown in Figure 33. The main peaks are in good accordance with the main peaks described from the reference file PDF 00-005-0566 for sphalerite ZnS. The broadening of the peaks already indicates that the primary crystallites are also in the nanometer range. From the half-width of the (113) - reflection at $56,32^\circ$ 2θ , a primary crystallite size of 4.6 nm is estimated using the Scherrer equation. A thorough examination of the XRD-pattern shows that the peak at approximately 82° 2θ as well as the small peak at 52.4° 2θ , are not in agreement with sphalerite structure. Therefore a Rietveld analysis of the pattern was performed using the two main ZnS modifications – cubic sphalerite and hexagonal wurtzite. The phase distribution is estimated to be roughly 80% sphalerite and 20% wurtzite. The calculated pattern is also presented in Figure 33 as well as the difference of calculated and observed data.

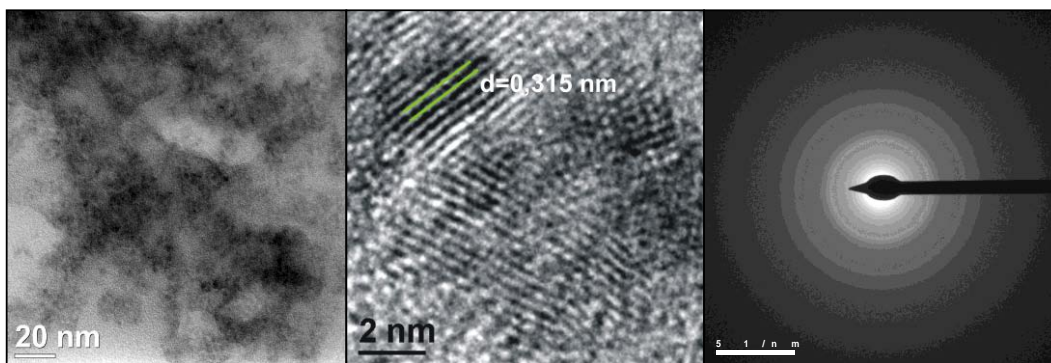


Figure 34: TEM, HR-TEM and SAED data for a P3EBT-ZnS composite

The corresponding TEM-data show rather diffuse aggregates of the ZnS nanoparticles and the polymer. Particles are of spherical shape and show diameters of ranging from 2 – 5 nm. SAED indicates sphalerite structure, with no apparent reflections from the wurtzite phase because of its low amount. HR-TEM of single particles reveals a plane distance of 0.315nm corresponding to (111) spacing.

Hybrid Solar Cells and Optical Properties

Figure 35 (left hand) shows the UV-VIS spectra of two different P3EBT-CdS layers (red line: 1/1 composite, green line: 4/1 composite) together with the absorption spectrum of P3EBT. Absorption is enhanced at short wavelengths, with an onset at 340 nm (i.e. 3.65 eV), a value very close to the sphalerite bulk-bandgap of 3.7 eV [213] and an additional feature at 300 nm (4.0 eV), which is attributed to an excitonic effect caused by the small diameter of the particles. It was possible to obtain devices showing a diode-like i-V curve, however photovoltaic output was infinitesimal. In this context it should be remembered that, contrary to e.g. CuInS_2 -hybrid solar cells, ZnS only acts as acceptor and electron transporting phase, with no contribution to photocurrent generation. The extraordinary low photocurrent values are attributed to the sparsely interconnected particles of the acceptor phase (compare Figure 34).

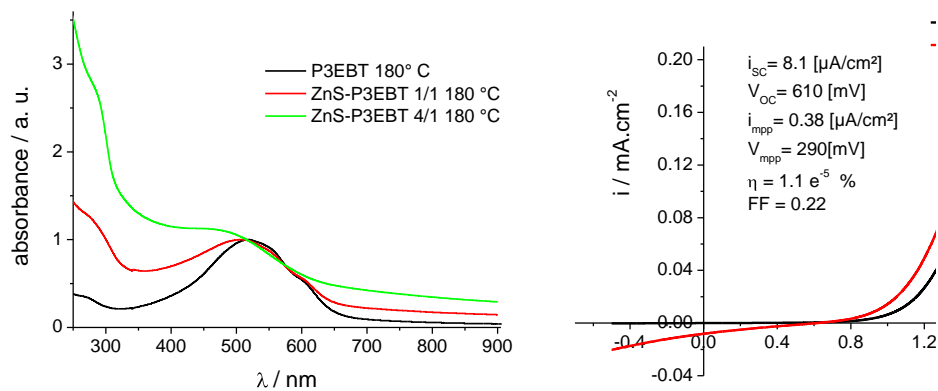


Figure 35: UV-VIS spectra of ZnS-P3EBT composites and i-V curve of a ZnS-P3EBT solar cell

5.4 Conclusion

In this section the formation of composites of a polythiophene and sulfide based semiconductors by an in-situ route was demonstrated. By thermal decomposition of thiourea in a polymer matrix (P3EBT) containing the respective metal salt ($\text{Cd}(\text{Ac})_2 \cdot x\text{H}_2\text{O}$, $\text{Pb}(\text{SCN})_2$ or $\text{Zn}(\text{Ac})_2$), organic-inorganic semiconductor layers were obtained. Structural

characterization by XRD and TEM methods demonstrated nano-scaled network structures for the CdS and ZnS composites, in case of the P3EBT-PbS blend microcrystalline PbS was obtained. Examination of layers prepared in the described fashion as photoactive layers in solar cells showed distinct photovoltaic action for the CdS-P3EBT material, ZnS-P3EBT showed infinitesimal photocurrents while the PbS blend did not work as a solar cell active layer. For application in hybrid solar cells further optimization is needed, adaption of the proposed in-situ route for different acceptor phases was demonstrated for binary sulfide-semiconductors and is also shown for CuInS₂ in chapter 7.

6 PPV – CuInS₂ Solar Cells

6.1 Introduction

Continuing previous efforts at the institute, first investigations on hybrid solar cells were performed on a system consisting of a non-substituted PPV-donor and an in-situ generated CuInS₂ acceptor. PPV is not soluble in common solvents and is generated by thermal decomposition of Poly(*p*-xylene tetrahydrothiophenium chloride) [214].

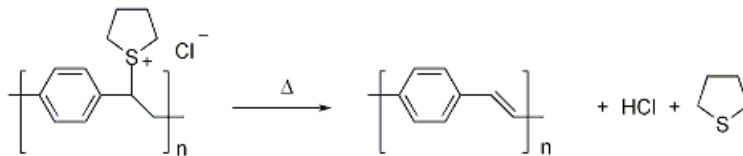


Figure 36: Thermal generation of PPV from the precursor

Device structure consists of a PPV-hole blocking layer on top of an ITO-coated glass substrate, followed by the active layer of a PPV-CuInS₂ blend and an aluminium cathode.

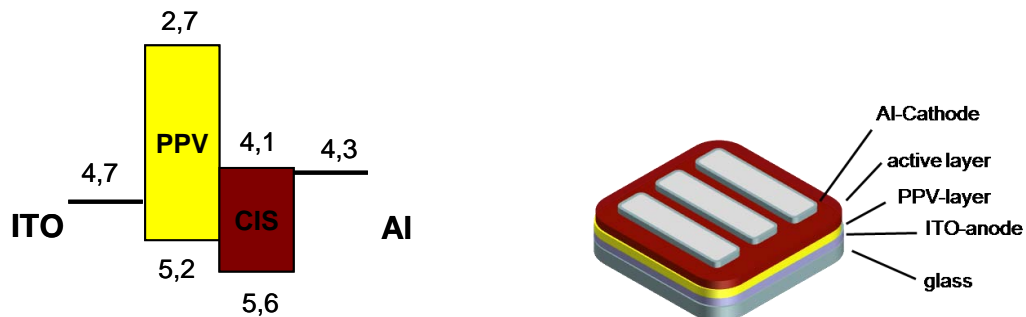


Figure 37: Energy bands (bulk values) and device structure for PPV-CuInS₂ solar cells

The acceptor phase is formed in-situ by thermal decomposition of thioacetamide (TAA), delivering a sulphur species, which is reacting with the metal ions present to form the inorganic species. TAA is a well known sulphur-delivering species widely used in wet-coating processes of binary semiconductors [215], its usage in chemical deposition of

ternary compounds is less frequent [216]. Depending on pH of the precursor solution used, the following mechanisms are possible for the decomposition in aqueous media:

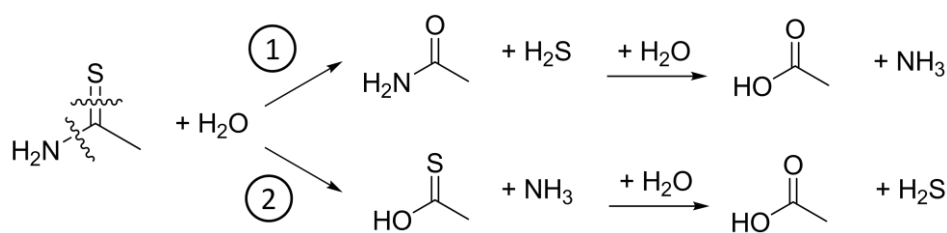


Figure 38: Reaction pathways of TAA in aqueous solution

In the regime of intermediate pH-values decomposition mechanism involving metal-ion-TAA complexes are also possible [217]. Only few work has been published on the chemical deposition of metal-sulfides using TAA from non aqueous media, e.g. Bi₂S₃ films were deposited on glass from an acetic acid-formaldehyde suspension [218].

6.2 Solar cell Preparation

Preparation of the precursor solution

Educts are contained in a pyridine-water mixture. CuI, InCl₃ and thioacetamide were dissolved in pyridine and added to the PPV-precursor (Poly(*p*-xylene tetrahydrothiophenium chloride), 0.25% w solution in H₂O). Concentrations and proportions of the components are summarized in Table 7 and were adapted from [23].

Table 7: Compositions of PPV-CIS precursor solution

	c(PPV-Prec) / mg.mL ⁻¹	c (CuI) / mg.mL ⁻¹	c (InCl ₃) / mg.mL ⁻¹	c(TAA) / mg.mL ⁻¹	PPV / CIS	Cu / In / TAA
PPV-CIS-4	0.22	0.31	1.82	1.85	1 / 4	1 / 5 / 15
PPV-CIS-7	0.22	0.55	3.19	3.25	1 / 7	1 / 5 / 15

Layer Deposition and Annealing

The hole blocking layer and the active layer as well were produced by drop coating. In a typical procedure, 150 μL of a 1/4 PPV-precursor – ethanole mixture were deposited with a sampler. This step was followed by annealing of the PPV-precursor under argon atmosphere at 150°C (t=15 minutes) on a ceramic plate. After cooling to RT, 100 μL of the active layer precursor solution were deposited as described and annealed at 200°C (argon atmosphere). The samples were cooled down and finally an aluminium cathode (d=200nm) was evaporated using a BalTec Med010 or Med020 evaporation unit.

i-V Measurements

i-V curves were measured in a glovebox with nitrogen atmosphere using a Keithley 2400 source-measurement unit. Samples were irradiated with a Philips halogen bulb at an intensity of 600 W/m^2 , irradiation intensity was determined using a photodiode.

6.3 Results and Discussion

6.3.1 Morphology and Structure of PPV-CIS Blend

Structural characterization of the active layer was performed by TEM and SAED.

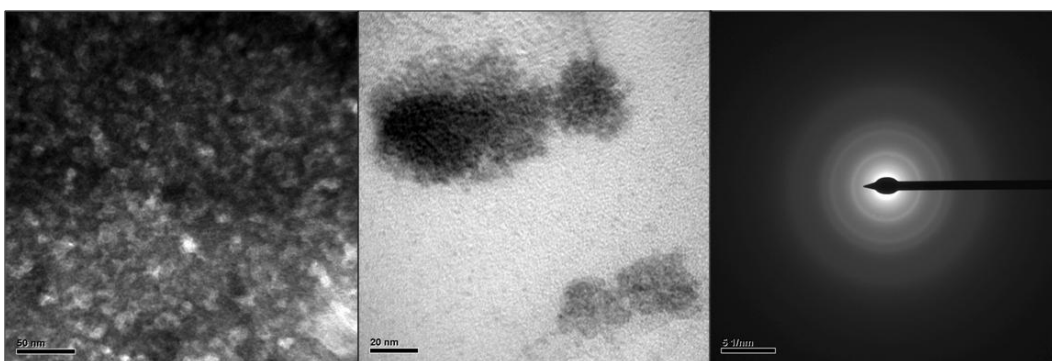


Figure 39: TEM micrographs and SAED of a PPV-CIS composite

Figure 39 shows the TEM data of 1/4 – PPV –CIS composite. Left hand side shows the dense network of the two components (dark areas are attributed to CIS). In the middle a

TEM micrograph of single particles is shown, particles are not monodisperse with diameters in the range of 10-30 nm. SAED data show diffuse reflection cones, indicative of a nano-structured material.

Table 8: SAED reflection list of a PPV-CIS blend

Ring	Radius / nm ⁻¹	1/Radius / nm	intensity / a.u.	plane index
1	3.218	0.320	100	(112)
2	5.139	0.195	67	(204), (220)
3	6.001	0.167	45	(116), (312)
4	8.858	0.113	31	(424)

Positions and intensities are summarized in Table 8. Comparison with reference data (PDF: 01-085-1575 27-159) shows good correlation of the obtained with literature data, plane distances in the reference file are 3.19, 1.96, 1.66 and 1.13 Å. Overall structural data show that a nanometer-sized composite is obtained following the method described.

6.3.2 PPV-CIS Solar Cells

Solar cells were prepared as described in the introduction. Polymer-CIS ratio and ageing time of the PPV-precursor were examined with respect to power conversion efficiency.

Testing of Different PPV-CIS Ratios

A continuous network of donor and acceptor phase is an essential prerequisite for a good bulk-heterojunction solar cell. Following the approach from [23], two different donor-acceptor ratios were tested, where PPV / CIS is 1 / 4 and 1 / 7 (mass ratios), respectively.

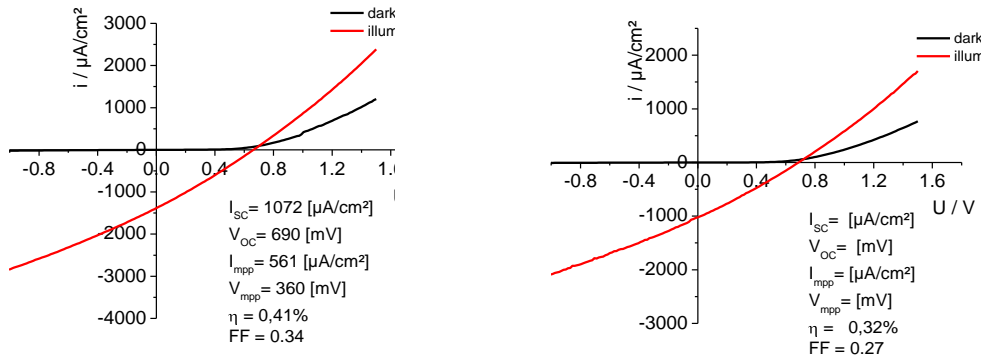


Figure 40: i-V curves of 1 / 4 (left hand) and 1 / 7 (right hand) PPV-CIS solar cells

Figure 40 shows i-V curves of two different devices, PPV-CIS ratio is 1 / 4 and 1 / 7. Solar cell parameters are quite comparable, PCE of the 1 / 4 device however is significantly higher than of the 1 / 7 device by virtue of the enhanced short circuit current and fill factor. It is assumed that deteriorated hole-transport in the 1 / 7 device accounts for the lower i_{sc} value, the great amount of CIS within the blend could reduce the available pathways for hole transport, reducing short circuit current as well as fill factor. This argument is in good correlation with the TEM-investigations, Figure 39 shows that a dense network structure is obtained already for the 1 / 4 PPV-CIS blend. For this reason, all further investigations were made using the 1 / 4 ratio.

Optical properties

Absorption properties and EQE of PPV-CIS solar cells were investigated. Data are displayed in Figure 41. Absorption spectra of the donor and the acceptor phase are shown by the dotted lines, the black line corresponds to the EQE spectrum of a 1/4 PPV-CIS solar cell. CuInS_2 is extending the absorption range beyond the bandgap of PPV (2.5 eV, corresponding to 496 nm [157]) beyond 800 nm. This is in concordance with the EQE-spectrum, which shows that a substantial contribution to the photocurrent is generated at wavelengths >500 nm, hence the inorganic phase does significantly contribute to photocurrent generation.

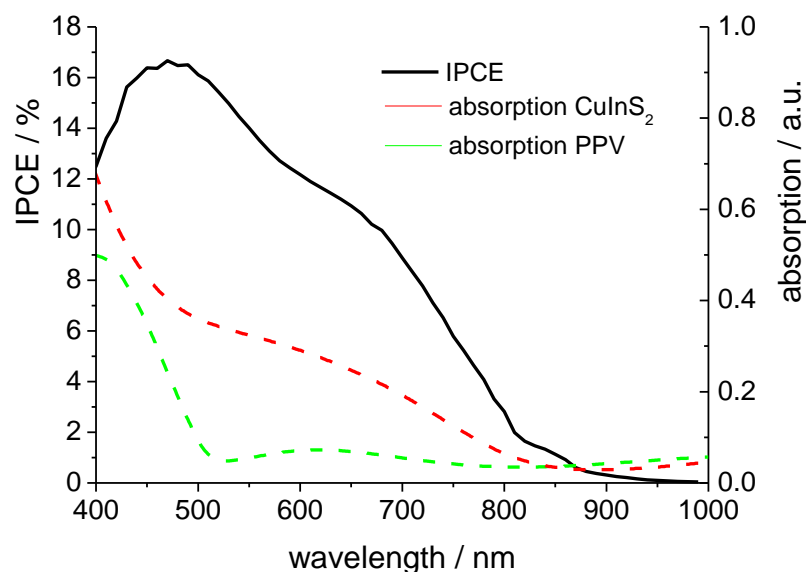


Figure 41: UV-VIS spectra of PPV-CIS layers and EQE spectrum of a 1/4 PPV CIS solar cell

PPV-CIS Solar Cells and Ageing of the PPV-Precursor

From previous work [23], where a Poly(*p*-xylene tetrahydrothiophenium chloride) precursor, which was synthesized at the institute (and was of considerable age) was used, it is concluded, that the quality of the PPV-precursor solution plays a considerable role during film formation and hence for the performance of the solar cell. In this experiment the PPV-precursor was stored at RT under exclusion of ambient light for one, two and three weeks and tested in PPV-CIS solar cells (cell-1, cell-2, cell-3). During this time, appearance of the precursor changed from colourless to yellow. For comparison, a reference cell was prepared using PPV-precursor without prior conditioning. All devices were prepared with a PPV / CIS ratio of 1 / 4.

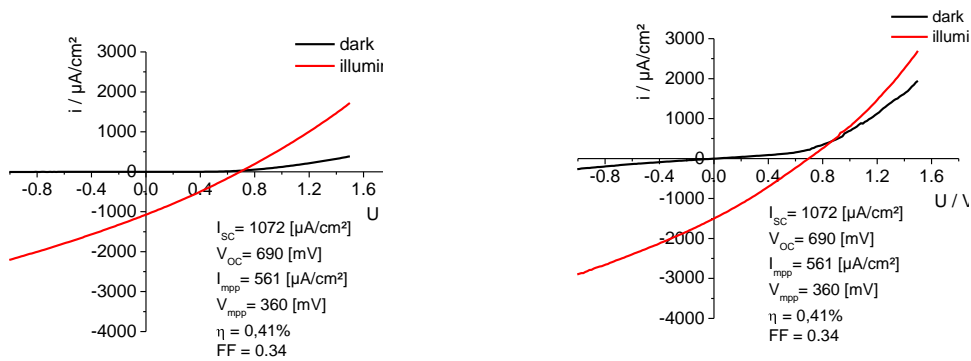


Figure 42: i-V curves of the reference cell and cell-1

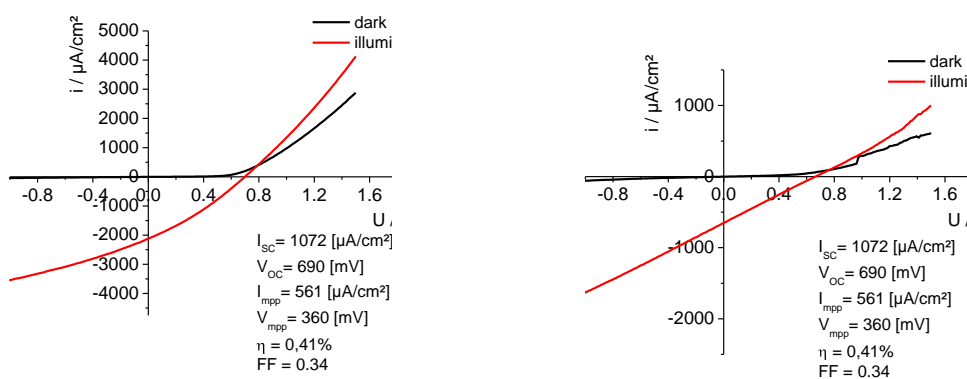


Figure 43: i-V curves of cell-2 and cell-3

Table 9: solar cell parameters

	η / %	V_{oc} / mV	i_{sc} / mA.cm ⁻²	V_{mpp} / mV	i_{mpp} / mA.cm ⁻²	FF
reference	0.34	690	1.072	360	0.561	0.27
cell-1	0.48	690	1.500	360	0.794	0.28
cell-2	0.75	705	2.120	390	1.15	0.30
cell-3	0.18	660	0.650	330	0.322	0.25

The preceding figures show the i-V curves of the different solar cells, efficiency parameters are summarized in Table 7. It can be readily seen, that ageing time of the PPV-precursor significantly affects solar cell action. Ageing of the PPV-precursor at ambient conditions results in increased solar cell performance, reaching its maximum value after

two weeks. The conjugated system is already formed to some extent during storage, as can be seen by the yellow colour. This is influencing precursor solubility and viscosity, which play a role in formation of the film and of the inorganic compound. When too much of the trans-vinylene bonds are formed, the precursor is subject to phase separation and parts of the macromolecule are not in vicinity of the acceptor, hence PCE is reduced when the precursor solution is allowed to pre-polymerize for three weeks.

6.4 Conclusion

The aim of this section was to demonstrate the feasibility of a recently proposed novel concept for hybrid solar cells [23]. Spray pyrolysis of solutions containing copper- and indium-salts as well as thiourea is a very well known process to generate films of CuInS_2 [219], this method was adapted (TU was replaced by TAA) for the in-situ generation of the acceptor phase in hybrid solar cells. Considering PPV-CIS blends, not only acceptor phase, but also the conjugated system of the donor is generated in-situ.

It was shown that photocurrent-generation not only occurs in the donor-, but also in the acceptor phase. 1/4 PPV-CIS ratio gave superior results compared to the 1/7 blend. However, ageing time of the PPV-precursor solution was identified to be the most influential parameter in this system.

7 P3EBT – CIS Composites and Solar Cells

7.1 Introduction

This section deals with the preparation of P3EBT – CuInS₂ (CIS) composites and their subsequent use as absorber layers in hybrid solar cells. Materials were obtained adapting the procedure described in chapter 5, CuInS₂ was obtained by the reaction of copper and indium metal salts with thiourea within the matrix of the conjugated polymer. Structural characterization was performed using XRD- and SEM-methods. Optical properties were determined by UV-VIS- and IPCE-spectroscopy, solar cell parameters were extracted from the i-V curves. Several aspects of P3EBT-CIS solar cells were investigated: Stoichiometry was examined by studying behaviour of bilayer heterojunction cells, consecutively exploration of bulk heterojunction type hybrid solar cells was performed by optimization of solvent systems, precursor materials and ratios, use of interlayers as well as detailed analysis of the decomposition reaction by XRD, TGA and IR-spectroscopy.

7.2 Proof of Principle – XRD analysis of an in-situ P3EBT – CIS composite

As an important prerequisite, the validity of the concept developed for binary sulfide semiconductors was verified for ternary semiconductors. A layer obtained by air-brushing of the precursor solution (composition is summarized in **Fehler! Verweisquelle konnte nicht gefunden werden.**) onto a Si wafer. The sample was annealed (RT $\xrightarrow{3 \text{ min}}$ 80°C $\xrightarrow{20 \text{ min}}$ 160°C $\xrightarrow{10 \text{ min}}$ 160°C, N₂-atmosphäre) and analyzed by XRD.

Table 10: Components and concentrations of precursor solution

	c(P3EBT) / mg.mL ⁻¹	c (CuI) / mg.mL ⁻¹	c (InCl ₃) / mg.mL ⁻¹	c (TAA) / mg.mL ⁻¹	P3EBT / CIS (wt. / wt.)	Cu / In / TAA (wt./wt./wt)
P3EBT-CIS	6	9.5	12.1	18.8	1 / 2	1 / 1.1 / 5

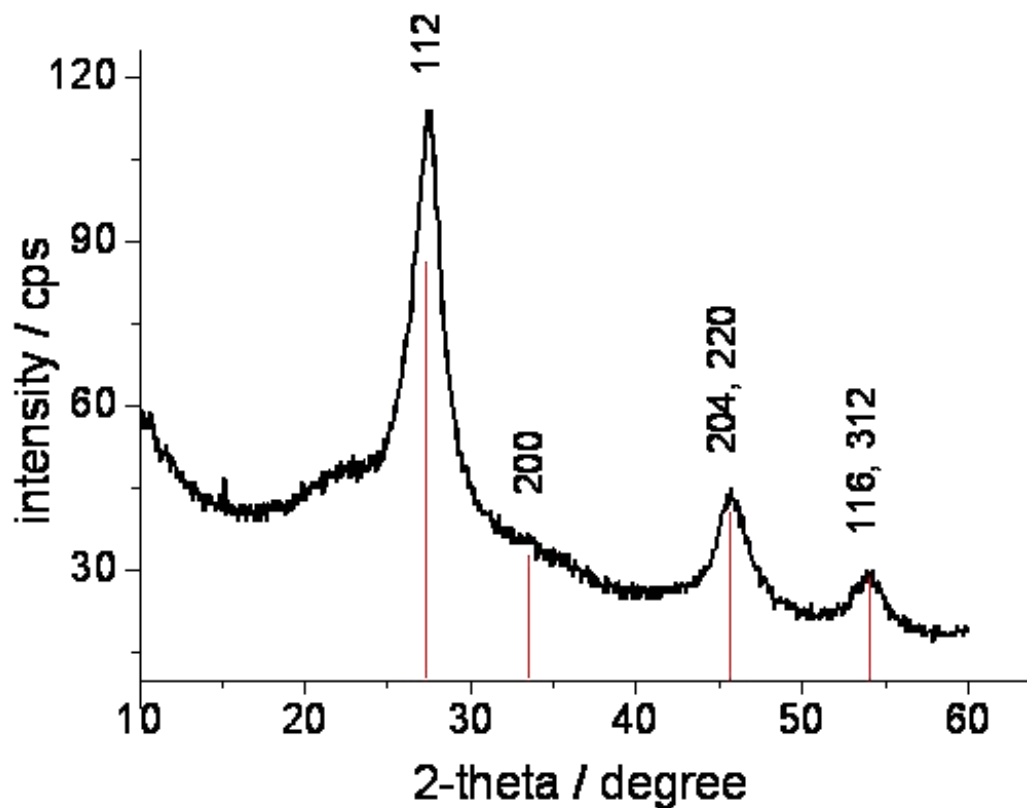


Figure 44: XRD data and peak positions of reference data

XRD-data of Figure 44 indicate the formation of the CuInS_2 phase; main reflections of the reference file (PDF 01-082-1702 27-159) are indicated by red lines. The experimental data correlate with the literature values, the three major peaks are present in the measurement. Almost no educt reflections (except for the very small feature at 15.15° 2-theta, which can be attributed to InCl_3) are detectable by XRD, indicating the formation of the inorganic semiconductor within the P3EBT-matrix. Analysis of the FWHM (1.85° 2-theta) of the (112)-reflection at 27.55° 2-theta the primary crystallite size is estimated to be 4.9 nm.

7.3 Bilayer Heterojunction Solar Cells and Optimization of CuInS_2 Stoichiometry

Within the bulk heterojunction active layer the CIS phase is acting as acceptor- as well as the electron transport phase. Depending on stoichiometry, p-type or n-type conduction can be observed in the material; stoichiometric CIS is considered as a p-type conductor,

generally Cu-rich material exhibits p-type conduction whereas In-rich material shows n-type conductivity [194] (compare section 3.3). Taking into account the volatility of group-three components [220],[221] and the elevated temperatures during the annealing procedure, this series was used to establish the optimum stoichiometry for polymer-CIS bilayer heterojunction solar cells. The results obtained in this experiment were used as a starting point for the stoichiometry optimization for bulk heterojunction devices.

7.3.1 Experimental

Precursor solutions with different compositions were prepared using acetonitrile as solvent and CuI, InCl₃ and TAA as CIS educts. Assuming complete and exclusive formation of CuInS₂, the CIS concentration of the precursor solution is 0.2 mM⁻¹. P3EBT was used as donor phase and was spin-coated from a pyridine solution (c(P3EBT) = 8 mg.mL⁻¹) at 1500 rpm / 1500 rpm.s⁻¹ / 20s. The polymer layer was annealed in an N₂-atmosphere for 15 minutes at temperature of 80°C. Subsequently the CIS precursor solution was spin-coated at 1000 rpm / 1000 rpm.s⁻¹ / 20s. Annealing of the acceptor phase was performed in a glove box (N₂-atmosphere) using the following temperature program: 120 °C $\xrightarrow{15\text{ min}}$ 120 °C $\xrightarrow{3\text{ min}}$ 160 °C $\xrightarrow{15\text{ min}}$ 160 °C. Finally, a 100 nm thick Al-cathode was evaporated using a BalTec MED020 evaporation unit.

Table 11: Composition of the precursor solutions

Cu / In / TAA	c (CuI) / mg.mL ⁻¹	c (InCl ₃) / mg.mL ⁻¹	c (TAA) / mg.mL ⁻¹
1 / 1.0 / 5	37.9	46.5	60.2
1 / 1.33 / 5	37.8	58.2	60.3
1 / 1.67 / 5	38.3	72.9	60.0
1 / 1.82 / 5	39.0	82.1	60.3
1 / 2.0 / 5	37.6	86.1	60.2
1 / 5.0 / 5	37.4	216.4	60.3

7.3.2 Results and discussion

Table 12 shows the corresponding PCE values, which are in the range of $1e^{-3}$ %.

Table 12: Solar cell efficiencies with different acceptor layer stoichiometries

Cu / In / TAA	1 / 1.0 / 5	1 / 1.33 / 5	1 / 1.67 / 5	1 / 1.82 / 5	1 / 2.0 / 5	1 / 5.0 / 5
η / %	$< 1e^{-3}$	$7.0 e^{-3}$	$8.2 e^{-2}$	$1.1 e^{-2}$	$9.5 e^{-3}$	$< 1e^{-3}$

This is attributed to the small interfacial area when adapting the bilayer heterojunction approach, in fact the situation was especially pronounced for precursor solutions with inferior wetting behaviour on the P3EBT polymer layer. This holds true especially for CIS-precursor solutions where a 1/1 pyridine-acetonitrile solvent system was used instead of pure pyridine, which is shown on the right hand side in Figure 45. The acceptor layer obtained from a purely acetonitrile-based solution (left hand) is compared with an acceptor layer obtained from a 1/1 acetonitrile-pyridine solution, while the CIS content was identical in both cases. Due to the unfavourable wetting properties of the acetonitrile-pyridine mixture, only a very small fraction of the polymer layer is covered with the inorganic phase, consequently only acetonitrile precursor solutions were tested with respect to solar cell activity.

The best device showed an efficiency of 0.082%, with a In to Cu ratio of 1.67. The i-V curve and device scheme are shown in Figure 46. The device shows a considerable short circuit current which, however, is contrasted by low fill factor and open circuit voltage values. The V_{oc} of 255 mV is unexpectedly low (the effective bandgap in the P3EBT-CIS system is 1.5 V), drastically reducing overall device performance, probably originating from bad adhesion of the donor and acceptor layers. In terms of stoichiometry optimization, the outcome of this experiment draws a definite picture; solar cells with an In to Cu ratio of 1.67 show a PCE higher by ca. 1 order of magnitude than PCE of devices with other stoichiometry.

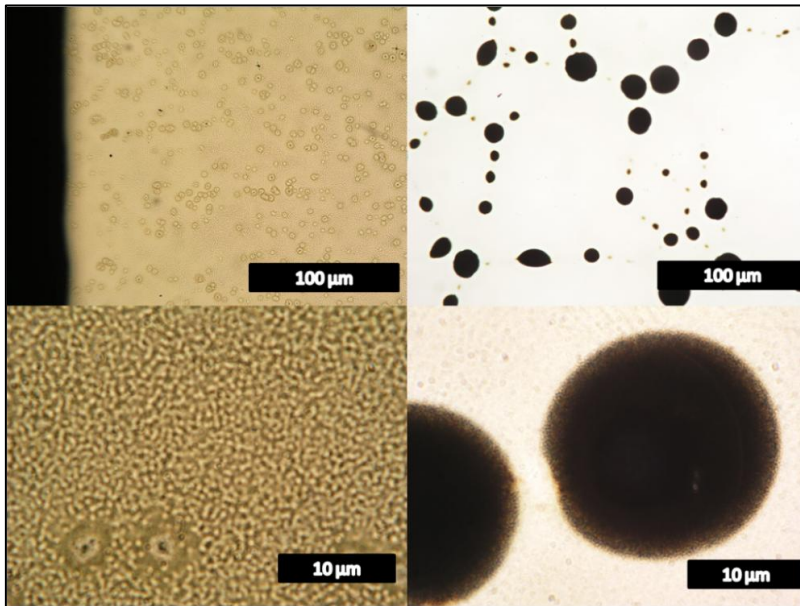


Figure 45: Optical micrographs of CIS-layers on top of a P3EBT-layer; Cu/In = 1/1.67 in all cases. Left hand: acetonitrile precursor solvent; right hand: acetonitrile-pyridine (1/1) mixture

It is assumed that a combined effect is accounting for this result: Changing the In to Cu ratio alters the surface energy and hence the wetting behavior of the precursor solution on the ITO substrate. When the sample is annealed, the indium content within the layer is reduced due to the high volatility of group three elements, correspondingly a higher amount than the stoichiometric proportion of In is needed for the formation of CuInS_2 .

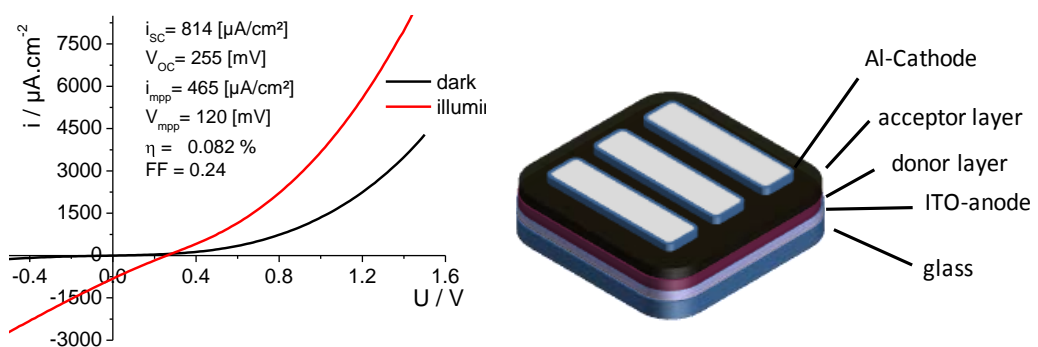


Figure 46: i-V curve and schematics of a P3EBT-CIS bilayer heterojunction solar cell ([In]/[Cu] = 1.67)

7.4 P3EBT-CIS Bulk Heterojunction Solar Cells from Different Copper- and Indium Precursors

7.4.1 Introduction

Considering organic solar cells, either the bilayer heterojunction or the bulk heterojunction approach is adapted for device fabrication. Polymer based devices very often have bulk-heterojunction configuration, which can be realized conveniently using wet-chemical deposition techniques. As a very important prerequisite for bulk heterojunction devices, a molecular-disperse solution containing every component of the film is necessary, as phase separation in the active layer is required to occur on the nm-scale. Practically, a clear solution containing all the components is required, for P3EBT-CIS BHJ-devices the precursor solution needs to contain the polymer, Cu-precursor, In-precursor and the sulfur source, whereas in the bilayer approach at least one component less (donor phase) is contained in the precursor solution. This was realized using combinations of the metal-acetates, -halogenides or -acetylacetonates together with thiourea as sulfur source in pyridine or pyridine acetonitrile mixtures.

7.4.2 CuI-InCl₃-TAA Precursor in Acetonitrile – Pyridine

The precursor system was adapted from the PPV-CIS system (chapter 6). As solubility of metal salts in pyridine is not sufficient to obtain concentrations of CuInS₂ ≥ 12 mg.mL, a 1/1 mixture of pyridine and acetonitrile was used. The metal salts were dissolved in acetonitrile, while the polymer was dissolved in pyridine, finally the two solutions were mixed. Table 13 shows the concentrations of the resulting solution.

Table 13: Composition of precursor solution

c (P3EBT) / mg.mL ⁻¹	c (CuI)		c (InCl ₃)		c (TAA)	
	/ mg.mL ⁻¹	/ mmol.mL ⁻¹	/ mg.mL ⁻¹	/ mmol.mL ⁻¹	/ mg.mL ⁻¹	/ mmol.mL ⁻¹
4	19.0	0.10	32.2	0.15	37.5	0.50

This solution was spin coated onto an ITO substrate at 1500 rpm/ 1500 rpm.s⁻¹ / 20s. After spin coating, annealing was performed in a glove box (120 °C $\xrightarrow{15\text{ min}}$ 120 °C $\xrightarrow{3\text{ min}}$

160 °C $\xrightarrow{15\text{ min}}$ 160 °C) and the Al-cathode (100 nm) was evaporated ion using a BalTec MED020 evaporation unit.

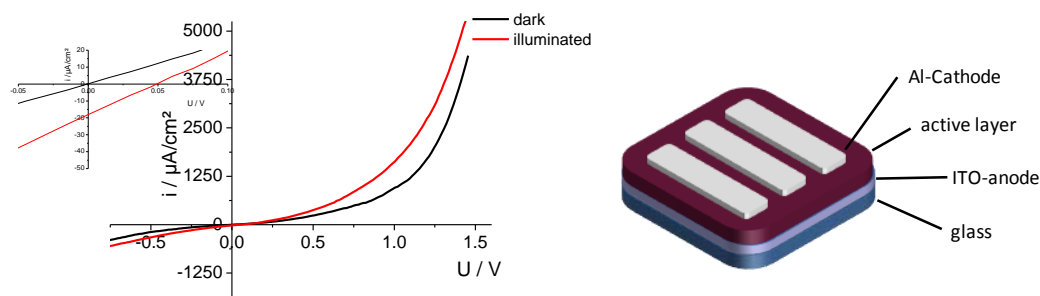


Figure 47: i-V curve and device scheme of a Cu-InCl₃-TAA based BHJ device

Figure 47 shows the i-V curve of typically obtained device. Virtually no photoeffect is observed, i_{sc} and V_{oc} values are $18 \mu\text{A}\cdot\text{cm}^{-2}$ and 45 mV, respectively. The In to Cu ratio was kept at 1.5, because a further increase of the InCl_3 resulted in non-stable solutions. The strong saturation of the solution, effectuating fast phase separation in the composite layer, together with the non-optimum In to Cu ratio are assumed to be responsible for the inferior device performance. Using a solvent mixture (pyridine-acetonitrile 1/1), an additional parameter in terms of the phase formation process during spin coating is added to the system, which is assumed to adversely affect the formation of the blend.

7.4.3 CuAc - In(Ac)₃ - TU - Pyridine Precursor

Copper acetate and Indium acetate were dissolved in pyridine. A clear solution is obtained, when thiourea is added and the solution is heated to $\approx 80 \text{ }^\circ\text{C}$ for about 5 minutes; finally P3EBT is added.

Table 14: Composition of precursor solution

c (P3EBT) / mg.mL ⁻¹	c (CuAc)		c (InAc ₃)		c (TU)	
	/ mg.mL ⁻¹	/ mmol.mL ⁻¹	/ mg.mL ⁻¹	/ mmol.mL ⁻¹	/ mg.mL ⁻¹	/ mmol.mL ⁻¹
8	12.2	0.10	48.6	0.17	76.1	1.00

Processing parameters were kept constant (compare section 7.4.2) and i-V characteristics were measured in N₂-atmosphere.

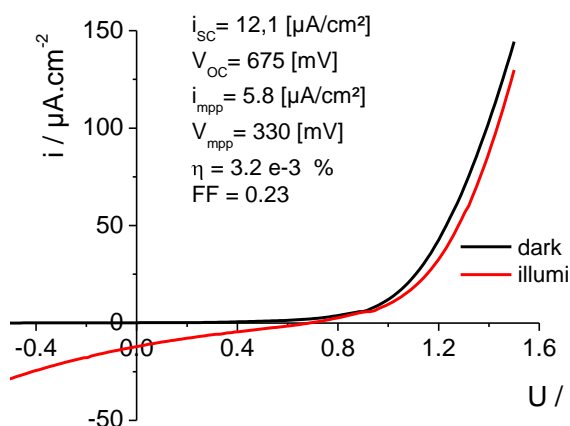


Figure 48: i-V curve of CuAc-In(Ac)₃-TU based BHJ solar cell

The i-V curve of the device with the highest measured V_{OC} -value is shown in Figure 48. While good rectification behavior and open circuit voltage has been observed, fill factor and especially photocurrent values seek improvement for prospective applications. As in section 7.4.2, the results reflect the critical role of the precursor solution with respect to solar cell performance; the obtained V_{OC} -value of 0.675 V demonstrates the potential of the method presented to produce efficient hybrid solar cells.

7.4.4 Copper(I)chloride- In(acac)₃ - TU - Pyridine Precursor Solutions

Dissolution of the Indium compound is most challenging for in-situ formation of the acceptor phase. Stoichiometric considerations necessitate bigger amounts of the In-component, while the larger molar mass (caused by three counter ions) additionally increases the proportion of the indium species within the precursor solution. While pyridine is a solvent with medium polarity ($\epsilon_r = 13.26$, $\mu = 2.2 \text{ D}$) its ability to dissolve inorganic metal components is limited and primarily based on its behavior as a complexing ligand [222]. This was the motivation to use an indium species with an organic ligand. In fact solutions containing indium acetylacetonate (In(acac)₃) showed very good stability and could be obtained as a clear suspension before the addition of thiourea. Several copper salts (CuAc, CuCl, CuI) were tested in this experiment, device-like behavior

however was only obtained for the copper(I)-chloride indium-acetylacetonate combination. Table 15 shows the composition of the precursor solution.

Table 15: Composition of the precursor solution

c (P3EBT) / mg.mL ⁻¹	c (CuCl)		c (In(acac) ₃)		c (TU)	
	/ mg.mL ⁻¹	/ mmol.mL ⁻¹	/ mg.mL ⁻¹	/ mmol.mL ⁻¹	/ mg.mL ⁻¹	/ mmol.mL ⁻¹
8	9.9	0.10	74.9	0.18	76.1	1.00

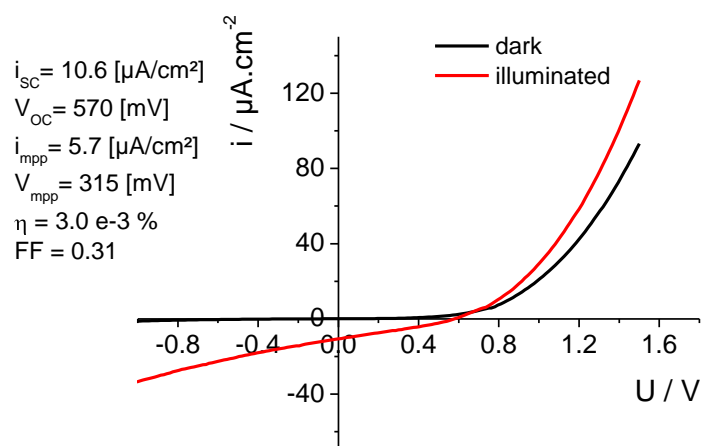


Figure 49: i-V curve of a CuCl - In(acac)₃ – TU based BHJ solar cell

The i-V curve of a typical device is depicted in Figure 49. Due to the low short circuit current solar cell performance does not meet the expectations, whereas V_{oc} of 570 mV is acceptable.

7.4.5 CuAc – InCl₃ – TU – Pyridine Precursor

Two counter ions with high volatility were chosen in order to enhance the formation of CuInS₂. Table 16 shows the components of the precursor solution, again pyridine was used as solvent.

Table 16: Composition of the precursor solution

c (P3EBT) / mg.mL ⁻¹	c (CuAc)		c (InCl ₃)		c (TU)	
	/ mg.mL ⁻¹	/ mmol.mL ⁻¹	/ mg.mL ⁻¹	/ mmol.mL ⁻¹	/ mg.mL ⁻¹	/ mmol.mL ⁻¹
8	12.2	0.10	36.9	0.17	76.1	1.00

Devices were prepared as described in the proceeding sections by spin coating, annealing was performed in a glovebox as described in section 7.3.1.

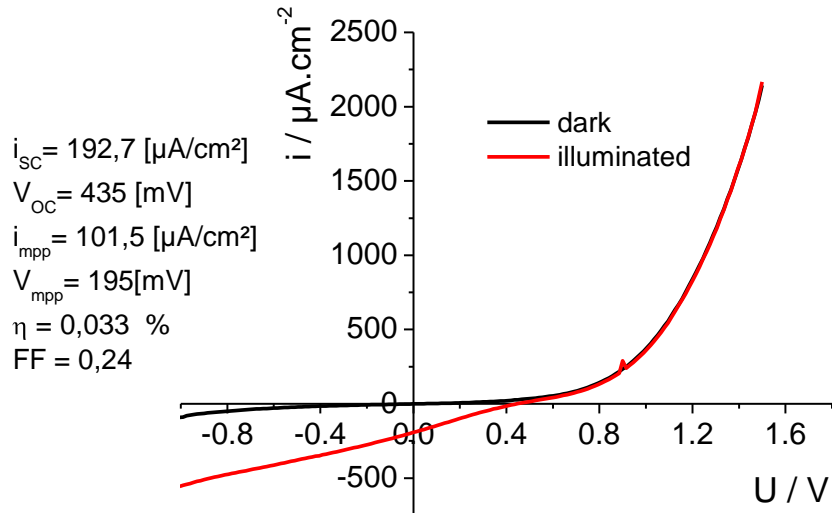


Figure 50: i-V curve of a Cu(Ac) - InCl₃ - TU based BHJ solar cell

Solar cells obtained from this precursor solution still leave plenty of opportunity for improvement, however, compared to the previous efforts to obtain bulk-heterojunction devices, efficiency improves by one order. V_{OC} of 435 mV is not as high as e.g. in the CuAc-In(Ac)₃-system, but due to the enhanced short circuit current device performance improves appreciably.

7.4.6 Conclusion from Precursor Experiments

This section demonstrated the utilization of different precursor systems for in-situ generated P3EBT-CuInS₂ blends. Solar cell parameters are summarized in Table 17.

Table 17: Summarized solar cell parameters for different precursor systems

	η / %	V_{OC} / mV	i_{SC} / $\mu\text{A}\cdot\text{cm}^{-2}$	FF	V_{mpp} / mV	i_{mpp} / $\mu\text{A}\cdot\text{cm}^{-2}$
CuAc - In(Ac) ₃ - TU	3.20E-03	675	12.1	0.23	330	5.8
CuCl - In(acac) ₃ - TU	3.00E-03	570	10.6	0.31	315	5.7
CuAc - InCl ₃ - TU	3.30E-02	435	192.7	0.24	195	101.5

PCE and i_{sc} values differ by more than one order of magnitude, open circuit voltage varies by 240 mV. From the precursor solutions used, the CuAc-InCl₃-TU combination explicitly shows the best efficiency result as the short circuit current is higher by one order of magnitude. Clearly, high PCE is attainable only by increasing i_{sc} and FF values, given that photovoltages are in a range similar to fullerene based devices. The different behavior of the various precursor solutions is originating from the interactions during the film formation process on one hand, on the other hand chemical reactivity during the annealing process is strongly depending on the precursor materials. During the spin-coating process the components of the solution phase-separate as the film is formed, depending on their chemical compatibility and the time for the formation of the layer. Such behavior can cause disadvantageous morphology [90], in fact it has been shown for fullerene solar cells, that good performance is attained only, when the solubility of the donor and acceptor species are more or less equal [91]. Apparently this aspect is quite challenging for the actual system, four components need to be dissolved in the precursor solution. It is believed that this is one of the reasons for the explicitly bad characteristics of the CuI-InCl₃-TAA system, where, due to solubility reasons, a pyridine-acetonitrile solvent was used: During spin coating, acetonitrile has a stronger tendency towards evaporation than pyridine, hence the components with good solubility in acetonitrile will precipitate at an early stage of film formation. Contrary to polymer-fullerene solar cells, where several reports indicate additive-induced morphology improvement [92],[223],[224], additional solvent components have negative impact on film formation in the multi-component system under investigation.

7.5 Investigation of Donor – Acceptor ratio and Concentration of the Precursor

7.5.1 Introduction

Creation of continuous pathways of donor and acceptor phase to the respective electrode is a necessary requirement for bulk-heterojunction solar cells. In this chapter, P3EBT-CIS solar cells were analyzed with respect to the optimum donor- acceptor composition and

concentration. Optimum ratio of the components is strongly depending on the materials, PCBM based devices containing PPV-type polymers have a donor to acceptor ratio of 1/4 (wt./wt.) [225] while devices with a P3HT donor phase show of a ratio of 1/1 (wt./wt.) or even lower PCBM content [145],[226]. In the case of polythiophenes it has been shown, that density and volume of the polymer side chains have a significant effect on the mobility [227], in composites with a fullerene species polymer side chain density is influencing the formation of the bicontinuous network [226].

Considering hybrid devices, naturally greater diversity with respect to optimum donor-acceptor ratio is encountered as the number of possible material combinations is large and only few acceptor phases were investigated in combination with different polymers. Such results are actually meaningful only, if the acceptor phase was synthesized using an identical procedure (different particle shapes, sizes and surface ligands). For CdSe, optimum acceptor content is reported to be ≈ 85 %wt. for a CdSe-tetrapod-MEH-PPV-combination [228], the same fraction is communicated for a CdSe-nanorod-APFO combination [229]. A CdSe-nanorod-P3HT composite contains ≈ 90 %wt. of the inorganic phase [230], whereas for a hyperbranched CdSe-P3HT active layer even 95 %wt. CdSe-content are reported [231]. Semiconductor oxide – polymer combinations contain lower amounts of the acceptor phase, ZnO-polymer composites show optimum PCE containing ≈ 50 %wt. ZnO (in-situ generation of ZnO, P3HT-donor [232], while ZnO-content is 67 %wt. for a combination of pre-synthesized ZnO in combination with MEH-PPV [233]). The optimum amount of TiO₂ in TiO₂-nanodot-P3HT solar cells is reported to be 60 %wt., while a P3HT-TiO₂-nanorod combination showed maximum PCE of 0.8% with 53 %wt. TiO₂ [234]. Considering polymer-chalcopyrite-type semiconductor systems, CuInSe₂-P3HT devices with a maximum efficiency of 0.15% contain 90 %wt. acceptor phase [195].

7.5.2 P3EBT-CIS Solar Cells with Different Donor and Acceptor concentrations

Solutions with different amounts of CIS-precursor and a different donor-acceptor ratio were tested in the active layer of P3EBT-CIS solar cells. CuAc, InCl₃, thiourea and P3EBT dissolved in pyridine acted as active layer precursor, preparation of the precursor is outlined in section 7.4.5. Mixtures with a CIS-precursor content of 24 mg.mL⁻¹ and 18

mg.mL⁻¹ were combined with polymer concentrations of 6, 8 and 10 mg.mL⁻¹. Device preparation was performed by spin coating with constant parameters (1000 rpm / 1000 rpm.s⁻¹ / 30s), annealing of the devices was carried out in a glove box (N₂-atmosphere, 120 °C $\xrightarrow{15\text{ min}}$ 120 °C $\xrightarrow{3\text{ min}}$ 160 °C $\xrightarrow{15\text{ min}}$ 160 °C). Finally, a 100 nm thick Al electrode was evaporated using a Baltec MED-020 evaporation unit. Current voltage curves were measured using a Keithley 2400 source measurement unit. Table 18 summarizes the results, the individual i-V curves are attached in appendix 10.2):

Table 18: Solar cell parameters from different donor acceptor concentrations

CIS-P3EBT / mg.mL ⁻¹	η / %	V _{OC} / mV	i _{SC} / μA.cm ⁻²	FF	V _{mpp} / mV	i _{mpp} / μA.cm ⁻²
18-6	0.046	390	254	0.25	180	154
18-8	0.027	375	129	0.26	195	64
18-10	0.020	345	137	0.26	180	68
24-6	0.032	300	250	0.26	165	117
24-8	0.022	255	200	0.27	135	102
24-10	0.013	285	51	0.26	150	51

Optimum performance was reached with donor to acceptor ratio of 1 / 3 (wt./wt.) in the active layer and a CIS-precursor content of 18 mg.mL⁻¹ (18-6 series, corresponding to a mass fraction of 75%), followed by to the 24-6 series with a 1 / 4 (wt./wt) ratio (80 %wt. of acceptor) of the active layer components. Interestingly, the 24-8 series, containing the same relative amounts as the 18-6 series, reached only half of the PCE of 18-6 series, primarily due to low open circuit voltages (255 mV compared to 390 mV). Increasing polymer content reduces both, V_{OC}- and i_{SC}-values, which can be attributed to insufficient network formation. The fact that solutions containing 24mg.mL⁻¹ of CIS precursor generally perform inferior compared to the lower concentrated samples is assigned to the high concentration of educts, during spin coating precipitation of the components occurs rapidly, and hence phase separation in the active blend is difficult to control.

7.6 Analysis of the Annealing Process and Optimization of the Heating Rate

7.6.1 Introduction

Thermal annealing of bulk-heterojunction solar cells is frequently used to tune the morphology of the active layer [103],[102], alternatively solvent additives are used to modify the phase separation of the components [94]. Considering the in-situ P3EBT-CIS system, morphology tuning is a prerequisite for the annealing procedure, where the decomposition of the sulfur source (i.e. thiourea) and the formation of the inorganic phase are the principal processes. In this section the temperature dependent formation of CuInS_2 is monitored by XRD, FT-IR, TGA-MS and mass spectrometry, consequently solar cell action was investigated. The effect of the annealing step on P3EBT was studied using FT-IR.

7.6.2 Online XRD-Monitoring of CuInS_2 Formation

Samples were prepared by air-brushing a solution containing the active layer precursor solution (CuAc , $\text{In}(\text{Ac})_3$, thiourea and P3EBT dissolved in pyridine (compare section 7.4.5) onto a silicon waver. XRD-data were recorded between 15 and 45° 2-theta using a Bruker D8 Discover diffractometer equipped with an Anton Paar Domed Hot Stage Unit. Following temperature program was used for the measurement: RT $\xrightarrow{20^\circ\text{C}/\text{min}}$ 80 °C $\xrightarrow{5^\circ\text{C}/\text{min}}$ 180 °C $\xrightarrow{20^\circ\text{C}/\text{min}}$ 450 °C).

The results are shown in Figure 51: After preparation of the sample, a series of four peaks (indicated by black arrows) at 19.70, 22.84, 25.32 and 27.62 degrees 2-theta appears, which can be attributed to complexes of the metals with thiourea and pyridine. In the course of the annealing process, the intensity of the initial reflections decreases rapidly, at a temperature of 100 °C the initially observed pattern has practically vanished.

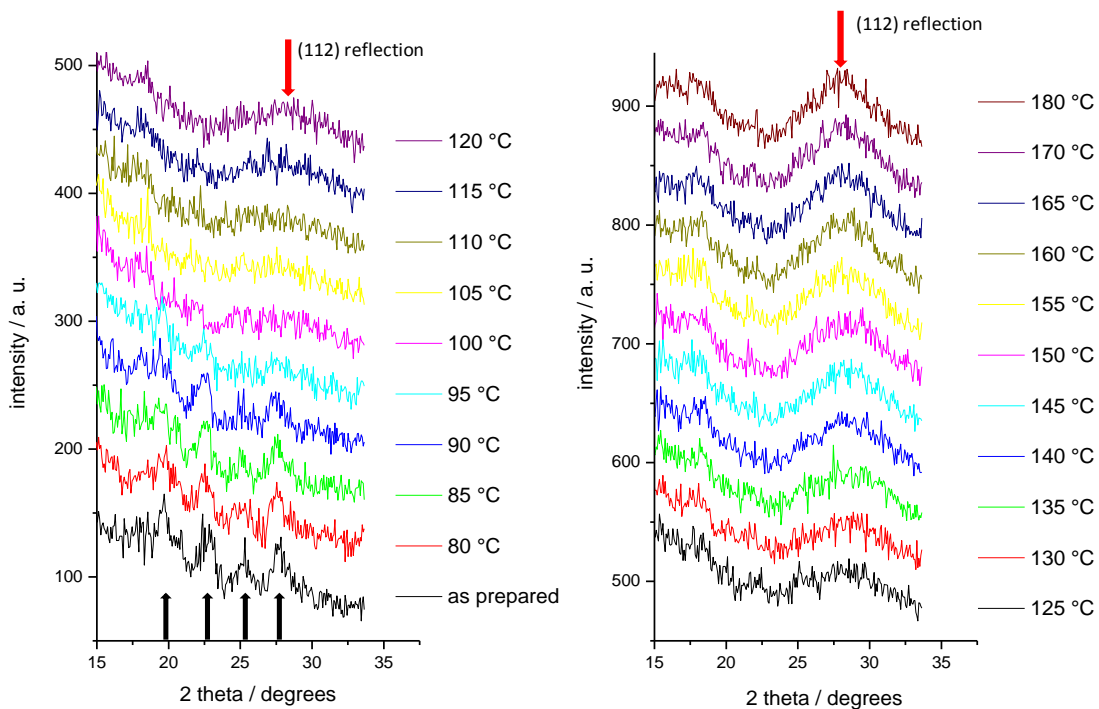


Figure 51: Temperature dependent evolution of the (112) reflection

Starting at 120 °C, the evolution of a broad peak at 28 degrees 2-theta is observed (indicated by a red arrow), which is attributed to the (112)-reflection of CuInS_2 (reference value: 27.90 degrees 2-theta, from PDF 01-085-1575 27-159). This serves as an important information for future annealing strategies, as a minimum temperature of 120 °C is necessary for the formation of the acceptor phase.

7.6.3 Investigation of the Decomposition Process by TGA-MS

In this experiment, the materials comprising the active layer were analyzed by thermogravimetry and mass spectroscopy. Samples were prepared by drop coating of a ZCIS (compare section 7.7.2) active layer precursor solution (CuAc , InCl_3 , ZnAc_2 , TU (1/2/0.1/10) and P3EBT in pyridine, $c(\text{ZCIS}) = 18 \text{ mg.mL}^{-1}$, $c(\text{P3EBT}) = 6 \text{ mg.mL}^{-1}$, compare) onto soda-lime glass slides.

Table 19: Composition and relative amounts of the precursor solution

	CuAc	InCl ₃	ZnAc ₂	TU	P3EBT	total
c / mg.mL ⁻¹	9.1	32.84	1.36	56.5	6	105.8
c(rel.) / %wt.	8.6	31.0	1.3	53.4	5.7	100.0

After drying under vacuum for two hours to remove the pyridine, the layers were scraped off and annealed using two different heating rates (final temperature $T_f = 160$ or 200 °C, heating rate = 5 or 20 °C/min, compare

Figure 52). Thermogravimetric- and TIC-data are shown for samples with $T_f = 160$ °C, detailed analysis of the mass spectra is demonstrated for a sample heated to $T_f = 200$ °C using heating program 1 (Figure 52). Thermogravimetric data for $T_f = 180$ °C, thermodata of thiourea and reference mass spectra are attached in appendix 10.4.

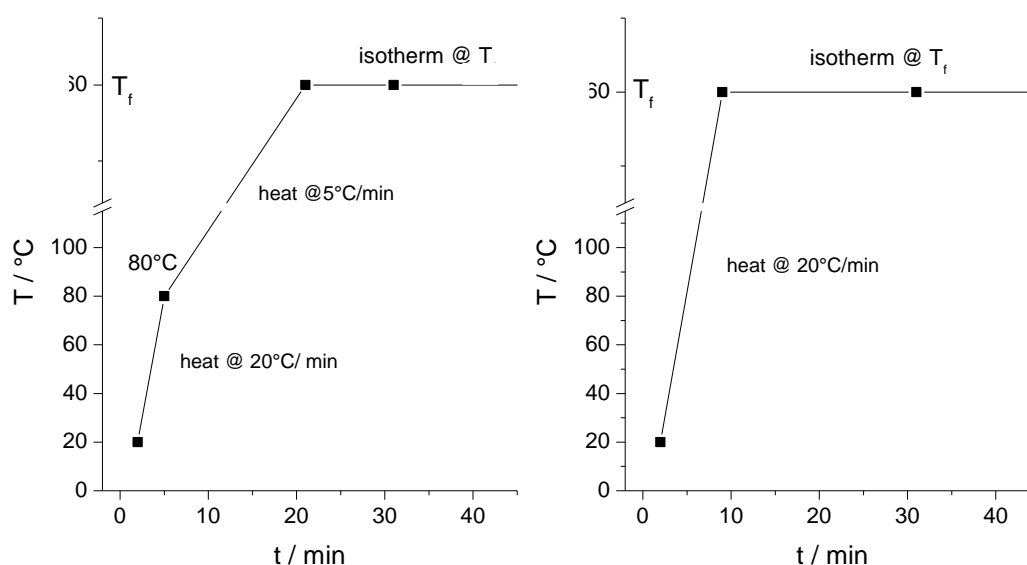


Figure 52: Temperature programs used in TGA experiments; left side: after a temperature of 80 °C is reached, annealing proceeds @ 5 °C/minute (program 1); right side: samples are annealed using a heating rate of 20 °C / minute (program 2)

Thermogravimetric- and total ion current-data (TIC) of the samples heated to a final temperature T_f of 160 °C are shown in Figure 53 (data for samples with $T_f = 180$ or 200 °C can be found in appendix 10.4). Qualitative analysis of the TG-data reveals evident differences in sample weight. When the samples are annealed with different heating

programs, faster heating results in more pronounced mass loss. Consequently, the total ion current of the sample heated at 20 °C/min reaches its maximum shortly after the final temperature of 160 °C, followed by a fast decay in the generation of pyrolysis products, while at a heating rate of 5 °C/min a fairly constant release of reaction products is observed. A very significant feature is the relative sample weight at the end of the heating routine, which is 71.7% and 65.1% of the initial weight for heating using program 1 / program 2, respectively. Comparison with Table 19 shows that the thiourea content of the precursor solution is 53.4%, quantitative reaction / thermolysis of TU corresponds to a final mass 46.6% of the initial mass (assuming zero pyridine content in the samples), indicating that a substantial amount of the sulfur source is still present within the sample (see also section 7.6.4).

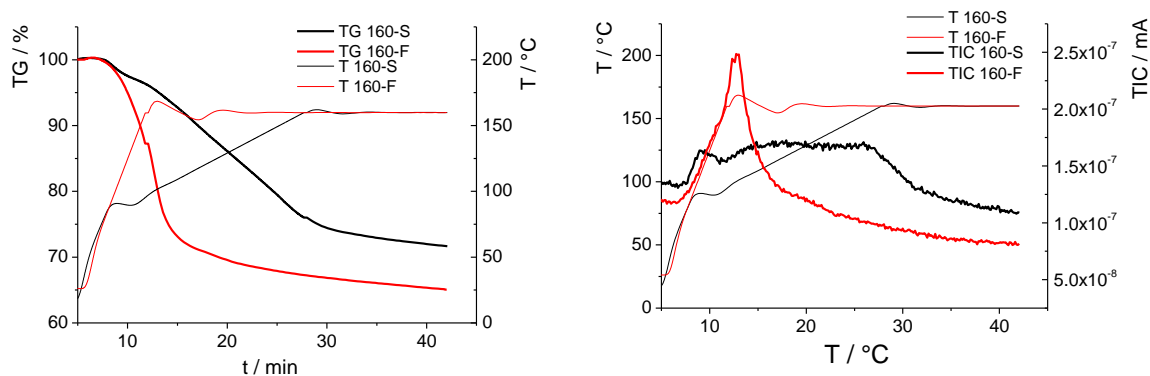


Figure 53: TG and TIC data of samples heated to 160 °C at different rates; black lines: heating program 1; red lines: heating program 2 (compare Figure 52)

Chemical information from the pyrolysis products was obtained by mass spectrometry. The sample was heated to a final temperature of 200 °C using heating program 1 (Figure 52). Figure 54 illustrates the temperature-dependent generation of the various pyrolysis products. The appearance of the mass spectra is strongly dominated by fragments from pyridine (while other decomposition products are difficult to identify), together with a slowly decreasing peak at $m/z = 32$ (presumably oxygen), most of the peaks can be traced back to pyridine fragments ($m/z = 78, 79$ (molecule-ion) 80 ; $m/z = 49-52$) until 100 °C. Starting at 110 °C, two small peaks at $m/z = 43$ and 45 arise, which can be attributed to decomposition products of thiourea or the acetate-ion, which both have fragments of this

mass. All the features so far decrease at a temperature of 170 °C, where a fragment at $m/z = 76$, corresponding to the thiourea molecule-ion appears, with another thiourea fragment appearing at $m/z = 43$ and increasing signal in sulfur containing compounds at $m/z = 32, 33, 34$.

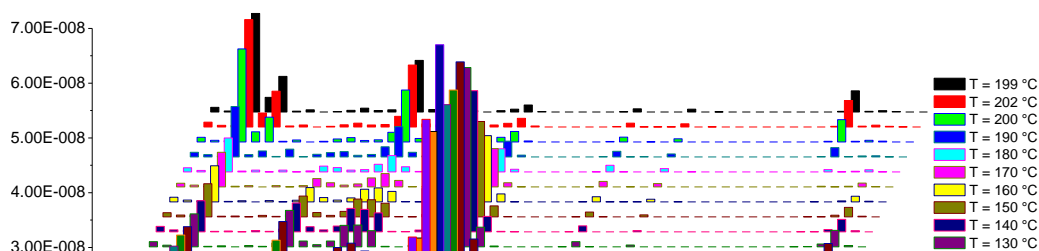


Figure 54: Mass spectra of an active-layer sample during heating from RT to 200 °C using heating routine 1 (compare Figure 52), $T_f = 200$ °C

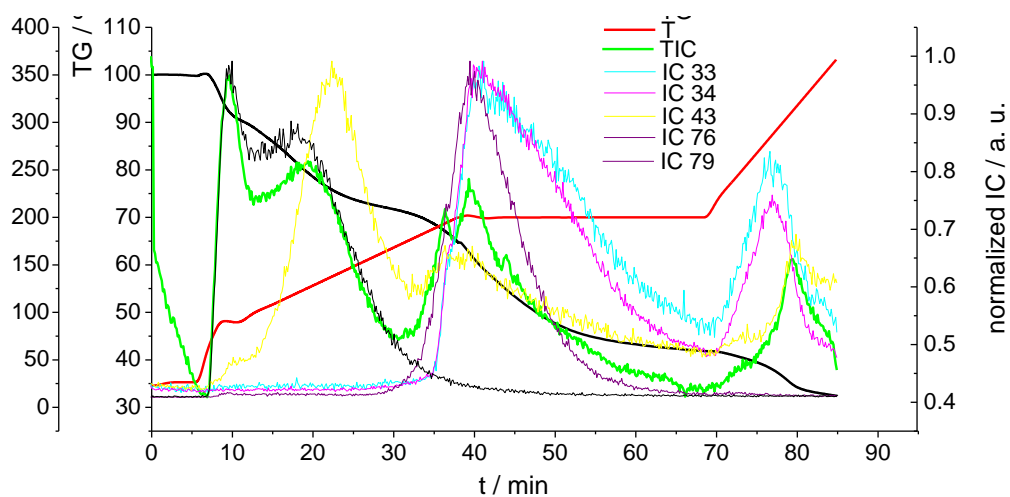


Figure 55: Selected normalized ion currents during the annealing reaction of an active layer sample (heating program 1, followed by an additional heating step from 200 to 350 °C)

Figure 55 shows the corresponding normalized ion currents. Until a temperature of 150 °C the appearance of the TIC is very similar to that of the pyridine-IC (IC-79), at higher

temperatures there is a strong resemblance of the TIC-signal with that of HS and H₂S (ICs 33 and 34). Comparison of the 34-ion current (fragments from acetate and thiourea) with the IC of thiourea (IC-76) suggests that the first peak is due to acetates leaving the sample, while the second peak most likely stems from the decomposition of thiourea. Further pyrolysis of the sample takes place at temperatures above 200 °C (note the different slope of the TG-signal), a temperature range considered to be incompatible for processing of P3EBT (compare section 7.6.5).

7.6.4 Analysis of the Annealing Process using Mass Spectrometry

In the preceding section, products from the thermal curing were analyzed by a quadrupole mass spectrometer, which was attached to the TGA-setup, only allowing the identification of the very basic products of the reaction. For this reason the decomposition reaction was analyzed using a Waters Micromass GCT Premier spectrometer (EI ionisation, TOF mass analyzer): Precursor solution (P3EBT / CIS = 1 / 4; Cu / In / TU = 1 / 1.7 / 10, compare section 7.4.5) was drop coated onto a soda-lime glass slide, the sample was dried in vacuum atmosphere for two hours. Afterwards a small amount of the layer was scraped off and placed directly into the capillary of the mass spectrometer which was heated in the sample chamber of the mass spectrometer. Contrary to results from the TGA-MS measurement, fragments with $m/z > 100$ were detected, a distinct peak at $m/z = 126$ could be identified as one of the major products in this region of the spectrum (Figure 56). Analysis of the fragmentation pattern and accurate mass determination of the substance allowed the identification of the compound, the peak is attributed to 2,4,6-Triamino-1,3,5-triazine (Melamine). The compound apparently is not contained in the precursor solution. The following scheme illustrates the formation of the compound, as is proposed in [235]. Cyanamide, CS₂ and ammonia are formed during the pyrolysis of thiourea, upon the trimerization of cyanamide melamine is obtained. Its presence in thin film solar cells from thiourea-containing precursors is questioned in [219]; more mechanistic detail is given in [236],[237].

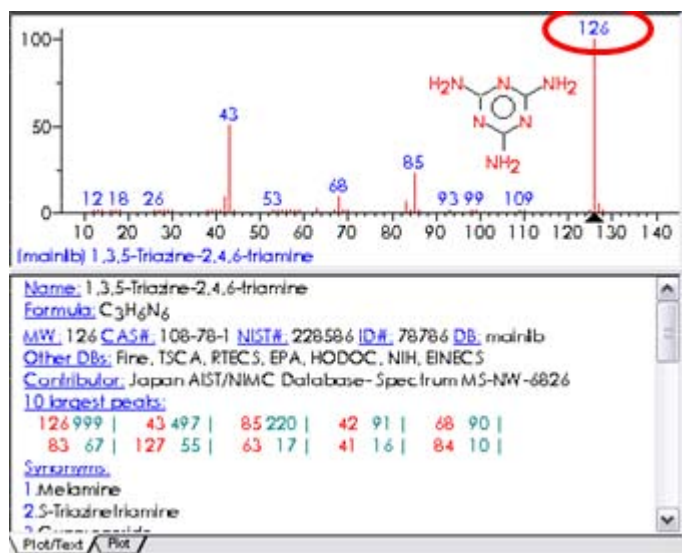


Figure 56: Screenshot from the analysis of the peak at $m/z = 126$

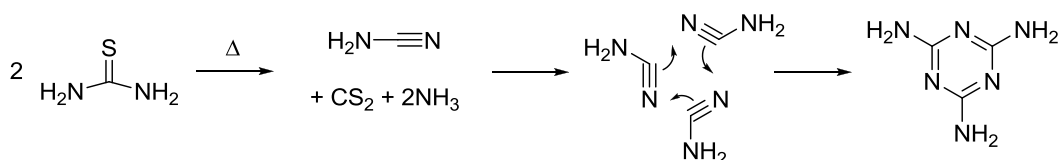


Figure 57: Schematic illustration of the formation of melamine from thiourea

Following the ion current (IC) at $m/z = 126$, melamine formation as a function of time (and temperature) can be monitored. Top image of Figure 58 shows the onset of melamine formation after 30 minutes at a temperature of ca. 125 °C (temperature of sample chamber). Melamine IC consecutively increases when the sample is kept at the temperature, maximum release of the compound occurs at a temperature of 180° C. As the melting point of melamine is 350 °C (decomposition), it cannot be removed from the blend without decomposition of the polymer. Though not present in large quantities (detection by FT-IR was not possible) it is assumed that exciton dissociation and charge transport will be negatively influenced by the presence of the compound, adversely impacting on photovoltaic performance.

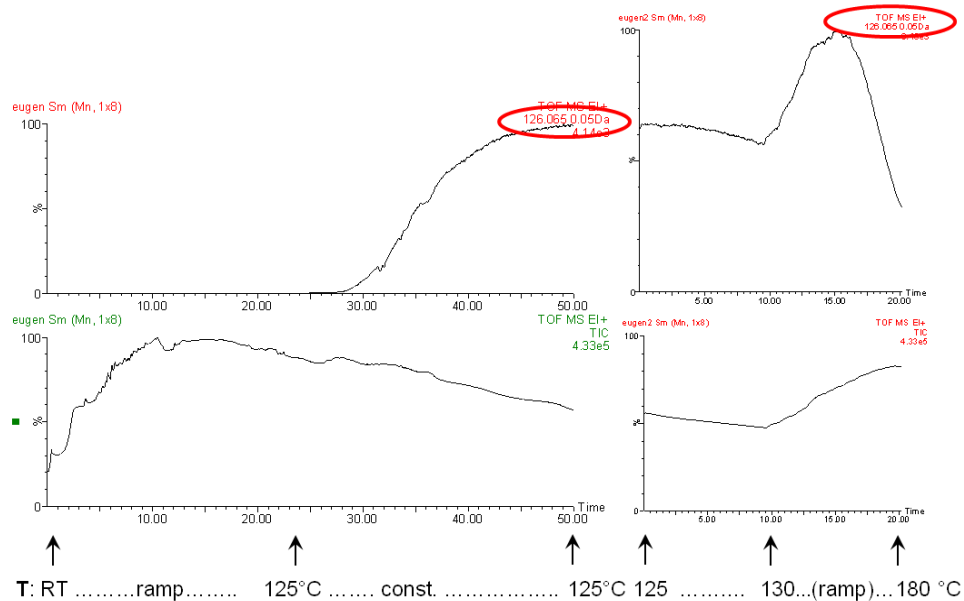


Figure 58: Melamine (top) and total ion current (bottom) during the course of the measurement

7.6.5 Thermal Stability of P3EBT

In order to investigate the thermal stability of the donor material, P3EBT films were analyzed by FT-IR. Samples were prepared by spin coating of P3EBT onto CaF₂ substrates, annealing was performed at different temperatures ($T_f = 180, 160, 200, 230$ and 250 °C, respectively; heating program 1 (Figure 52)) using a tube furnace (vacuum atmosphere). Overall annealing for all samples was 47 minutes in all experiments. After cooling to RT (no specific cooling program), the samples were probed by FT-IR.

Figure 59 shows the corresponding spectra. Although sample preparation was identical, transmission values vary evidently, probably due to different layer thicknesses. For this reason the area of two spectral ranges was compared, A1 corresponds to $3020-2750$ cm⁻¹ (aliphatic C-H stretch), A2 corresponds to $1760-1575$ cm⁻¹ (ester-carbonyl). From the premise that C-H bonds are thermally more stable than the ester functionality, the relative area of the peaks should return a qualitative information on the thermal stability of the compound. Analysis involving peaks originating from vibrations of the thiophene ring (e. g. symmetric / asymmetric ring stretch at 1447 and 1510 cm⁻¹, respectively) was intricate,

as their intensity strongly decreases, when $T_f > 180$ °C. Integrated peak areas are listed in Table 20. Whereas the relative area is comparable between the RT- and the 180 °C-sample (1.2 vs. 1.3), significant deviation (≥ 1.7) from the initial value of 1.3 is observed at higher curing temperatures, corresponding to the degradation of the carbonyl group. It should be noted, that from the data obtained, hydro-acyloxy elimination of the ethyl ester cannot be asserted, in this case the carbonyl function would be conserved (conversion of the ester- into acid functionality) and a shift its position, additionally the carboxy-OH – stretch vibration should appear, which could not be verified. However, it is shown, that annealing temperatures higher than 180 °C are detrimental to the structural integrity of the polymer and hence to solar cell performance. This temperature is in the same range as was found for poly-3-alkoxy-thiophenes [238], but considerably lower than data on P3HT (decomposition at $T > 400$ °C) [239].

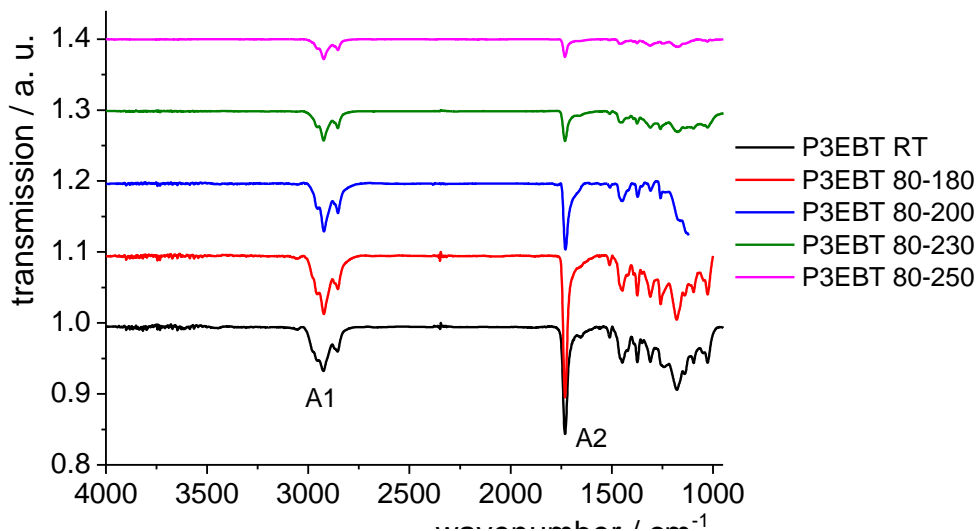


Figure 59: FT-IR spectra of P3EBT-layers annealed at various temperatures T_f

Table 20: Peak area of P3EBT layer at various temperatures

	A1 / area / a.u. 3020-2750 cm^{-1}	A2 /area / a.u. 1760-1575 cm^{-1}	A1 / A2
P3EBT-RT	-591.9	-461.9	1.3
P3EBT-80-180	-665.4	-556.6	1.2
P3EBT-80-200	-451.3	-258.7	1.7
P3EBT-80-230	-320.6	-162.4	2.0
P3EBT-80-250	-199.4	-79.0	2.5

7.6.6 Hybrid Solar Cells Using Different Annealing Procedures

In order to examine the effect of the thermal treatment on the photovoltaic parameters, P3EBT-CuInS₂ solar cells were investigated using different annealing procedures, which are summarized in Table 21. Precursor solutions were prepared as described in section 7.4.5 using a pyridine based solution CuAc, InCl₃ TU and P3EBT. As before, a simple device architecture with no interface layers at the electrodes was used, devices were prepared as stated in section 7.5.2. Solar cell parameters are outlined in Table 22.

Table 21: Overview of heating programs used

sample	heating device	atmosphere	T _f / °C	heating program
A	magnetic stirrer	Ar	160	120 °C $\xrightarrow{15 \text{ min}}$ 120 °C $\xrightarrow{3 \text{ min}}$ 160 °C $\xrightarrow{15 \text{ min}}$ 160 °C
B	tube furnace	N ₂	160	RT °C $\xrightarrow{3 \text{ min}}$ 80 °C $\xrightarrow{16 \text{ min}}$ 160 °C
C	tube furnace	N ₂ -stream	160	RT °C $\xrightarrow{3 \text{ min}}$ 80 °C $\xrightarrow{16 \text{ min}}$ 160 °C $\xrightarrow{18 \text{ min}}$ 160 °C
D	tube furnace	N ₂ -stream	180	RT °C $\xrightarrow{3 \text{ min}}$ 80 °C $\xrightarrow{20 \text{ min}}$ 180 °C $\xrightarrow{14 \text{ min}}$ 180 °C
E	tube furnace	N ₂ -stream	200	RT °C $\xrightarrow{3 \text{ min}}$ 80 °C $\xrightarrow{24 \text{ min}}$ 200 °C $\xrightarrow{10 \text{ min}}$ 200 °C
F	tube furnace	vacuum	180	RT °C $\xrightarrow{3 \text{ min}}$ 80 °C $\xrightarrow{20 \text{ min}}$ 180 °C $\xrightarrow{10 \text{ min}}$ 180 °C

The heating program significantly influences solar cell performance. The most important parameter is the heating rate, devices heated at 5 °C/min show almost double device efficiency (0.10 % compared to 4.6e⁻² % in the samples A and C). Isothermal annealing at T_f further increases photovoltaic action, as can be seen by comparison of sample B and C, probably due to incomplete reaction when the final annealing stage is not applied. A final temperature of 180 °C with a 10 minute isotherm at the same temperature under vacuum conditions returned a device with a PCE of 0.35%, compared to 0.16% obtained using the

same heating program and a N₂-stream. Vacuum conditions are supposed to favour the formation of the inorganic phase by shifting the equilibrium to the product side, as the decomposition of thiourea yields gaseous products. When the final temperature is set to 200 °C, PCE again deteriorates (0.13%), most likely due to polymer decomposition (compare preceding section).

Table 22: Solar cell parameters

	η / %	V_{oc} / mV	i_{sc} / $\mu\text{A}\cdot\text{cm}^{-2}$	FF	V_{mpp} / mV	i_{mpp} / $\mu\text{A}\cdot\text{cm}^{-2}$
A	4.6 e^{-2}	390	284	0.25	180	154
B	0.08	585	362	0.23	270	180
C	0.10	420	607	0.23	200	300
D	0.16	510	600	0.31	255	376
E	0.13	420	705	0.27	220	361
F	0.35	516	1305	0.31	276	728

7.6.7 Conclusion

XRD data showed the formation of the inorganic phase starting at temperatures above 100 °C, at higher temperatures the (112) reflection of CuInS₂ gains intensity. The heating rate is a crucial parameter of the annealing process, TGA showed distinct differences when samples were heated at slow (5 °C/min) or at fast rate (20 °C/min). This finding is consistent with the parameters obtained from hybrid solar cells obtained by different annealing procedures, where it was shown, that devices heated at slow rate clearly outperform devices heated at fast rate. After an initial period (RT-100 °C), where predominantly pyridine escapes from the sample, mass spectra indicate that the formation of the inorganic phase is already starting at ca. 100 °C (compare IC-43 in Figure 55). Most likely, acetate fragments leave the sample, corresponding to a reorganization of the initial metal-thiourea-pyridine complexes; at temperatures below 120 °C the decomposition of thiourea is assumed to play a minor role. Using mass spectrometry it was possible to identify side reactions in the in-situ formation of the acceptor phase, as a main by-product melamine was identified, which is formed at a temperatures > 125 °C. The compound is formed by reaction of three thiourea molecules and is assumed to have negative impact on solar cell action. High temperatures are favourable for the formation of CuInS₂ (thin films CIGS cells are processed at temperatures in the range of 400-600 °C

[240]), but definitely are not for conjugated polymers. This was demonstrated by FT-IR, where it was shown, that significant decomposition of P3EBT takes place at temperatures ≥ 180 °C, whereas 180 °C seem to be compatible with the material. This is consistent with the results on bulk-heterojunction devices, where a final temperature of 180 °C under vacuum conditions returned the highest PCE of 0.35%.

7.7 Incorporation of Zn, Acceptor Phase Stoichiometry and Solar Cell Action

7.7.1 Introduction

In the development of inorganic CuInSe₂ thin-film solar cells incorporation of Ga and S was utilized for optimization of bandgap and transport properties, whereas compound formation with elements from different groups of the periodic system (so far reported for Mg, Cd and Zn) has not been studied with comparable vigour, probably due to multitude of structural possibilities. Inclusion of Zinc yields ZnS_{2x}.(CuIn)_{1-x}S₂-type compounds (ZCIS), analogous Mg- and Cd-structures are known as well [208],[241],[242]. Incorporation of Zn results in increased bandgaps and V_{OC}-values in thin film solar cells [207], therefore the behaviour P3EBT-ZCIS hybrid solar cells is explored in this section. The second major aspect of this chapter is the investigation of the stoichiometry of the active layer. Due to a higher volatility of indium compounds [243] compared to copper compounds, proper stoichiometry of the film after the annealing reaction can be adjusted by altering the composition of the precursor solution. This task was addressed by the preparation of active layer films of different Cu- and In- and Zn-stoichiometry and subsequent analysis of the annealed films by SEM-EDX.

7.7.2 Hybrid P3EBT-ZCIS Solar Cells

While In to Cu ratio was kept constant at 1.7 (% at.), different contents of Zn were added to the precursor solution (as Zn(Ac)₂, compare Table 23), which was subsequently spin-coated onto ITO-substrates and annealed using heating program **F** (RT $\xrightarrow{3\text{min}}$ 80 °C

→ 20 min → 180 °C → 14 min → 180 °C). Device preparation was performed as described in section 7.5.2, donor / acceptor ratio is 1 / 3 (wt.), P3EBT concentration was 6 mg.mL⁻¹. A reference device with a CuInS₂ acceptor phase was included for comparison.

Table 23: Composition of ZCIS precursor solutions

Cu / In / Zn / TU	c (CuAc) / mg.mL ⁻¹	c (InCl ₃) / mg.mL ⁻¹	c(Zn(Ac) ₂) / mg.mL ⁻¹	c (TU) / mg.mL ⁻¹
1 / 1.7 / 0.05 / 10	9.2	27.6	1.4	60.2
1 / 1.7 / 0.1 / 10	9.2	27.6	2.7	60.3
1 / 1.7 / 0.2 / 10	9.2	27.6	4.1	60.0
1 / 1.7 / 0.3 / 10	9.2	27.6	5.4	60.3
1 / 1.7 / 0.5 / 10	9.2	27.6	6.8	60.2

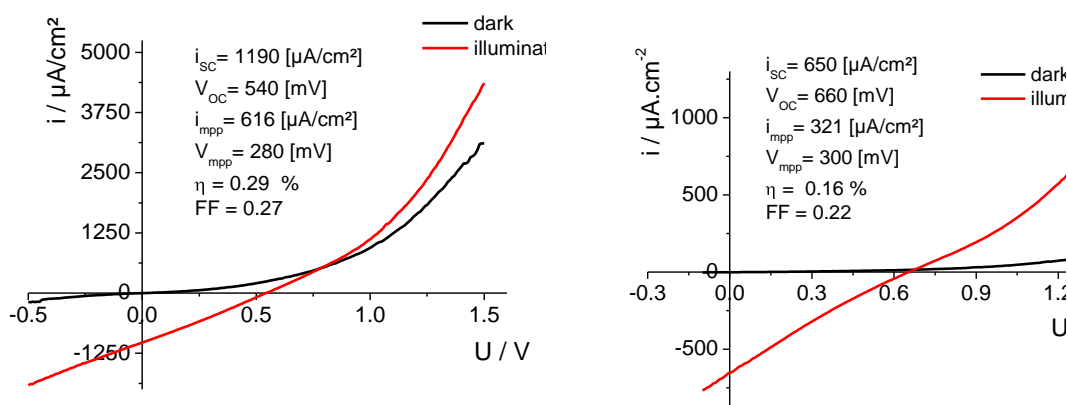


Figure 60: I-V curves of a P3EBT-CIS device (left) and a P3EBT-ZCIS device containing 0.5 at.% Zn

Figure 60 shows two typical i-V curves: Left hand side is showing the characteristics of the reference device with a CuInS₂ acceptor phase, while on the right hand side shows the device containing the highest Zn-content in this series ($c(\text{Zn}) = 0.5 \text{ } \%$ at.). The obvious feature of devices with a ZCIS acceptor are elevated V_{oc} -values (588-690 mV compared to 540 mV of the reference device, see Table 24; i-V curves of the other samples can be found in appendix 10.5) while the fill factor decreases slightly. Optimum Zn-content in this experiment was found to be 0.1 % at., at this value both V_{oc} and i_{sc} are increased by a factor of ca. 1.2 compared to the reference device. Further increase of the Zn-content augments device voltages up to 690 mV, however, at expense of the short circuit current.

This behaviour is in accordance with the situation in thin-film CuInS₂ devices [208], the increase in V_{oc} however is accompanied by an increase of the serial resistivity of the device (which is consistent with the flat shape of the dark i-V curve). When zinc contents are > 0.1 %at. this behaviour becomes dominant und photocurrents decrease.

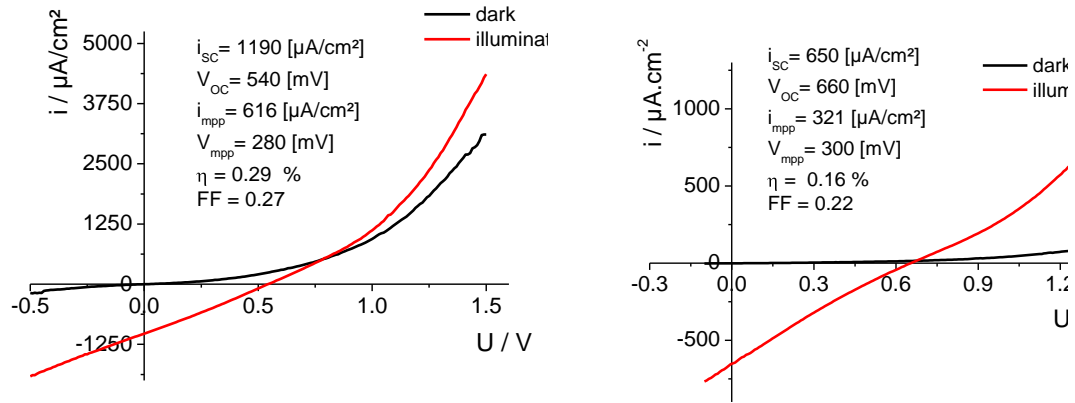


Figure 61: i-V curves of a P3EBT-CIS- (left side) and a P3EBT-ZCIS device ($c(\text{Zn}) = 0.5$) (right side)

Table 24: Solar cell parameters of P3EBT-ZCIS devices with different stoichiometry

$c(\text{Zn})$	η / %	V_{oc} / mV	i_{sc} / $\mu\text{A}\cdot\text{cm}^{-2}$	FF	V_{mpp} / mV	i_{mpp} / $\mu\text{A}\cdot\text{cm}^{-2}$
0	0.29	540	1190	0.29	280	616
0.05	0.27	588	1290	0.27	268	614
0.1	0.42	660	1433	0.27	340	746
0.2	0.31	690	1271	0.31	300	628
0.3	0.22	676	911	0.22	300	444
0.5	0.16	660	650	0.22	300	321

7.7.3 ZCIS-Precursor Stoichiometry - Active Layer Morphology – Active Layer Stoichiometry

From chapter 7.3, where precursor solutions of different stoichiometry were analyzed with respect to solar cell performance, an Indium excess of 1.7 %at. was used for the consecutive experiments. In the preceding section, Zn-content in ZCIS-type acceptors was varied and a with best results for 0.1 at.% Zn. In this chapter, Cu to In ratio was studied using SEM methods, while In-content was fixed at 0.1 at.%. Measurements were made by

Thomas Rath at the Technical University of Tallin, which is gratefully acknowledged. P3EBT-ZCIS precursor solutions were spin coated onto CaF_2 substrates and subject to the heating routine as outlined in part 7.6.6 (program F: (RT $\xrightarrow{3\text{ min}}$ $80\text{ }^\circ\text{C}$ $\xrightarrow{20\text{ min}}$ $180\text{ }^\circ\text{C}$ $\xrightarrow{14\text{ min}}$ $180\text{ }^\circ\text{C}$). Layer morphology was examined by SEM, stoichiometry was probed using SEM-EDX.

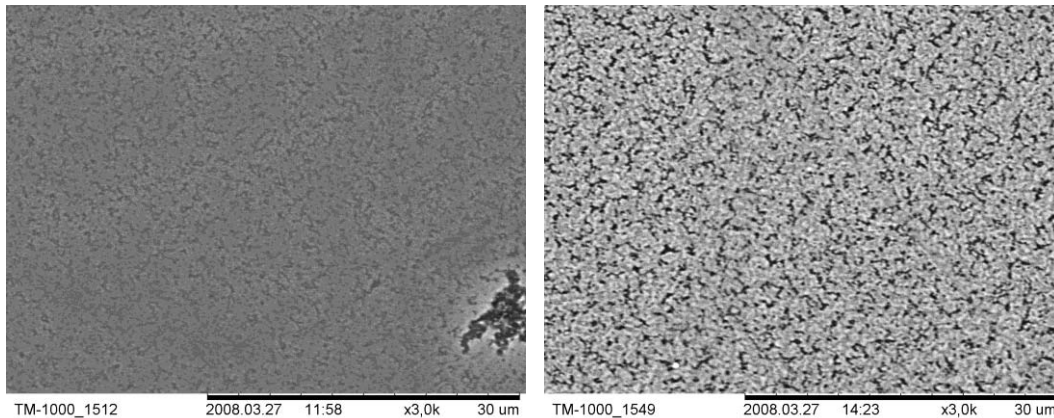


Figure 62: SEM-micrographs of two active layers: Left side: Cu / In = 1/1, right side: Cu / In = 1/2

Figure 62 shows two of the obtained SEM-images. Apart from differences in the brightness of the images, the morphology of the two samples is very similar, even though the In-content of the precursor solutions differs by a factor of two. As all of the samples investigated show a comparable morphology, supplementary SEM images were can be found in appendix 10.7. Additional information was obtained from a view on the cross section of a device, which is shown in Figure 63:

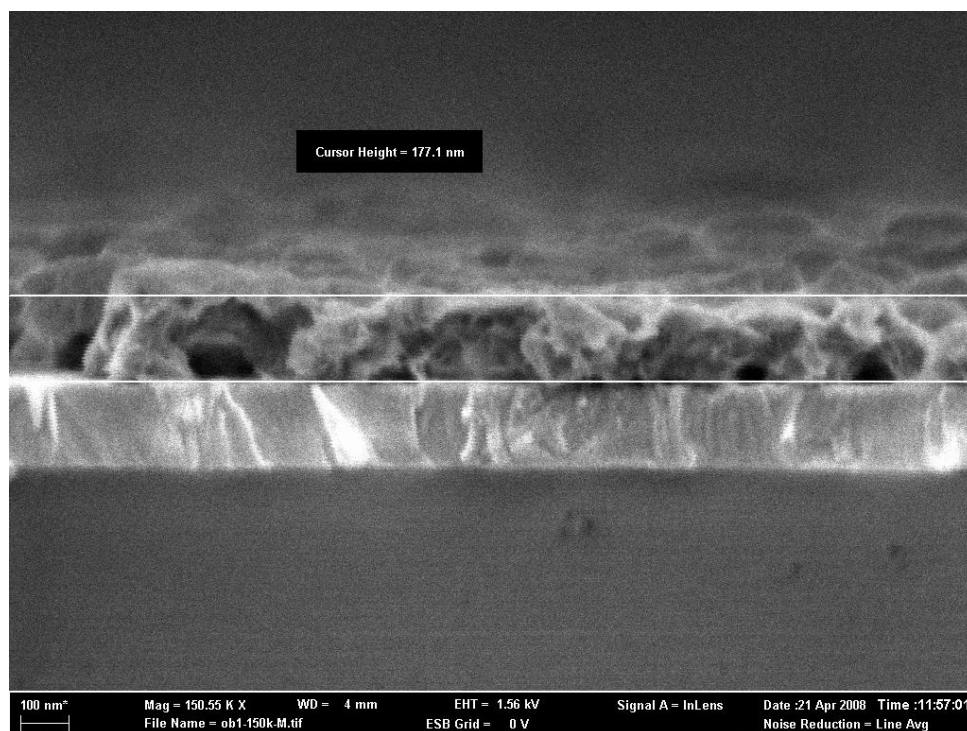


Figure 63: SEM view on the cross section of a P3EBT-ZCIS active layer (Cu/In/Zn = 1/2/0.1)

The active layer is located in the middle of the image, on top of ITO-covered glass. The film shows a porous appearance, probably due to the evaporation of gaseous products during the formation of the inorganic phase. The bulky motives show dendritic substructures which show good interconnection, active layer was determined to be ca. 180 nm.

Investigations on the stoichiometry were performed using SEM-EDX. Results are plotted in Figure 64 (listings of the analyses can be looked up in appendix 10.6). Indium to Copper ratio of the precursor solution is plotted on the x-axis, the metal- and metal to sulfur ratio in the active layer (determined by SEM-EDX) is plotted on the ordinate.

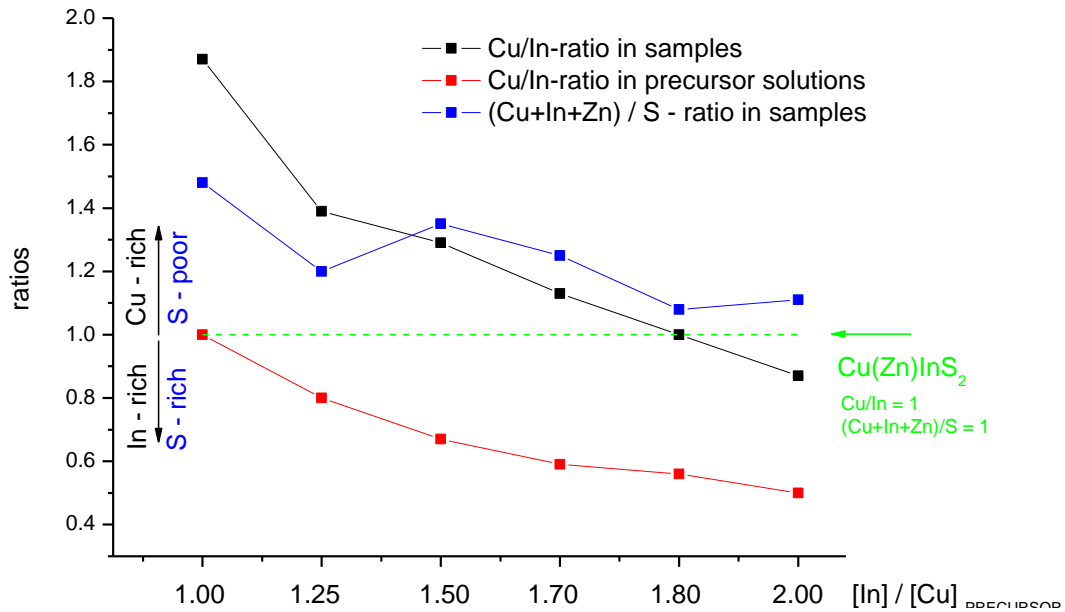


Figure 64: Active layer composition (determined by SEM-EDX) vs. precursor composition

It is readily seen, that a dramatic decrease of the Indium content occurs upon the annealing procedure of the samples; whereas in the 1/1 precursor sample 46% of the Indium is evaporated from the thin film, this value increases up to nearly 90% in the 2/1 (In/Cu)-precursor film. Zn-content (not explicitly plotted in) is not subject to as pronounced variations (values ranging from 0.10 – 0.12 at.%, compare appendix 10.6), however sulfur deficient compounds are obtained in all experiments. An Indium excess of ca. 1.8 at.% yields an acceptor phase with equal amounts of Cu and In. this finding is in good correlation with the results obtained from the solar cell experiments, where a In content of 1.7 %at. showed best results.

7.8 Conclusion

This chapter illustrated the development of P3EBT – CuInS₂ hybrid solar cells. The applicability of the in-situ approach for the generation of donor-acceptor blends was demonstrated by XRD, consequently the application of polymer-CIS films as active layers in solar cells was elaborated. The in-situ preparation of the composite turned out to be a delicate task, for a bulk heterojunction-type active layer (at least) four constituents are required to make up a molecular dispersion in the precursor solution. After experiments

with bilayer heterojunction devices (optimization metal stoichiometry) and acetonitrile-pyridine mixtures, a precursor system consisting of CuAc, InCl₃, TU and P3EBT dissolved in pyridine showed promising photovoltaic action. The system then was optimized in terms of the donor / acceptor ratio and precursor concentration. Special emphasis was put on the analysis of the annealing procedure, which proved to be the decisive preparation step. The formation of CuInS₂ starts at temperatures of ca. 120 °C, as was shown by online-XRD measurements. Thermogravimetric analysis of the annealing process revealed considerable differences in terms of the heating rate. Correspondingly devices annealed at a slow heating rate (5 °C/min, T_f = 180 °C) showed distinctly better PCE than devices obtained by a fast heating ramp (0.35 vs. ~0.05 %). Chemical analysis was performed by mass spectrometry, which revealed the formation of melamine as a side product, while FT-IR spectroscopy showed that temperatures beyond 180 °C are not compatible with P3EBT. Finally zinc was incorporated into the acceptor phase (with Zn(Ac)₂ as precursor component), yielding a ZnS_{2x}·(CuIn)_{1-x}S₂ (ZCIS)-type acceptor phase. ZCIS-P3EBT active layer morphology as well as stoichiometry was probed by SEM and SEM-EDX, showing extensive indium loss during the annealing reaction of the active layer. The results showed good correlation to PCE of the devices, which reached values of 0.42%.

8 Stability Testing of Plastic Solar Cells

8.1 Introduction

Besides device efficiencies well below values of inorganic devices, one major issue of plastic solar cells seeking improvement is their stability. This is predominantly due to the reactivity of the conjugated system, which can react with impurities such as oxygen or water on one hand, on the other hand photochemical processes not necessarily involving external reaction partners are possible [244-246]. This section will consider stability testing of polymer-PCBM – combinations (F8T2-, MEH-PPV-, P3HT – PCBM), stability tests of hybrid solar cell systems with a CuInS₂ acceptor are the second focus of this section (PPV-CIS, MEH-PPV – CIS, MDMO-PPV – CIS, F8T2 – CIS). As throughout the thesis, acceptor phase was obtained using an in-situ processes [23],[24],[247]. Details of the testing-setup are described in section 4.3.

8.2 Stability of Polymer – PCBM Solar Cells

Three polymer-PCBM combinations were tested for their stability: (1) MEH-PPV – PCBM, (2) F8T2 – PCBM and (3) P3HT – PCBM. Devices were prepared by spin coating from chloroform solutions as outlined in Table 25, following the procedures outlined in [135],[96],[145], respectively. At the anode a PEDOT-PSS (Baytron VPAI-4083) interface layer was deposited by spin coating (200 rpm / 200 rpm.s⁻¹ / 30 s), the aluminium cathode (thickness 200 nm, electrode area = 0.1 cm²) was evaporated using a Baltec MED-020 unit. Solar cells were encapsulated with a glass slide which was glued onto the substrate using two component epoxy glue (UHU® plus 5 min epoxy) , the resin was cured for two hours (pot life of resin: 5 minutes, minimal curing time: 1 hour) in nitrogen atmosphere (compare section 4.1). After the curing process the devices were removed from the glove box and examined in the testing under permanent illumination of a sulfur-plasma lamp (iV-no-bias mode, no spectral mismatch correction).

Table 25: Production parameters of polymer – PCBM devices

System	c (Poly.) / mg.mL ⁻¹	c (PCBM) / mg.mL ⁻¹	solvent	spin coating parameters
MEH-PPV - PCBM	4	16	CHCl ₃	500 rpm / 500 rpm.s ⁻¹ / 30s
F8T2 – PCBM	5	5	CHCl ₃	500 rpm / 500 rpm.s ⁻¹ / 30s
P3HT - PCBM	10	8	CHCl ₃	2000 rpm / 2000 rpm.s ⁻¹ / 30s

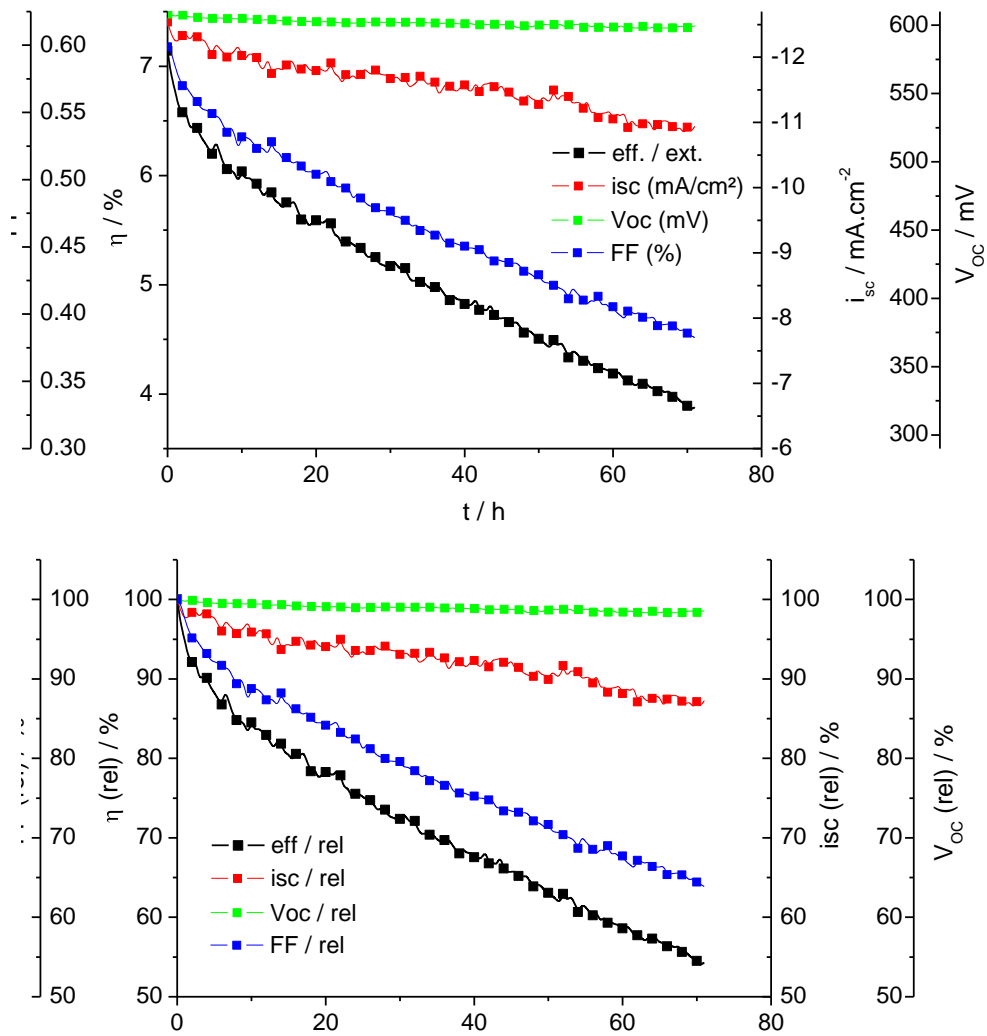


Figure 65: Solar cell parameters of a P3HT-PCBM device under permanent illumination with a sulfur plasma lamp; $P_{(in)} = 670 \text{ W.m}^{-2}$, no spectral mismatch correction. Top / bottom: absolute / relative values

Figure 65 shows the results obtained for a P3HT-PCBM solar cell. Data of MEH-PPV – PCBM and F8T2 – PCBM are compiled in appendix 10.8, main results are summarized in Table 26 as well as in Figure 66.

Table 26: Stability of polymer – PCBM solar cells

system	testing-mode	$\eta(i) / \%$	$t(80\%) / h$	$t(50\%) / h$	$t(20\%) / h$	main loss parameters
MEH-PPV - PCBM	iV-noBias	1.1	1.5	-	$h(7.5h) = 55\%(rel)$	i_{sc} , FF
F8T2 – PCBM	iV-noBias	0.8	2	10	37	i_{sc} , FF
P3HT – PCBM	iV-noBias	4.6	15	-	$h(70h) = 54\%(rel)$	FF, i_{sc}

Rather elevated PCE-values in Figure 65 are due to illumination with a sulphur plasma lamp, for this reason the initial PCEs ($\eta(i)$) of the devices are listed in Table 26 (illumination with solar simulator). Figure 65 shows a rapid decrease of FF and i_{sc} in the initial stage of the test, after approx. 5h roughly linear diminution of the PCE is observable. After 15 hours device performance is at 80% of its initial value, at the end of the test (70h) PCE is 54% of the initial value. Parameters especially subject to degradation are the fill factor and the short circuit current, while the open circuit voltage remains almost at its starting value (99% after 70h).

A comparison of the relative PCE values of the three polymer-PCBM systems is shown in Figure 66. While the profile of PCE vs. t shows a linear shape in case of the P3HT-PCBM system (at this scale; compare Figure 65), PCE of the MEH-PPV and F8T2 devices exponentially decreases. Another distinct difference of the latter two systems is that the short circuit current is the principal loss parameter, whereas in the P3HT device it is the fill factor. Such behaviour is in accordance with literature [248] and the higher reactivity of PPV- and polyfluorene-type polymers; the conjugated system degrades more rapidly, as a consequence charge transport (and hence the i_{sc} value) deteriorates.

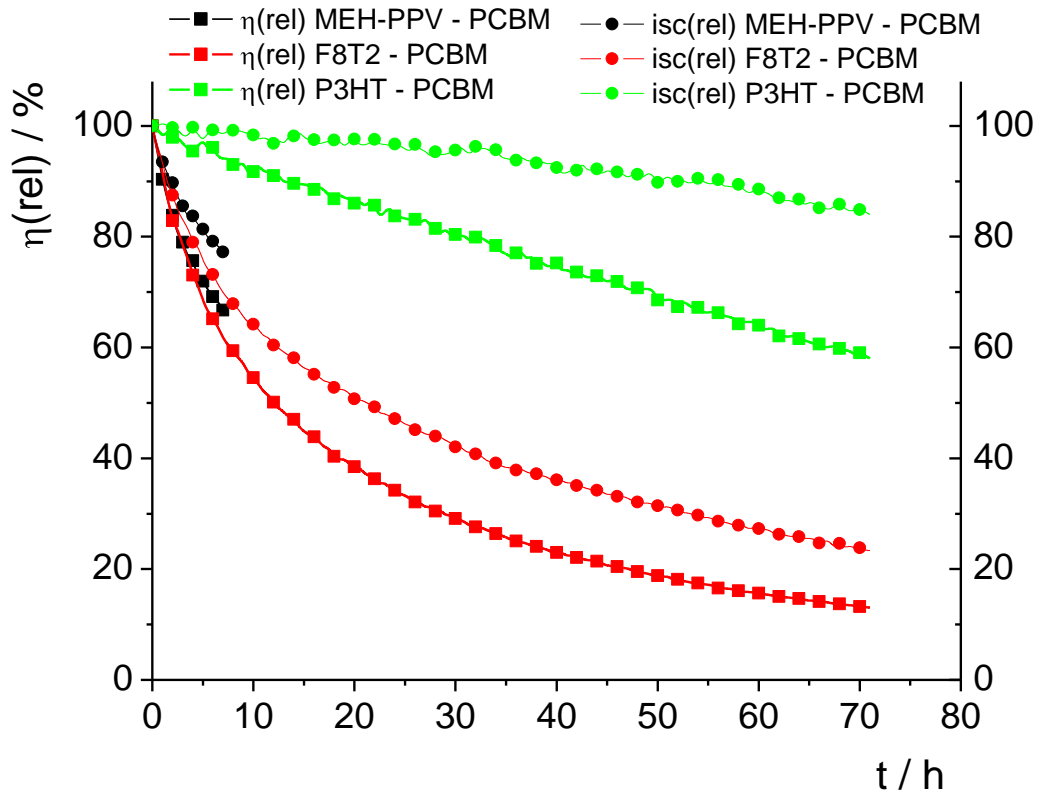


Figure 66: Relative PCE and i_{sc} values as a function of time for the three polymer – PCBM systems

8.3 Stability of Polymer – CuInS_2 Solar Cells

This section deals with the time dependent behaviour of polymer- CuInS_2 solar cells. First the stability of the PPV-CIS system described in chapter 6 was investigated, while device-stability of different polymers (MEH-PPV, MDMO-PPV and F8T2) was investigated in connection with a CuInS_2 -acceptor phase obtained by a recently developed precursor route [249],[250]. All devices had an active area of 0.1 cm^2 , encapsulation (glass-epoxy) is described in the preceding section.

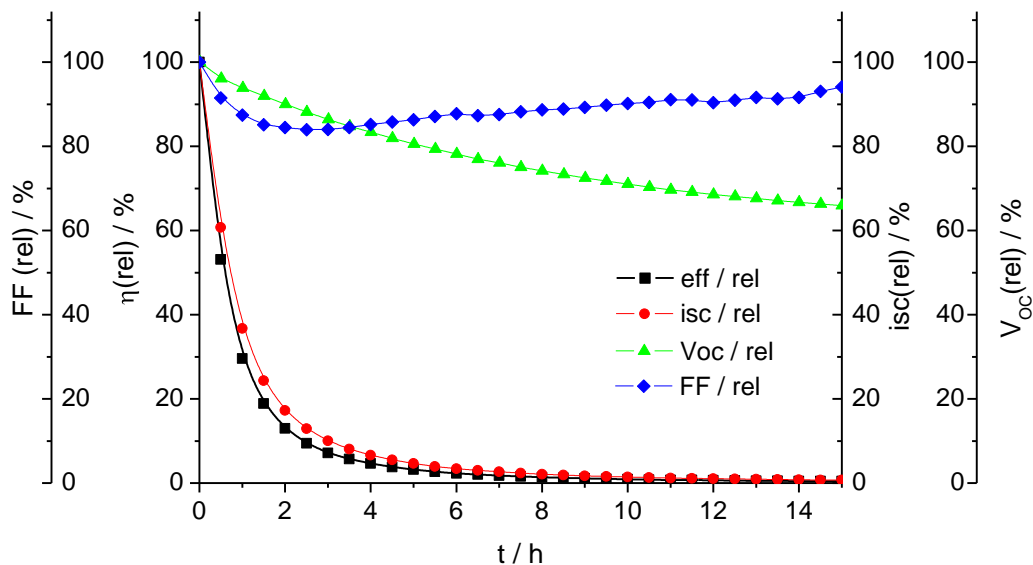


Figure 67: Device parameters of PPV-CIS solar cell (relative values); $P_{(in)} = 1010 \text{ W.m}^{-2}$ (sulfur plasma lamp)

The relative values of the solar cell parameters are shown in Figure 67 (absolute values are located in appendix 10.8); device performance is 53 %(rel.) after 30 minutes, after 5 hours PCE is 3% of its initial value. The rapid degradation is predominantly due to the decrease in the short circuit current, while V_{OC} and fill factor are less affected.

Stability data for the new CIS - precursor system are summarized in Table 27, the respective plots are located in appendix 10.8:

Table 27: Stability data for CIS - polymer solar cells

system	testing-mode	$\eta(i) / \%$	$t(80\%) / h$	$t(50\%) / h$	$t(20\%) / h$ v $\eta(t)$	main loss parameters
MEH-PPV - CIS	iV-noBias	0.90	1.5	7.5	$\eta(35.5h)=22.8\%$	i_{sc} , FF
MDMO-PPV - CIS	iV-noBias	0.92	1.0	8.0	23.0	i_{sc} , FF
F8T2 - CIS	iV-noBias	0.51	2.5	-	$\eta(35.5h)=56\%$	i_{sc} , V_{OC}

Compared to PPV-CIS solar cells stability values could be increased considerably, the F8T2-CIS system showing best performance after the continuous illumination of approx. 36 hours (56% of initial performance):

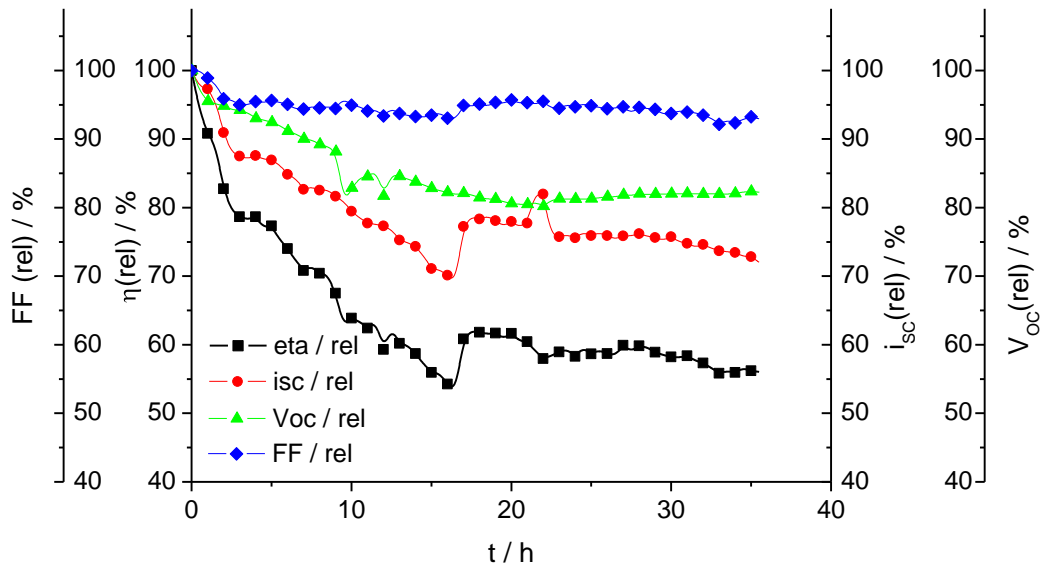


Figure 68: Relative solar cell parameters of a F8T2 – CIS solar cell; $P_{(in)} = 1010 \text{ W.m}^{-2}$ (sulfur plasma lamp)

Solar cell parameters of the F8T2-CIS device are plotted in Figure 68 (relative values), comparison with Figure 66 shows that the F8T2-CIS device exhibits greater stability than the corresponding PCBM device. Among the four tested hybrid systems, F8T2 clearly shows best stability values, which is shown in Figure 69. Degradation of the MEH- and MDMO-PPV-based CIS devices is comparable to the MEH-PPV – PCBM solar cell. As in case of the MEH-PPV – PCBM and the F8T2 – PCBM combinations, the decrease in the short circuit current most strongly affects the reduction of solar cell action.

8.4 Conclusion

This section focused on the testing of plastic solar cells under continuous illumination. Strong degradation effects were observed for all systems under investigation; highest stability was observed for the P3HT – PCBM system, among the hybrid solar cells F8T2 – CIS was found to be most stable, with about half of the degradation observed in the P3HT – PCBM device. As a common feature of all investigations especially charge transport was adversely affected by continuous illumination, short circuit currents and fill factors most strongly deteriorated under the conditions of the test, which was very pronounced in the PPV-CIS combination. Comparison with literature data (especially with data on PCBM systems, whereas much fewer dedicated publications on the stability of hybrid solar cells

are available, e. g. [251-253] shows similar behaviour [254], additional improvement is reported from the applications of suitable cathode interface layers [255-257]).

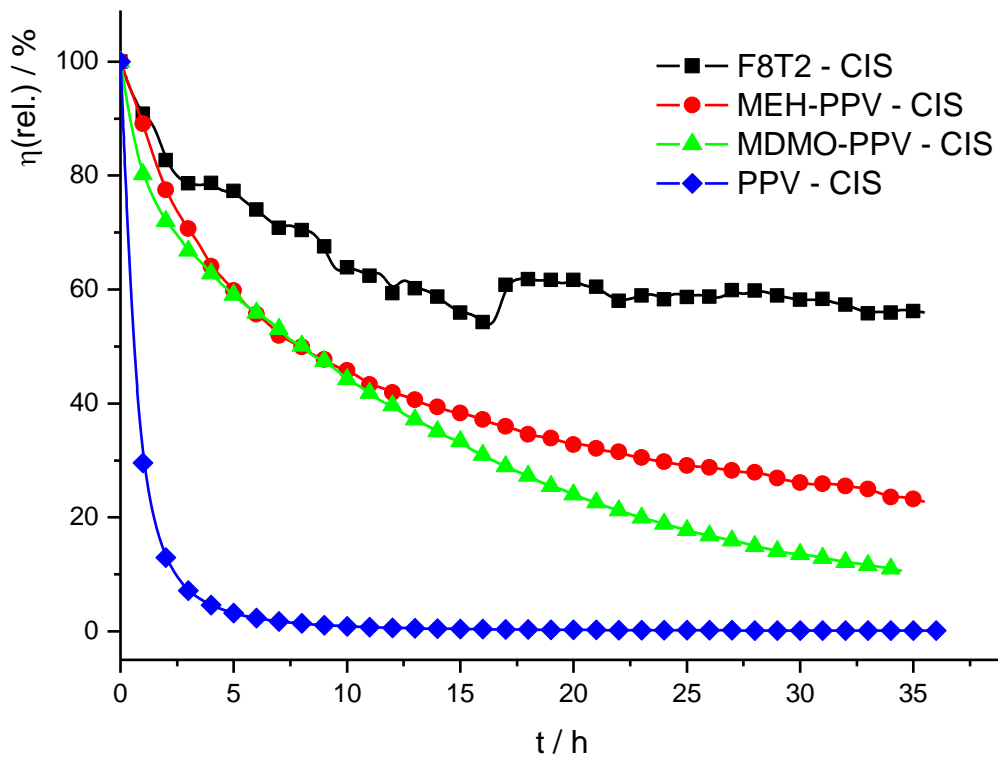


Figure 69: Relative efficiency values for the four different polymer – CuInS₂ systems

9 Summary and Outlook

Summary

The subject of this thesis was the preparation of organic-inorganic composite semiconductor layers and their subsequent application as active layer in hybrid heterojunction solar cells. In a second part, a multi-channel stability testing facility was constructed, which allows to monitor solar cell performance under permanent illumination. The composite layers were obtained using a novel in-situ approach, where the acceptor phase (CdS , CuInS_2 or $(\text{ZnS})_{2x}\cdot(\text{CuIn})_{1-x}\text{S}_2$) is formed by the reaction of metal ions (Cd^{2+} , Zn^{2+} ; Cu^+ , In^{3+}) by thermal decomposition of a sulfur source (thiourea / thioacetamide) in the composite film. This approach bears the advantage that, (I) no separate synthesis procedure for the acceptor phase is necessary and the donor-acceptor composite is directly obtained as a thin film and, (II) no capping agents are necessary to prevent the agglomeration of the nano-structured acceptor phase. In the conventional approach, the capping agents (which are difficult to remove) deteriorate exciton dissociation and charge transport, as their presence at the donor-acceptor interface represents a high energetic barrier for these processes.

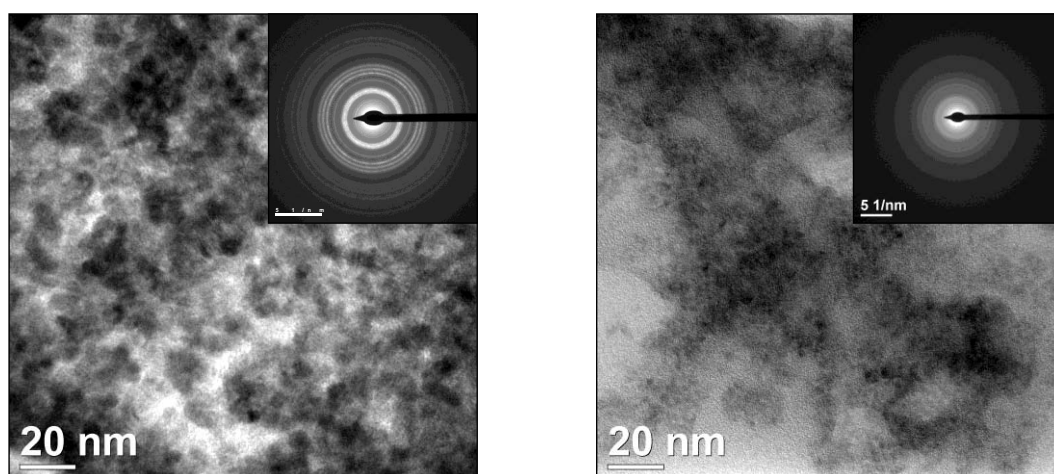


Figure 70: TEM-micrographs and SAED data (inset) for the CdS-P3EBT (left) and for the ZnS-P3EBT composite (right)

The in-situ formation of composite layers consisting of a binary semiconductor (CdS , PbS and ZnS) and P3EBT (Poly-3-(ethylbutanoate)-thiophene) was demonstrated in chapter 5.

Structural analysis was performed using XRD and TEM-SAED, the obtained values were in very good agreement with literature data. From the FWHM of the reflections primary crystallite sizes of 4.3 and 4.6 nm were obtained for CdS and ZnS, respectively, which is in good agreement correlation with the obtained TEM micrographs, which show also the formation of larger aggregates (compare Figure 70). In case of the PbS – P3EBT blend, bulk material with crystal sizes of approx. 200 nm was obtained. The composites were used as active layer in hybrid bulk heterojunction solar cells, the CdS – P3EBT system showed a substantial photovoltaic effect with a PCE of 0.066 %. In case of ZnS – P3EBT blend a photovoltage of 610 mV could be observed, whereas the PbS – P3EBT film is not suitable for PV-applications, as particle diameters (ca. 200 nm) are too large to observe quantum-confinement effects and the bandgap remains at its bulk value of 0.4 eV.

Nanocomposites of CuInS₂ and PPV were obtained adapting the procedure from [23]. The system showed promising photovoltaic activity with PCE values of up to 0.75 %, however at the expense of reproducibility and stability. The age of the precursor was identified as the most influential parameter for photovoltaic activity. Stability testing of PPV – CIS devices revealed a half-live of only 30 minutes.

Heterojunction films of CuInS₂ and P3EBT were in the focus of chapter 7. Successful formation using the in-situ formation by decomposition of thiourea was shown by XRD, no secondary phases (e. g. Cu₂S) could be observed. Precursor composition and stoichiometry were optimized in bilayer heterojunction devices. CuAc and InCl₃ were identified as suitable precursor salts using pyridine as solvent. The optimum Indium content was determined to be 1.7 at.%. CuInS₂ – P3EBT bulk heterojunction solar cells were optimized with respect to donor - acceptor ratio and processing conditions. A 3/1 (wt./wt.) ratio of CuInS₂ / P3EBT returned best devices. Incorporation of Zn yields (ZnS)_{2x}.(CuIn)_{1-x}S₂ as acceptor material, which showed elevated V_{OC}-values of up to 690 mV in combination with P3EBT. Optimization of the precursor composition demonstrated that a substantial In-excess is necessary (as was found in the bilayer setup), optimum composition of the precursor solution was 1 / 1.7 / 0.1 (CuAc / InCl₃ / Zn(Ac)₂ (%at.)), which returned PCE values of 0.42%. This was confirmed by SEM-EDX, showing that a

significant amount of Indium is leaving the sample (up to 90% of the initial amount), while Cu and Zn amounts remained unchanged. At 80 % at excess of InCl_3 in the precursor solution, equal amounts of Cu and In are found in the composite layer after annealing at 180 °C. The Morphology of the active layer was studied by scanning electron microscopy, which showed similar results for different Zn-contents. The network structure of the active layer was revealed by a view on the cross-section of an active layer.

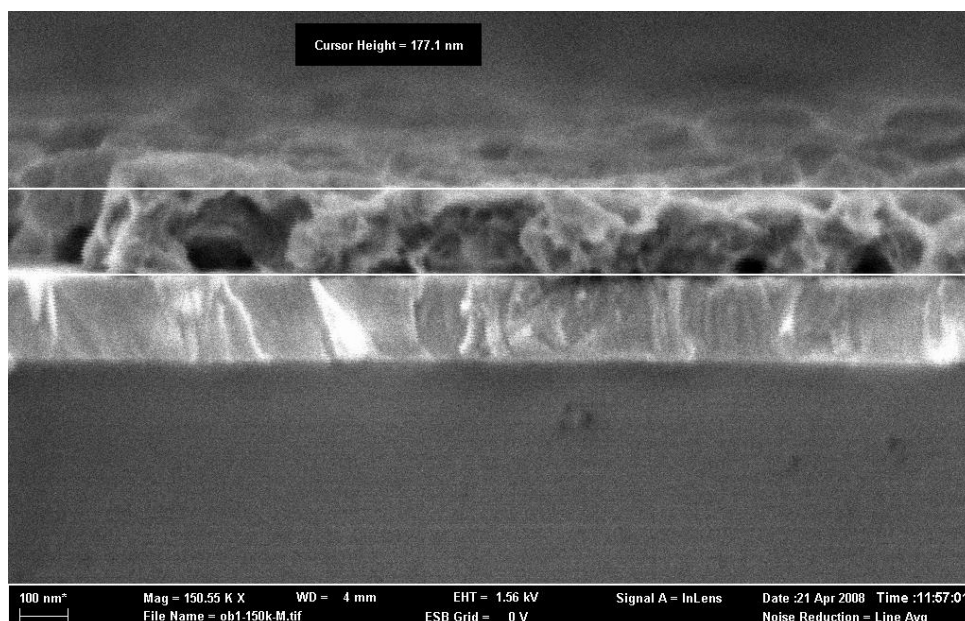


Figure 71: View on the cross section of a P3EBT-ZCIS active layer on top of a glass-ITO substrate

As the acceptor phase is generated in-situ by the thermolysis of thiourea, analysis of the annealing process was a central part of the work. The temperature dependent formation was examined in an online XRD-experiment. The formation of the acceptor phase starts at ca. 120 °C, the intensity of the CuInS_2 peaks augments with increasing temperature. It could also be shown, that heating rate and final temperature play a significant role on solar cell properties. Application of a slow heating rate with 5 °C/min to a final temperature of 180 °C gave superior results compared to a rate of 20 °C/min. This was confirmed by STA analysis of the decomposition reaction, showing substantial differences between the two different heating programs. Side product formation in during the decomposition of thiourea was probed by mass spectrometry. Starting at temperatures of ca. 125 °C the formation of melamine (mp = 350 °C (decomp.)) could be detected (which

was not possible by e. g. FT-IR spectroscopy). It is formed by condensation of three thiourea fragments and most likely adversely affects exciton dissociation and charge transport.

One of the parameters of polymer solar cells yet to improve is their stability. In order to investigate this aspect, a multi-channel testing setup was constructed, which allows the parallel testing of up to 15 devices. Three different polymer – PCBM systems (F8T2, MEH-PPV and P3HT) were investigated, testing of hybrid solar cells included MDMO-PPV, MEH-PPV and F8T2 in combination with CuInS_2 , a PPV-CIS device was tested as well. The devices were encapsulated using an epoxy resin to attach a glass cover. In case of fullerene systems, P3HT-PCBM combination showed best stability. Degradation was most pronounced in the PPV-CIS system (half live of 30 minutes), in the hybrid-series the F8T2-CIS system showed best stability values.

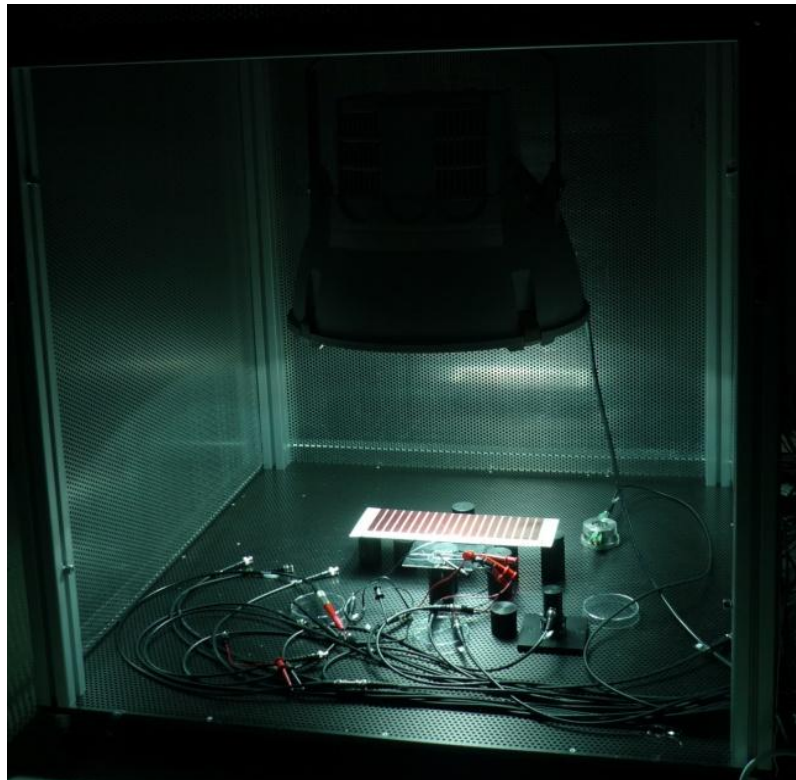


Figure 72: Illumination unit of the stability testing setup in action

Outlook

Research efforts in organic solar cells have considerably increased during the last two decades, after the milestones of Tang et al. in 1986 and Sariciftci et al. in 1995. Up to now, fullerene-based acceptors are in the centre of interest, while hybrid devices incorporating a nano-structured inorganic semiconductor as acceptor phase did not attract comparable attention. This is a surprise at first glance, hybrid systems can comprise the advantages of two material categories, compared to fullerenes they can exhibit high absorptivity and FO energies can be tuned. On the other hand, a common drawback of nano-scaled semiconductor particles is the need to stabilize them, as they are thermodynamically not stable. This involves application of capping agents, which are adsorbed on the surface of the nanocrystals and prevent agglomeration. This evidently has negative impact on exciton dissociation and charge transport, processes with strong dependence on a clean interface. For this reason in-situ formation of the inorganic phase was pursued in this work, no capping agents are required as the acceptor phase evolves within the matrix of the conjugated polymer ensuring an intimate contact of the two components. So far, in-situ formation of nanoparticles was utilized for the investigation of e.g. spectroscopic properties, whereas application in photonic devices has attracted little interest. Very recent publications on the theme [21],[22],[258], however, suggest this situation is changing, the promise of copper-free interfaces, hence unhindered charge transport indeed is attractive.

In-situ formation yet does not necessarily implicate the formation of clean interfaces, as could be shown for the P3EBT-CIS system, where melamine has been detected using mass-spectrometry. This example illustrates the demand for a clean chemistry, formation of side products should be suppressed and the precursor materials need to be decomposed quantitatively. From this viewpoint highly volatile or gaseous sulfur sources are most attractive, e. g. H_2S or HMDST could be interesting candidates. Considering molecular precursors, the side chain functionalities could be designed in a way favouring its decomposition by rearrangement or cleavage reactions.

Further improvement is expected from development of precisely engineered materials (combinations). Photon harvesting needs to be extended into the NIR-regime (nano-PbS is an interesting candidate in this respect) in order to generate high photocurrents, this can be achieved only with properly engineered band gaps and band offsets. So far plenty of research on organic-inorganic hybrid solar cells involved polymers originally developed for PLED applications, while (commercial) availability of low-bandgap absorbers is limited. The purity of the materials in use is of crucial importance, contaminations tend to accumulate on phase boundaries, defects can act as recombination centres in semiconductors. Probably we are to observe a development similar to semiconductor physics, and organic semiconductor devices become an everyday part of 21st century technology.

10 Appendices

10.1 Appendix 10.1: P3EBT Data

GPC Data

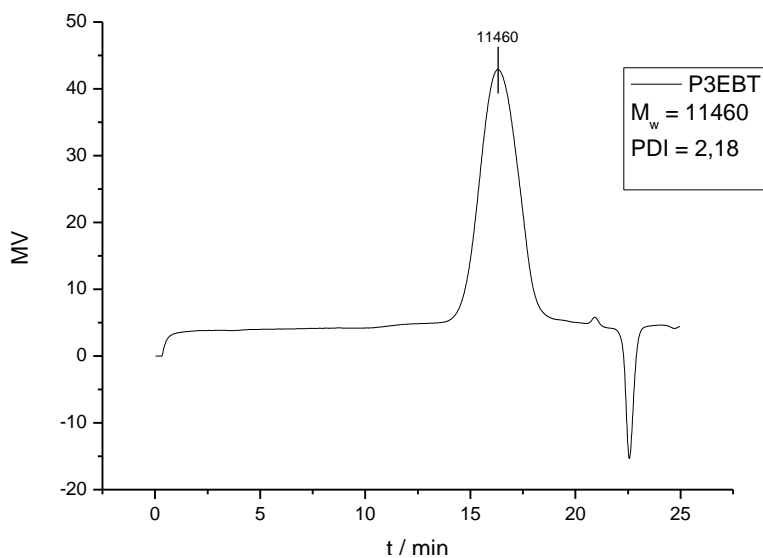


Figure 73: GPC chromatogram of P3EBT (CHCl_3 solution, PS calibration)

CV Data

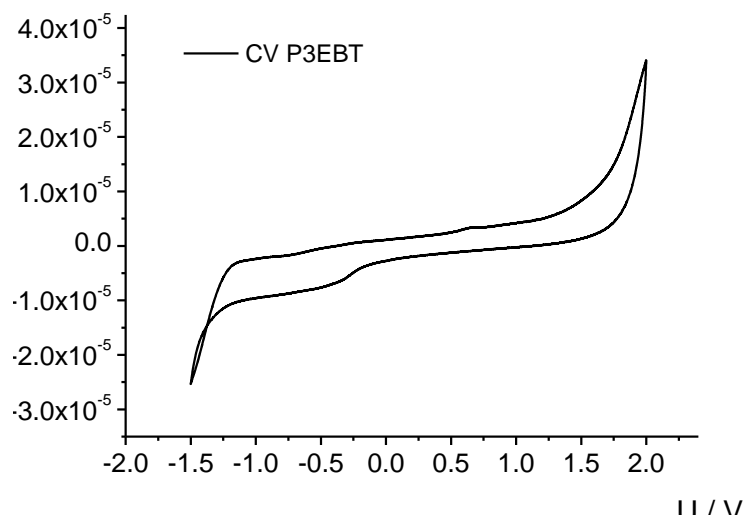


Figure 74: Cyclic voltammogram of a P3EBT layer on Pt (acetonitrile-TEABF electrolyte, calibration with $\text{Fe}(\text{cp})_2$)

10.2 Appendix 10.2: i-V Curves from P3EBT-CIS Devices with Different Donor and Acceptor Contents

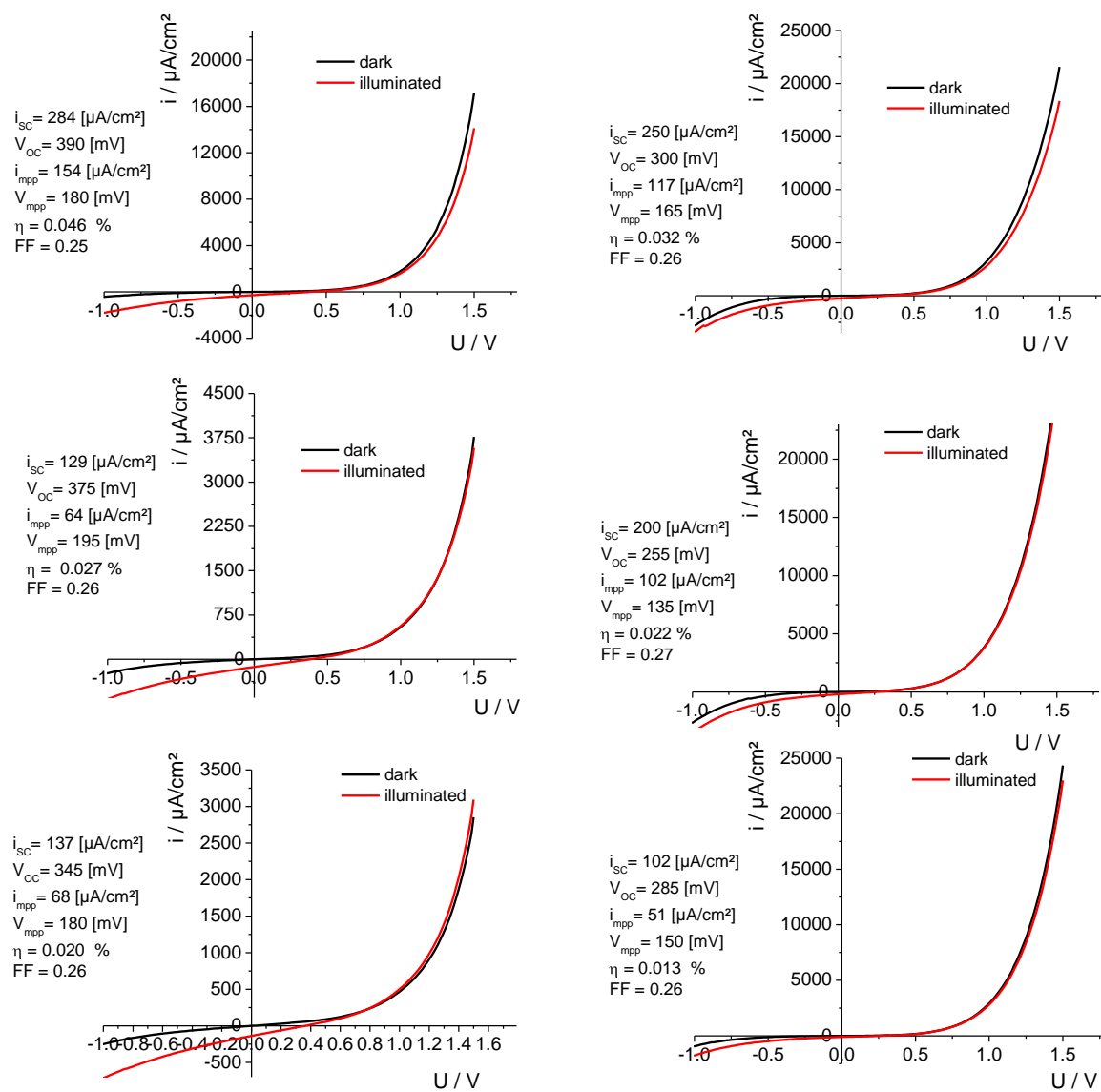


Figure 75: I-V curves from section 7.5: Left side: top: P3EBT-CIS 18-6, middle: P3EBT-CIS 18-8, bottom: P3EBT-CIS 18-10; right side: top: P3EBT-CIS 24-6, middle: P3EBT-CIS 24-8, bottom: P3EBT-CIS 18-10

10.3 Appendix 10.3: i-V Curves of P3EBT-CIS Devices Using Different Annealing

Procedures

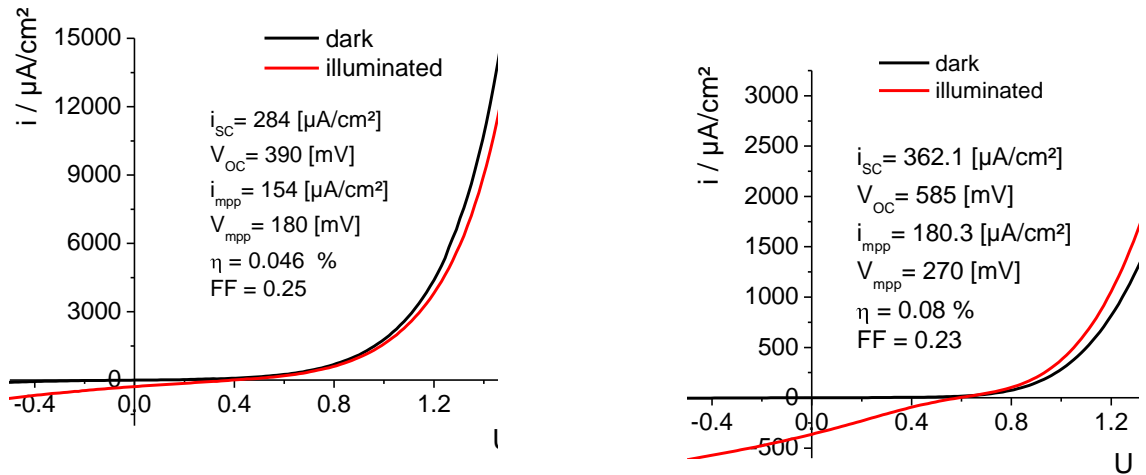


Figure 76: i-V curves from section 7.6.6: Left side: Sample A ($120\text{ }^{\circ}\text{C} \xrightarrow{15\text{ min}} 120\text{ }^{\circ}\text{C} \xrightarrow{3\text{ min}} 160\text{ }^{\circ}\text{C} \xrightarrow{15\text{ min}} 160\text{ }^{\circ}\text{C}$; glove box, magnetic stirrer); right side: Sample B ($\text{RT }^{\circ}\text{C} \xrightarrow{3\text{ min}} 80\text{ }^{\circ}\text{C} \xrightarrow{16\text{ min}} 160\text{ }^{\circ}\text{C}$; tube furnace, N_2 -stream)

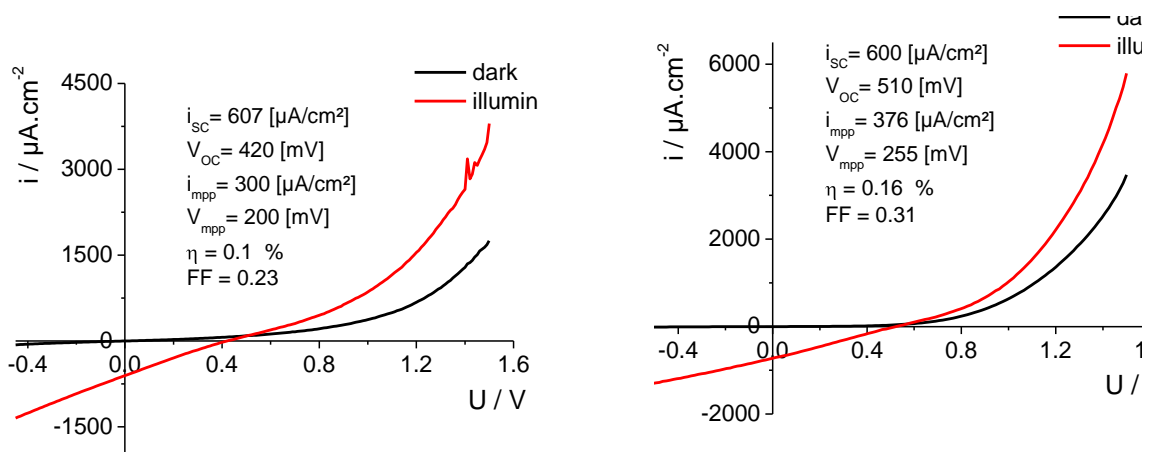


Figure 77: i-V curves of differently annealed samples. Left side: Sample C ($\text{RT }^{\circ}\text{C} \xrightarrow{3\text{ min}} 80\text{ }^{\circ}\text{C} \xrightarrow{16\text{ min}} 160\text{ }^{\circ}\text{C} \xrightarrow{18\text{ min}} 160\text{ }^{\circ}\text{C}$), right side: Sample D ($\text{RT }^{\circ}\text{C} \xrightarrow{3\text{ min}} 80\text{ }^{\circ}\text{C} \xrightarrow{20\text{ min}} 180\text{ }^{\circ}\text{C} \xrightarrow{14\text{ min}} 180\text{ }^{\circ}\text{C}$). Samples were annealed in a tube furnace under a N_2 -stream

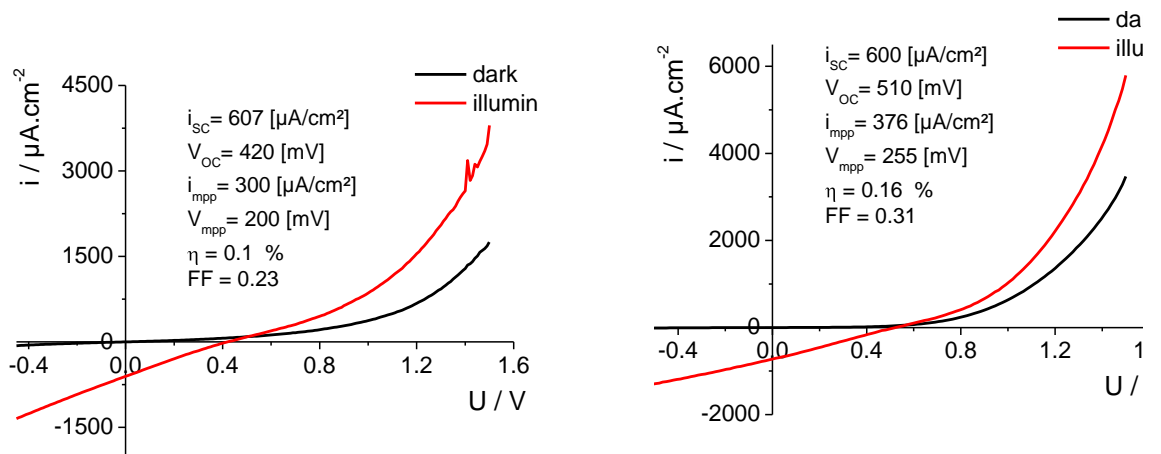


Figure 78: : i-V curves of differently annealed samples. Left side: Sample E (RT °C $\xrightarrow{3 \text{ min}}$ 80 °C $\xrightarrow{20 \text{ min}}$ 180°C $\xrightarrow{14 \text{ min}}$ 180 °C; tube furnace, vacuum); right side: Sample F (RT °C $\xrightarrow{3 \text{ min}}$ 80 °C $\xrightarrow{24 \text{ min}}$ 200°C $\xrightarrow{10 \text{ min}}$ 200 °C; tube furnace, N₂-stream)

10.4 Appendix 10.4: TGA Data of Active Layer Components, Mass Spectra

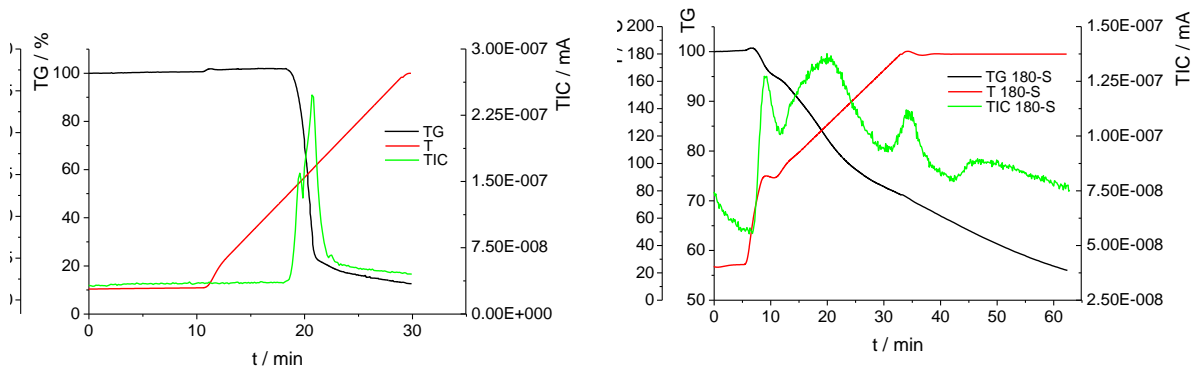


Figure 79: Left side: TG- and TIC-data for the decomposition of thiourea; right side: TG- and TIC-data for an active layer sample with TF=180 °C using heating routine 1 (compare Figure 52)

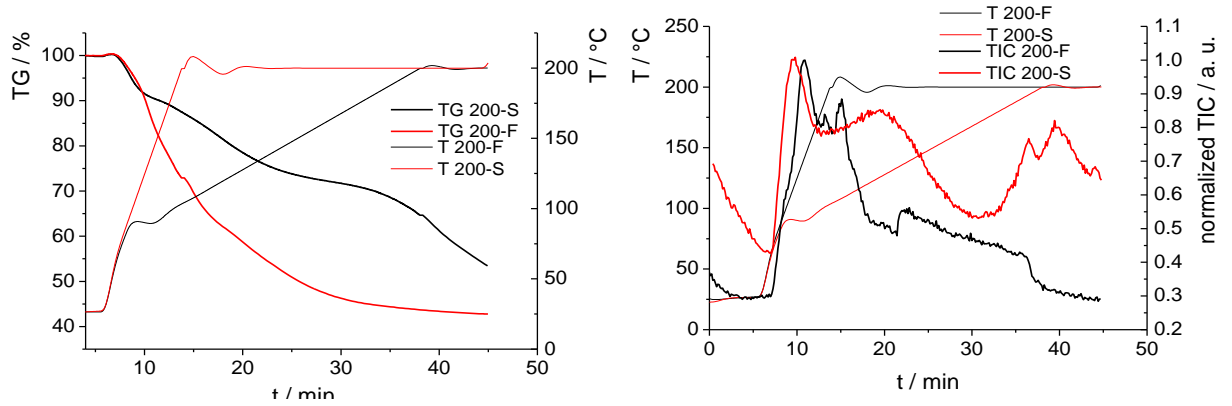


Figure 80: Left side: TG data of active layer samples heated using programs 1 and 2; right side: corresponding TICs

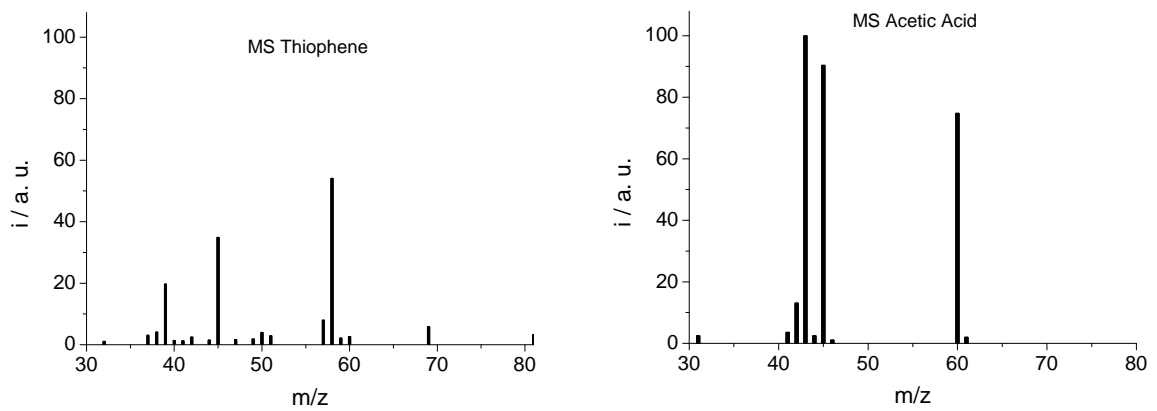


Figure 81: Reference mass spectra of thiophene and acetic acid from $m/z = 30-80$

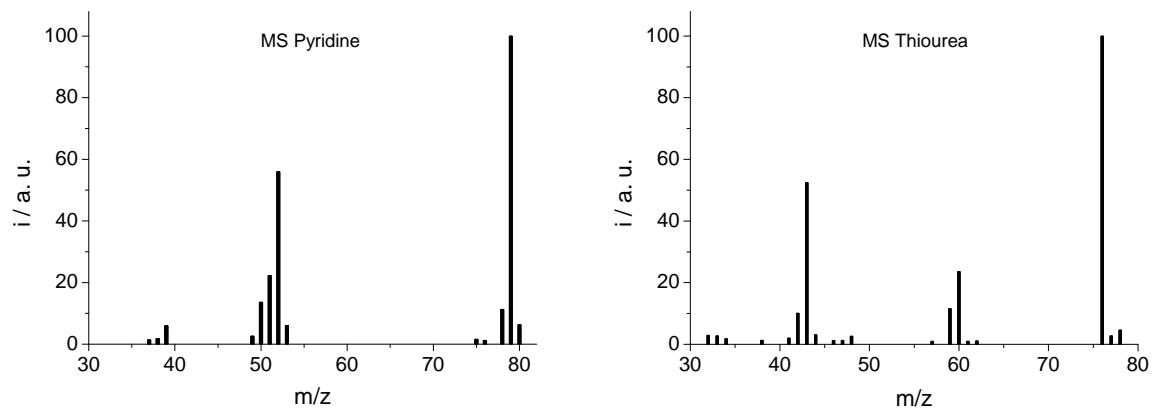


Figure 82: Reference mass spectra of pyridine and thiourea $m/z = 30-80$

10.5 Appendix 10.5: ZCIS-Stoichiometry: i-V Curves

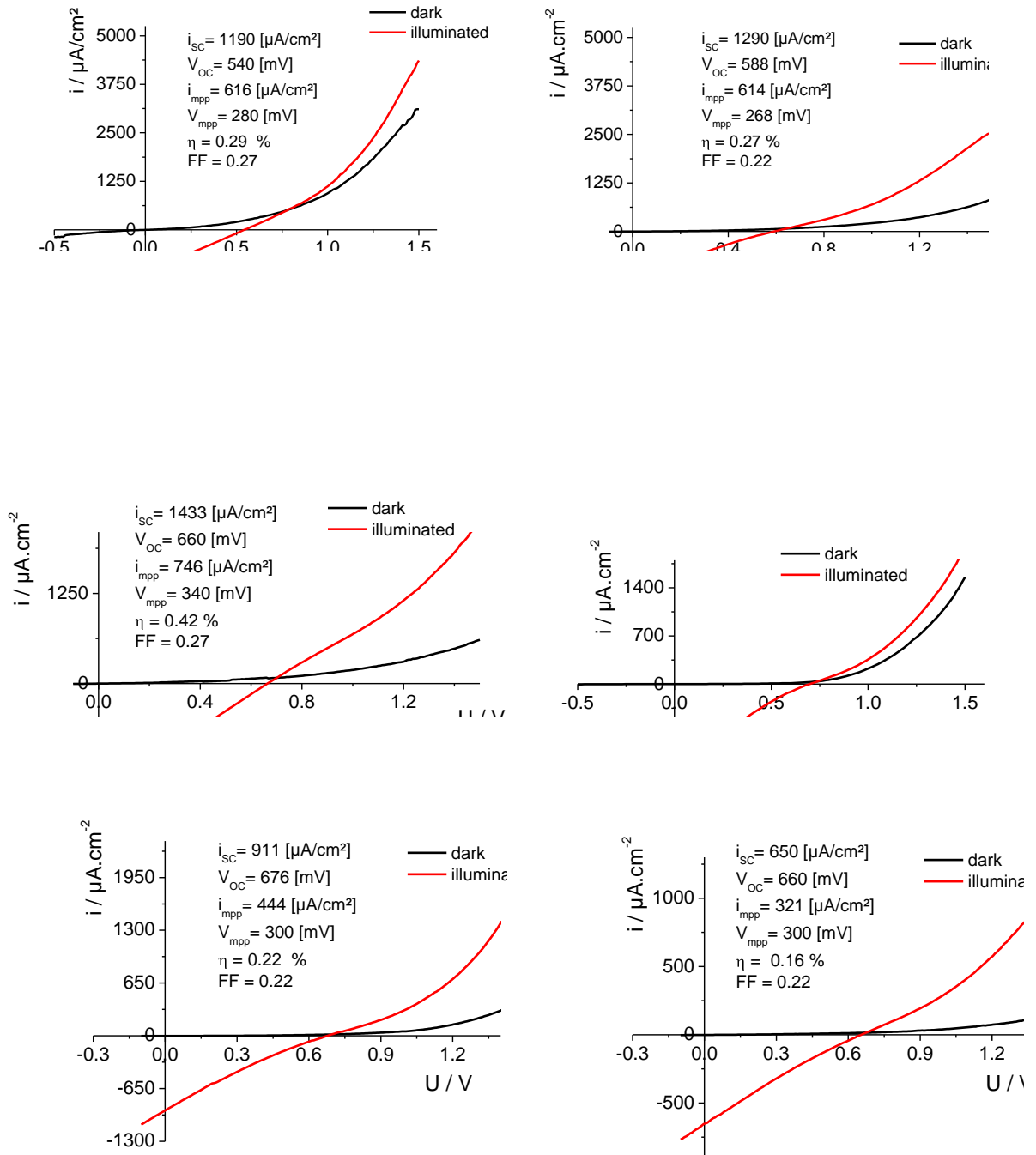


Figure 83: Current density vs. voltage-plots for various P3EBT-ZCIS bulk heterojunction solar cells: top left: [Zn] = 0 (reference), top right: [Zn] = 0.05; middle left: [Zn] = 0.1, middle right: [Zn] = 0.2; bottom left: [Zn] = 0.3, bottom right: [Zn] = 0.5

10.6 Appendix 10.6: EDX-Analyses of P3EBT-ZCIS Active Layers with Different Stoichiometry

NANONA-A: Precursor solution: Cu / In = 1 / 1 (%at.)

Spectrum: 1068

Element	Series	unn. C [wt.-%]	norm. C [wt.-%]	Atom. C [at.-%]
Copper	L-series	34,44	37,99	35,52
Indium	L-series	31,01	34,21	17,70
Sulfur	K-series	18,47	20,38	37,75
Chlorine	K-series	2,69	2,97	4,98
Zinc	L-series	4,03	4,45	4,04
Total:		90,64	100,00	100,00

Spectrum: 1070

Element	Series	unn. C [wt.-%]	norm. C [wt.-%]	Atom. C [at.-%]
Copper	L-series	32,69	34,63	32,39
Indium	L-series	34,74	36,80	19,05
Sulfur	K-series	20,02	21,21	39,32
Chlorine	K-series	3,13	3,32	5,56
Zinc	L-series	3,82	4,04	3,68
Total:		94,39	100,00	100,00

Spectrum: 1071

Element	Series	unn. C [wt.-%]	norm. C [wt.-%]	Atom. C [at.-%]
Copper	L-series	34,04	36,52	34,19
Indium	L-series	32,89	35,28	18,28
Sulfur	K-series	19,20	20,60	38,22
Chlorine	K-series	2,90	3,11	5,22
Zinc	L-series	4,19	4,49	4,09
Total:		93,22	100,00	100,00

NANONA-B: Precursor solution: Cu / In = 1 / 1.25 (%at.)

Spectrum: 1065

Element	Series	unn. C [wt.-%]	norm. C [wt.-%]	Atom. C [at.-%]
Copper	L-series	30,19	30,46	28,21
Indium	L-series	39,01	39,36	20,17
Sulfur	K-series	23,05	23,26	42,67
Chlorine	K-series	3,55	3,59	5,95
Zinc	L-series	3,30	3,33	3,00
Total:		99,11	100,00	100,00

Spectrum: 1067

Element	Series	unn. C [wt.-%]	norm. C [wt.-%]	Atom. C [at.-%]
Copper	L-series	28,30	29,58	27,64
Indium	L-series	38,97	40,73	21,07
Sulfur	K-series	22,06	23,05	42,70
Chlorine	K-series	3,19	3,34	5,59
Zinc	L-series	3,16	3,30	3,00
Total:		95,68	100,00	100,00

Spectrum: 1072

Element	Series	unn. C [wt.-%]	norm. C [wt.-%]	Atom. C [at.-%]
Copper	L-series	30,25	30,38	28,13
Indium	L-series	39,31	39,48	20,24
Sulfur	K-series	23,20	23,30	42,77
Chlorine	K-series	3,55	3,56	5,91
Zinc	L-series	3,26	3,27	2,95
Total:		99,56	100,00	100,00

NANONA-C: Precursor solution: Cu / In = 1 / 1.50 (%at.)

Spectrum: 1073

Element	Series	unn. C [wt.-%]	norm. C [wt.-%]	Atom. C [at.-%]
Copper	L-series	28,69	29,95	28,68
Indium	L-series	40,27	42,04	22,28
Sulfur	K-series	20,20	21,08	40,02
Chlorine	K-series	3,13	3,26	5,60
Zinc	L-series	3,52	3,67	3,42
Total:		95,80	100,00	100,00

Spectrum: 1074

Element	Series	unn. C [wt.-%]	norm. C [wt.-%]	Atom. C [at.-%]
Copper	L-series	28,11	29,84	28,49
Indium	L-series	39,54	41,98	22,18
Sulfur	K-series	20,14	21,39	40,46
Chlorine	K-series	3,08	3,27	5,60
Zinc	L-series	3,32	3,52	3,27
Total:		94,20	100,00	100,00

NANONA-D: Precursor solution: Cu / In = 1 / 1.70 (%at.)

Spectrum: 1075

Element	Series	unn. C [wt.-%]	norm. C [wt.-%]	Atom. C [at.-%]
Copper	L-series	25,97	27,72	26,61
Indium	L-series	41,45	44,25	23,51
Sulfur	K-series	20,76	22,16	42,16
Chlorine	K-series	2,67	2,85	4,90
Zinc	L-series	2,84	3,03	2,83
Total:		93,69	100,00	100,00

Spectrum: 1076

Element	Series	unn. C [wt.-%]	norm. C [wt.-%]	Atom. C [at.-%]
Copper	L-series	26,76	26,95	25,91
Indium	L-series	44,72	45,04	23,97
Sulfur	K-series	22,26	22,42	42,71
Chlorine	K-series	2,76	2,78	4,79
Zinc	L-series	2,78	2,81	2,62
Total:		99,27	100,00	100,00

NANONA-E: Precursor solution: Cu / In = 1 / 1.80 (%at.)

Spectrum: 1077

Element	Series	unn. C [wt.-%]	norm. C [wt.-%]	Atom. C [at.-%]
Copper	L-series	24,41	25,72	24,95
Indium	L-series	44,02	46,37	24,89
Sulfur	K-series	20,92	22,04	42,36
Chlorine	K-series	2,69	2,83	4,92
Zinc	L-series	2,89	3,05	2,87
Total:		94,93	100,00	100,00

Spectrum: 1079

Element	Series	unn. C [wt.-%]	norm. C [wt.-%]	Atom. C [at.-%]
Copper	L-series	24,94	24,92	23,48
Indium	L-series	45,03	45,00	23,46
Sulfur	K-series	24,31	24,30	45,36
Chlorine	K-series	3,12	3,12	5,27
Zinc	L-series	2,66	2,66	2,43
Total:		100,06	100,00	100,00

Spectrum: 1080

Element	Series	unn. C [wt.-%]	norm. C [wt.-%]	Atom. C [at.-%]
Copper	L-series	25,70	27,74	26,58
Indium	L-series	40,76	43,98	23,33
Sulfur	K-series	20,59	22,21	42,19
Chlorine	K-series	2,64	2,85	4,90
Zinc	L-series	2,99	3,22	3,00
Total:		92,68	100,00	100,00

NANONA-F: Precursor solution: Cu / In = 1 / 2.00 (%at.)

Spectrum: 1084

Element	Series	unn. C [wt.-%]	norm. C [wt.-%]	Atom. C [at.-%]
Copper	L-series	23,05	24,62	23,74
Indium	L-series	44,23	47,25	25,22
Sulfur	K-series	21,66	23,14	44,21
Chlorine	K-series	2,54	2,72	4,70
Zinc	L-series	2,12	2,27	2,13
Total:		93,61	100,00	100,00

Spectrum: 1085

Element	Series	unn. C [wt.-%]	norm. C [wt.-%]	Atom. C [at.-%]
Copper	L-series	22,76	23,23	22,41
Indium	L-series	47,47	48,45	25,87
Sulfur	K-series	23,17	23,65	45,21
Chlorine	K-series	2,63	2,68	4,64
Zinc	L-series	1,96	2,00	1,87
Total:		97,98	100,00	100,00

10.7 Appendix 10.7: Morphology of ZCIS-P3EBT Active Layers with Different Cu / In – morphology

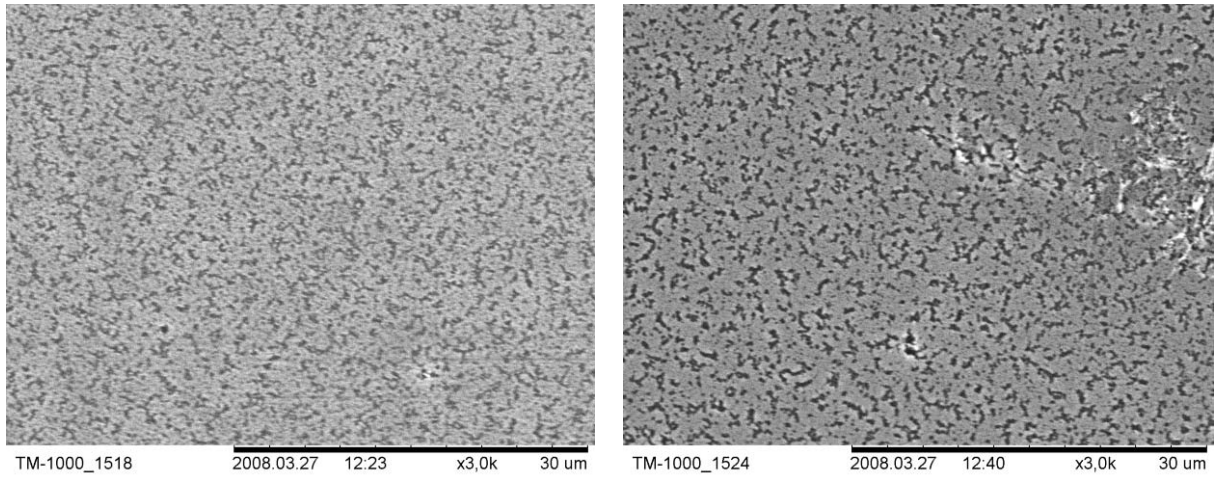


Figure 84: SEM-micrographs of P3EBT-ZCIS active layers; left side: Cu / In = 1 / 1.25 (%at.); right side: Cu / In = 1 / 1.50 (%at.)

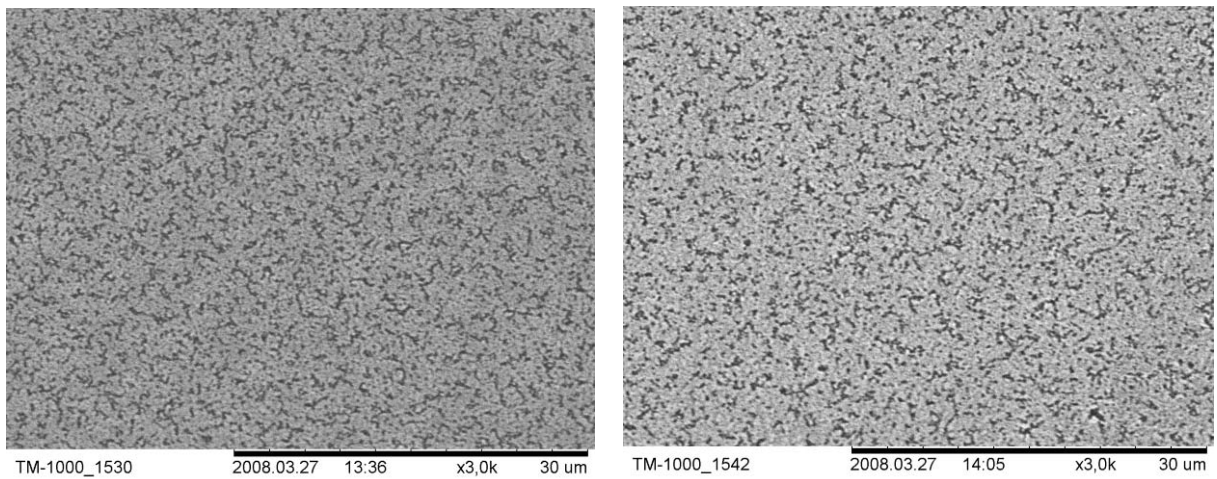


Figure 85: SEM-micrographs of P3EBT-ZCIS active layers; left side: Cu / In = 1 / 1.70 (%at.); right side: Cu / In = 1 / 1.80 (%at.)

10.8 Appendix 10.8: Stability Data of Plastic Solar Cells

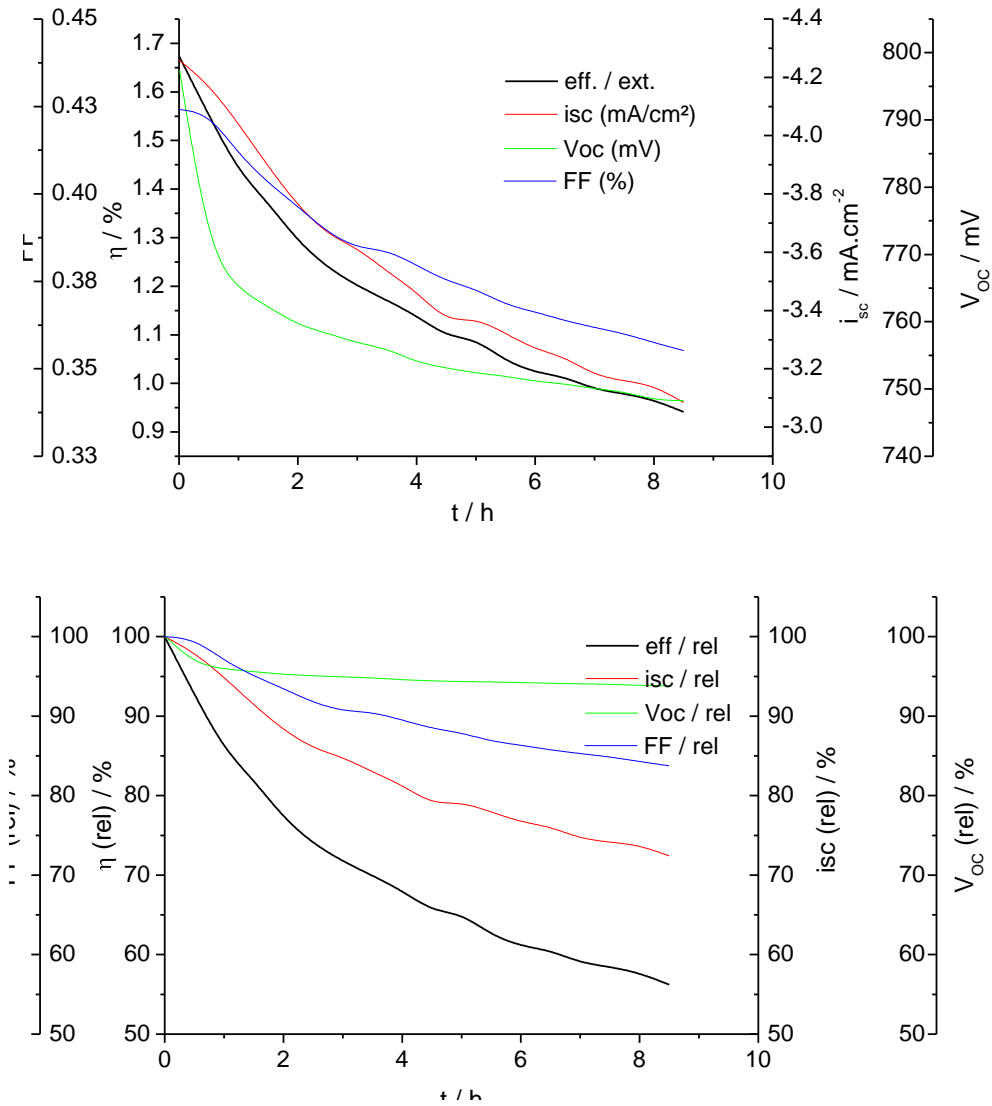


Figure 86: Solar cell parameters of a MEH-PPV - PCBM device under permanent illumination with a sulfur plasma lamp; $P_{(in)} = 1010 \text{ W.m}^{-2}$, no spectral mismatch correction. Top / bottom: absolute / relative values

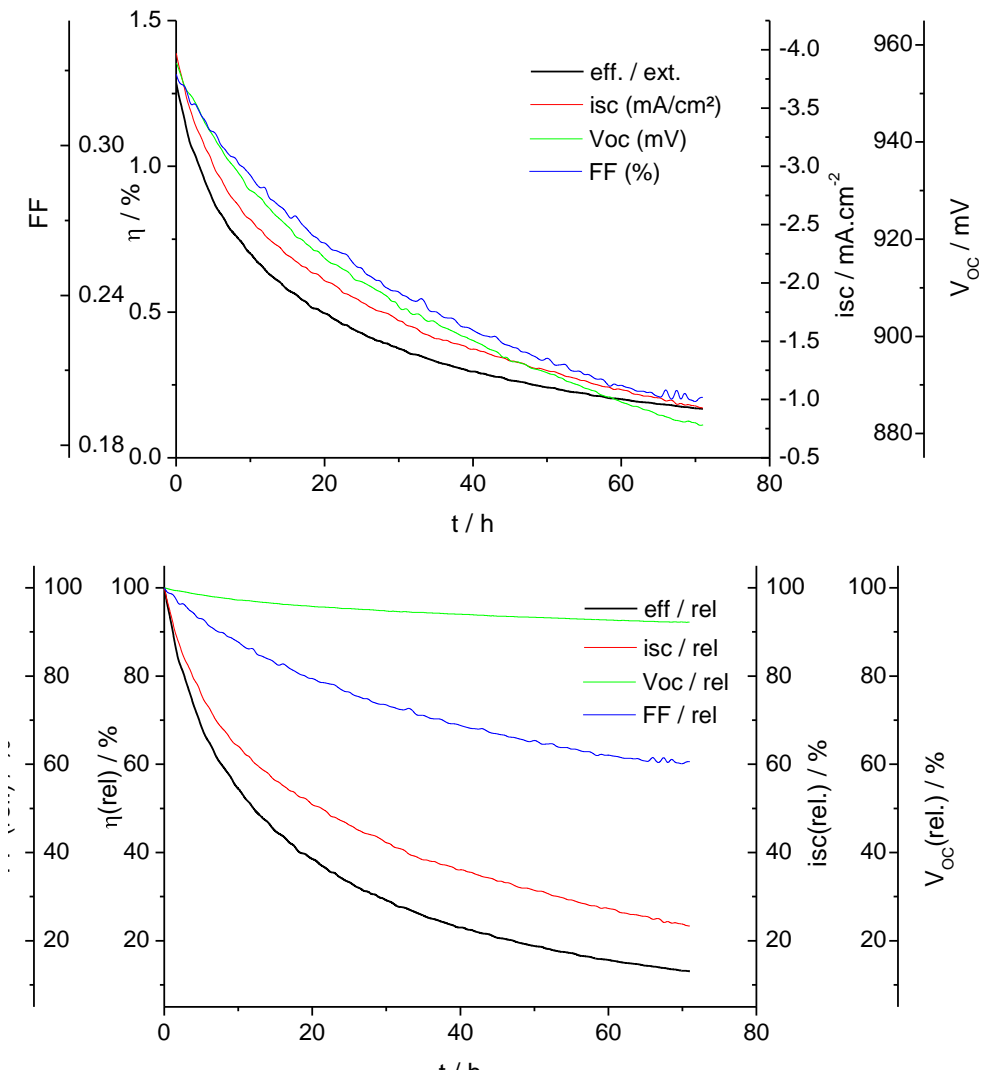


Figure 87: Solar cell parameters of a F8T2 - PCBM device under permanent illumination with a sulfur plasma lamp; $P_{(in)} = 1010 \text{ W.m}^{-2}$, no spectral mismatch correction. Top / bottom: absolute / relative values

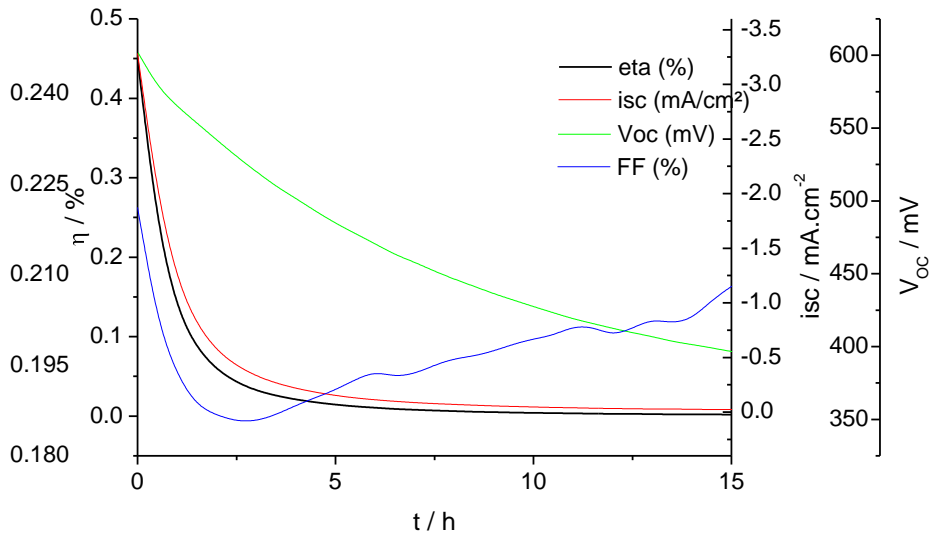


Figure 88: Solar cell parameters of a PPV - CIS device under permanent illumination with a sulfur plasma lamp; $P(\text{in}) = 1010 \text{ W.cm}^{-2}$

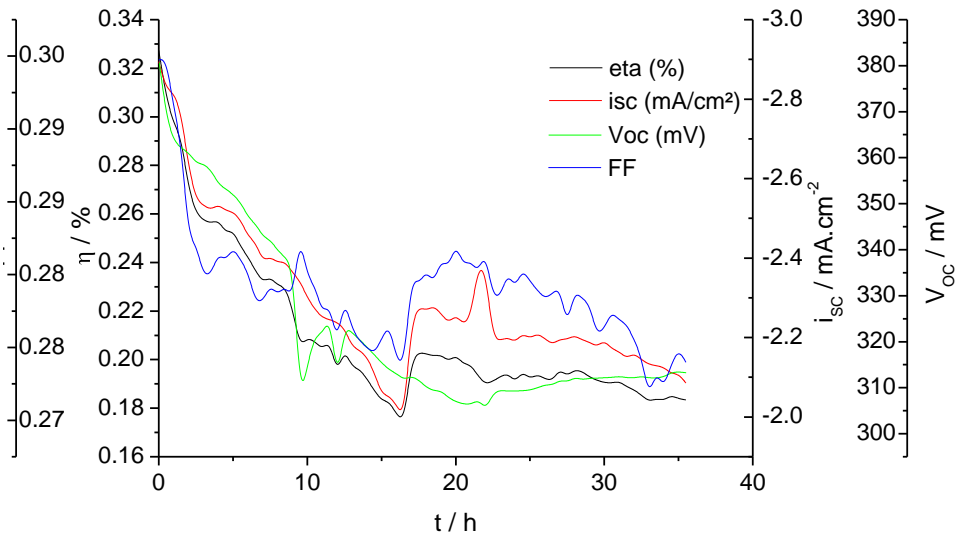


Figure 89: Solar cell parameters of a F8T2 - CIS device under permanent illumination with a sulfur plasma lamp; $P(\text{in}) = 1010 \text{ W.cm}^{-2}$

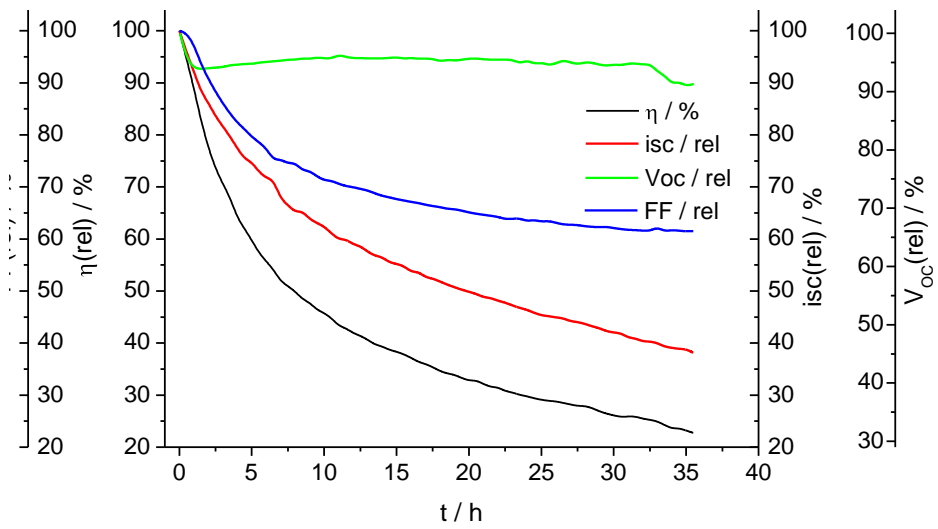
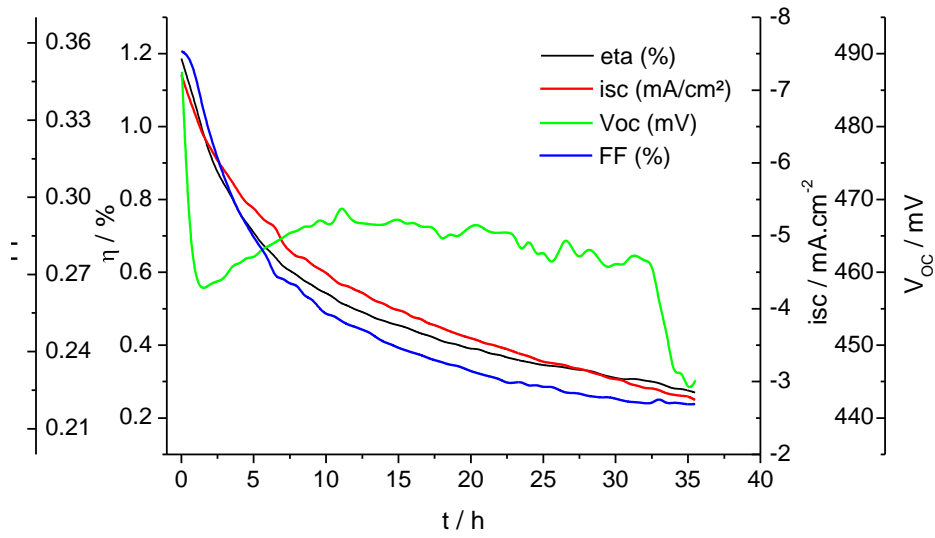


Figure 90: Solar cell parameters of a MEH-PPV - PCBM device under permanent illumination with a sulfur plasma lamp; $P_{(in)} = 1010 \text{ W.m}^{-2}$, no spectral mismatch correction. Top / bottom: absolute / relative values

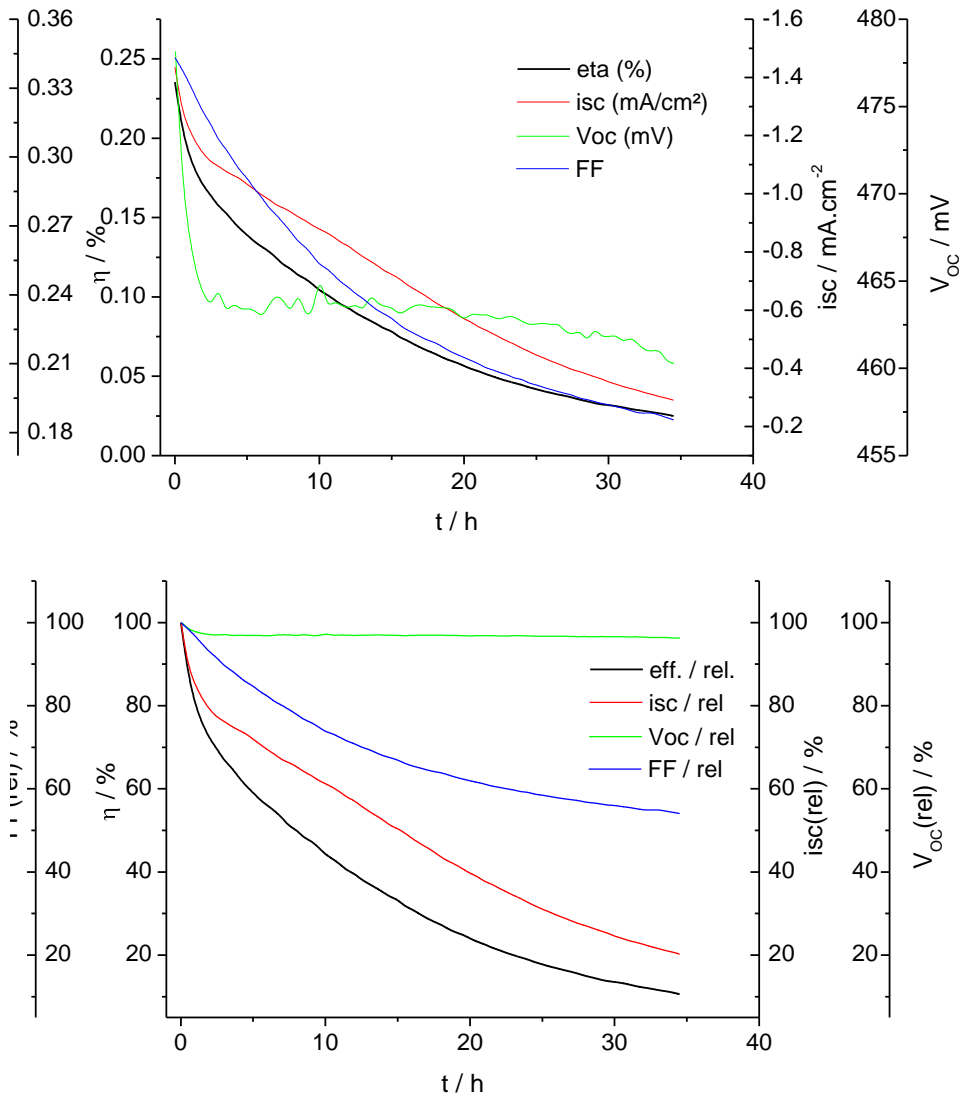


Figure 91: Solar cell parameters of a MDMO-PPV - PCBM device under permanent illumination with a sulfur plasma lamp; $P_{(in)} = 1010 \text{ W.m}^{-2}$, no spectral mismatch correction. Top / bottom: absolute / relative values

11 List of Figures

Figure 1: World energy consumption after region in 1973 (left) and 2007 (right) [2]	1
Figure 2: Left: Global CO ₂ emissions and development scenarios	2
Figure 3: Cumulative PV installation in Germany / worldwide [5]	2
Figure 4: AM1.5G spectrum [27]	6
Figure 5: i-V curve of a solar cell under dark and illuminated conditions.....	8
Figure 6: Scheme of p-n junction formation [49]	9
Figure 7: Band profile formation of two materials of different bandgap, workfunction and electron affinity	10
Figure 8: Schematic drawing of bulk- and bilayer-heterojunction architectures.....	12
Figure 9: Level alignment of a metal – organic semiconductor interface	12
Figure 10: Current generation in organic heterojunction solar cells.....	14
Figure 11: Absorption of photons, thermalization and splitting of the Fermi level [50]	14
Figure 12: i-V curves of MDMO-PPV – PCBM devices with different cathode.....	16
Figure 13: Solar cell with asymmetric contacts at different bias voltages [121]	17
Figure 14: Dark i-V curve of a bulk-heterojunction device in logarithmic scale [77].	18
Figure 15: Structure of PPV, MEH-PPV and MDMO-PPV	19
Figure 16: Left: Polythiophene structures	20
Figure 17: Coupling of 3-substituted thiophene units in different geometries [147]	21

Figure 18: Structures of F8T2 and APFO-3 [154],[17].....	22
Figure 19: Frequently used building blocks of low bandgap polymers	22
Figure 20: C60-PCBM (right side) and cyclovoltammogramm of C70	24
Figure 21: Sphalerite and wurtzite unit cells (Zn: grey, S: yellow).....	25
Figure 22: Chalcopyrite-type unit cell of CuInS ₂ (left) and ternary phase diagram of the Cu-In-S system [194]	27
Figure 23: CIS defect levels determined by Brewster-angle- / photoluminescence spectroscopy [201]	27
Figure 24: Encapsulated hybrid solar cell array	30
Figure 25: Photograph of permanent testing appliance	33
Figure 26: Screenshots of the stability-testing software; right side: operational display containing channel overview and results; left side: parameter settings.....	34
Figure 27: Reaction scheme for metal-sulfide - P3EBT composites	36
Figure 28: Diffraction pattern of P3EBT- CdS composite.....	38
Figure 29: TEM, HR-TEM micrographs and SAED of the P3EBT-CdS composite	39
Figure 30: UV-VIS spectra of different P3EBT-CdS composites	39
Figure 31: i-V curve and surface topography of P3EBT-CdS solar cell.....	40
Figure 32: XRD and TEM-data of P3EBT-PbS composite structures	41
Figure 33: XRD-pattern of the P3EBT-ZnS composite.....	41
Figure 34: TEM, HR-TEM and SAED data for a P3EBT-ZnS composite.....	42

Figure 35: UV-VIS spectra of ZnS-P3EBT composites and i-V curve of a solar cell	43
Figure 36: Thermal generation of PPV from the precursor	45
Figure 37: Energy bands (bulk values) and device structure for PPV-CuInS ₂ solar cells	45
Figure 38: Reaction pathways of TAA in aqueous solution	46
Figure 39: TEM micrographs and SAED of a PPV-CIS composite	47
Figure 40: i-V curves of 1 / 4 (left hand) and 1 / 7 (right hand) PPV-CIS solar cells	49
Figure 41: UV-VIS spectra of PPV-CIS layers and EQE spectrum of a PPV CIS solar cell	50
Figure 42: i-V curves of the reference cell and cell-1	51
Figure 43: i-V curves of cell-2 and cell-3.....	51
Figure 44: XRD data and peak positions of reference data	54
Figure 45: Optical micrographs of CIS-layers on top of a P3EBT-layer	57
Figure 46: i-V curve of a P3EBT-CIS bilayer heterojunction solar cell.....	57
Figure 47: i-V curve and device scheme of a Cu-InCl ₃ -TAA based BHJ device.....	59
Figure 48: i-V curve of CuAc-In(Ac) ₃ -TU based BHJ solar cell	60
Figure 49: i-V curve of a CuCl - In(acac) ₃ – TU based BHJ solar cell.....	61
Figure 50: i-V curve of a Cu(Ac) - InCl ₃ - TU based BHJ solar cell	62
Figure 51: Temperature dependent evolution of the (112) reflection	67
Figure 52: Temperature programs used in TGA experiments.....	68
Figure 53: TG and TIC data of samples heated to 160 °C at different rates	69

Figure 54: Mass spectra of an active-layer sample during heating from RT to 200 °C	70
Figure 55: Selected normalized ion currents during the annealing reaction of an active layer sample.....	70
Figure 56: Screenshot from the analysis of the peak at $m/z = 126$	72
Figure 57: Schematic illustration of the formation of melamine from thiourea.....	72
Figure 58: Melamine (top) and total ion current (bottom) during the course of the measurement	73
Figure 59: FT-IR spectra of P3EBT-layers annealed at various temperatures T_f	74
Figure 60: I-V curves of a P3EBT-CIS device (left) and a P3EBT-ZCIS device.....	78
Figure 61: i-V curves of a P3EBT-CIS- (left side) and a P3EBT-ZCIS device	79
Figure 62: SEM-micrographs of two active layers	80
Figure 63: SEM view on the cross section of a P3EBT-ZCIS active layer	81
Figure 64: Active layer composition vs. precursor composition	82
Figure 65: Solar cell parameters of a P3HT-PCBM device under permanent illumination with a sulfur plasma lamp	85
Figure 66: Relative PCE and i_{SC} values as a function of time for the three polymer – PCBM systems	87
Figure 67: Device parameters of PPV-CIS solar cell.....	88
Figure 68: Relative solar cell parameters of a F8T2 – CIS solar cell.....	89
Figure 69: Relative efficiency values for the four different polymer – $CuInS_2$ systems.....	90

Figure 70: TEM-micrographs and SAED data (inset) for the CdS-P3EBT (left) and for the ZnS-P3EBT composite (right)	91
Figure 71: View on the cross section of a P3EBT-ZCIS active layer on top of a glass-ITO substrate	93
Figure 72: Illumination unit of the stability testing setup in action	94
Figure 73: GPC chromatogram of P3EBT (CHCl ₃ solution, PS calibration).....	97
Figure 74: Cyclovoltammogram of a P3EBT layer on Pt (acetonitrile-TEABF electrolyte, calibration with Fe(cp) ₂).....	97
Figure 75: I-V curves from section 7.5.....	98
Figure 76: i-V curves from section 7.6.6.....	99
Figure 77: i-V curves of differently annealed samples	99
Figure 78: : i-V curves of differently annealed samples	100
Figure 79: Left side: TG- and TIC-data for the decomposition of thiourea	101
Figure 80: Left side: TG data of active layer samples heated using programs 1 and 2	101
Figure 81: Reference mass spectra of thiophene and acetic acid from m/z = 30-80.....	102
Figure 82: Reference mass spectra of pyridine and thiourea m/z = 30-80	102
Figure 83: Current density vs. voltage-plots for various P3EBT-ZCIS bulk heterojunction solar cells	103
Figure 84: SEM-micrographs of P3EBT-ZCIS active layers.....	110
Figure 85: SEM-micrographs of P3EBT-ZCIS active layers.....	110

Figure 86: Solar cell parameters of a MEH-PPV - PCBM device under permanent illumination with a sulfur plasma lamp	111
Figure 87: Solar cell parameters of a F8T2 - PCBM device under permanent illumination with a sulfur plasma lamp	112
Figure 88: Solar cell parameters of a PPV - CIS device under permanent illumination with a sulfur plasma lamp	113
Figure 89: Solar cell parameters of a F8T2 - CIS device under permanent illumination with a sulfur plasma lamp	113
Figure 90: Solar cell parameters of a MEH-PPV - PCBM device under permanent illumination with a sulfur plasma lamp	114
Figure 91: Solar cell parameters of a MDMO-PPV - PCBM device under permanent illumination with a sulfur plasma lamp	115

12 List of Tables

Table 1: Current use and potential of renewable energy forms [3]	1
Table 2: Integrated current at various wavelengths in the AM1.5G spectrum	7
Table 3: Typical properties of singlet excitons in conjugated polymers	11
Table 4: Parameters for selected conjugated polymers.....	23
Table 5: List of chemicals	35
Table 6: Concentrations and proportions of the precursor solutions	37
Table 7: Compositions of PPV-CIS precursor solution	46
Table 8: SAED reflection list of a PPV-CIS blend	48
Table 9: solar cell parameters.....	51
Table 10: Components and concentrations of precursor solution	53
Table 11: Composition of the precursor solutions	55
Table 12: Solar cell efficiencies with different acceptor layer stoichiometries	56
Table 13: Composition of precursor solution	58
Table 14: Composition of precursor solution	59
Table 15: Composition of the precursor solution	61
Table 16: Composition of the precursor solution	61
Table 17: Summarized solar cell parameters for different precursor systems	62
Table 18: Solar cell parameters from different donor acceptor concentrations	65

Table 19: Composition and relative amounts of the precursor solution.....	68
Table 20: Peak area of P3EBT layer at various temperatures	74
Table 21: Overview of heating programs used	75
Table 22: Solar cell parameters.....	76
Table 23: Composition of ZCIS precursor solutions	78
Table 24: Solar cell parameters of P3EBT-ZCIS devices with different stoichiometry	79
Table 25: Production parameters of polymer – PCBM devices	85
Table 26: Stability of polymer – PCBM solar cells.....	86
Table 27: Stability data for CIS - polymer solar cells.....	88

13 Abbreviations

Å	Angström
a, b, c	lattice constants
a.u.	arbitrary units
AM	air mass
CIS	copper indium disulfide
CRT	cathode ray tube
CV	cyclic voltammetry
CZTS	copper zinc tin sulfide
D_i	carrier diffusion coefficient
EDX	energy dispersive X-ray spectroscopy
EQE	external quantum efficiency
E_g	band gap
e	electrons
eq.	equivalents
eV	electron volt
FF	fill factor
FO	frontier orbital
FTIR	fourier transform infrared (spectroscopy)
HMDST	hexamethyldisilathiane
HOMO	highest occupied molecular orbital
I, i	current, current density

I_{mpp}	current at the maximum power point
I_{sc}	short circuit current
IQE	internal quantum efficiency
LED	light emitting diode
ITO	indium tin oxide
JCPDS	Joint Committee on Powder Diffraction Standards
k	Boltzmann constant
LED	light emitting diode
LUMO	lowest unoccupied molecular orbital
μ	carrier mobility
M	spectral mismatch factor
MDMO-PPV	Poly[2-methoxy-5-(3',7'-dimethyloctyloxy)-1,4-phenylenevinylene]
MEH-PPV	Poly[2-methoxy-5-(2'-ethylhexyloxy)-1,4-phenylenevinylene]
n.e.	not estimated
n.s.	not specified
p	hole
P3EBT	poly(3-ethylbutanoate)thiophene
P3HT	poly(3-hexylthiophene)
p.a.	pro analysi
PCBM	[6,6]-Phenyl C61 butyric acid methyl ester
PCPDTBT	Poly[2,6-(4,4-bis-(2-ethylhexyl)-4H-cyclopenta[2,1-b;3,4-b]-dithiophene)-alt-4,7-(2,1,3-benzothiadiazole)]
PDF	powder diffraction file

PEDOT:PSS	Poly(3,4-ethylenedioxythiophene) : poly(styrenesulfonate)
PF	polyfluorene
P_{IN}	incident light intensity
PLED	polymer light emitting diode
mpp	maximum power point
OLED	organic light emitting diode
r	distance
SEM	scanning electron microscopy
SR	spectral responsivity
T	temperature
TAA	thioacetamide
TEM	transmission electron microscopy
TU	thiourea
V	voltage
V_{mpp}	voltage at the maximum power point
V_{oc}	open circuit voltage
XRD	X-ray diffraction
η	efficiency
θ	reflection angle (X-ray diffraction)
λ	wavelength
Ω	resistance
ZCIS	$ZnS_{2x} \cdot (CuIn)_{1-x}S_2$

14 Bibliography

- [1] J. Goldemberg und T.B. Johansson, Hrsg., *World Energy Assessment, 2004 Update*, UNO, United Nations Development Programme (UNDP), 2004.
- [2] I.E.A. (IEA), *Key World Energy Statistics 2009*, International Energy Agency (IEA), 2009.
- [3] U.N.D.P. (UNDP), *World Energy Assessment*, United Nations Development Programme (UNDP), 2000.
- [4] A.R. Rajendra K. Pachauri, Hrsg., *Climate Change 2007 Synthesis Report*, Intergovernmental Panel on Climate Change (IPCC), 2008.
- [5] R. Bhandari und I. Stadler, "Grid parity analysis of solar photovoltaic systems in Germany using experience curves," *Sol. Ener.*, 83, 2009, S. 1634 - 1644.
- [6] C.W. Tang, "Two-layer organic photovoltaic cell," *Appl. Phys. Lett.*, 48, 1986, S. 183-185.
- [7] H. Kallmann und M. Pope, "Photovoltaic Effect in Organic Crystals," *Jour. Chem. Phys.*, 30, 1959, S. 585-586.
- [8] H. W. Kroto, J. R. Heath, S. C. O'Brien, R. F. Curl, R. E. Smalley, "C60: Buckminsterfullerene," *Nature*, 318, 1985, S. 162-63.
- [9] N.S. Sariciftci, L. Smilowitz, A.J. Heeger, und F. Wudl, "Photoinduced Electron Transfer from a Conducting Polymer to Buckminsterfullerene," *Science*, 258, 1992, S. 1474-1476.
- [10] B.R. Saunders und M.L. Turner, "Nanoparticle-polymer photovoltaic cells," *Adv. Colloid Interface Sci.*, 138, 2008, S. 1-23.
- [11] B. Sun, E. Marx, und N.C. Greenham, "Photovoltaic Devices Using Blends of Branched CdSe Nanoparticles and Conjugated Polymers," *Nano Lett.*, 3, 2003, S. 961-963.
- [12] W.U. Huynh, J.J. Dittmer, und A.P. Alivisatos, "Hybrid Nanorod-Polymer Solar Cells," *Science*, 295, 2002, S. 2425-2427.
- [13] P. Wang, A. Abrusci, H.M.P. Wong, M. Svensson, M.R. Andersson, und N.C. Greenham, "Photoinduced Charge Transfer and Efficient Solar Energy Conversion in a Blend of a Red Polyfluorene Copolymer with CdSe Nanoparticles," *Nano Lett.*, 6, 2006, S. 1789-1793.

- [14] L. Manna, E.C. Scher, und A.P. Alivisatos, "Synthesis of Soluble and Processable Rod-, Arrow-, Teardrop-, and Tetrapod-Shaped CdSe Nanocrystals," *J. Am. Chem. Soc.*, 122, 2000, S. 12700–12706.
- [15] Y. Kang und D. Kim, "Well-aligned CdS nanorod/conjugated polymer solar cells," *Sol. Energy Mater. Sol. Cells*, 90, 2006, S. 166 -174.
- [16] I. Gur, N.A. Fromer, und A.P. Alivisatos, "Controlled Assembly of Hybrid Bulk-Heterojunction Solar Cells by Sequential Deposition," *J. Phys. Chem. B*, 110, 2006, S. 25543–25546.
- [17] P. Ravirajan, S.A. Haque, J.R. Durrant, D. Poplavskyy, D.D.C. Bradley, und J. Nelson, "Hybrid nanocrystalline TiO₂ solar cells with a fluorene--thiophene copolymer as a sensitizer and hole conductor," *J. Appl. Phys.*, 95, 2004, S. 1473-1480.
- [18] P.R. Johann Bouclé und J. Nelson, "Hybrid polymer/metal oxide thin films for photovoltaic applications," *J. Mater. Chem.*, 14, 2007, S. 3141-53.
- [19] W. Beek, M. Wienk, M. Kemerink, X. Yang, und R. Janssen, "Hybrid Zinc Oxide Conjugated Polymer Bulk Heterojunction Solar Cells," *J. Phys. Chem. B*, 109, 2005, S. 9505-9516.
- [20] B. Sun, H.J. Snaith, A.S. Dhoot, S. Westenhoff, und N.C. Greenham, "Vertically segregated hybrid blends for photovoltaic devices with improved efficiency," *J. Appl. Phys.*, 97, 2005, S. 014914.
- [21] S.D. Oosterhout, M.M. Wienk, S.S. van Bavel, R. Thiedmann, L. Jan Anton Koster, J. Gilot, J. Loos, V. Schmidt, und R.A.J. Janssen, "The effect of three-dimensional morphology on the efficiency of hybrid polymer solar cells," *Nat. Mater.*, 8, 2009, S. 818-824.
- [22] H. Liao, S. Chen, und D. Liu, "In-Situ Growing CdS Single-Crystal Nanorods via P3HT Polymer as a Soft Template for Enhancing Photovoltaic Performance," *Macromolecules*, 42, 2009, S. 6558-6563.
- [23] M. Piber, "Neue Konzepte zur Herstellung von Nanocompositesolarzellen basierend auf anorganischen sulfidischen Halbleitern und Polyphenylenvinylenen," Graz Technical University, 2006.
- [24] M. Edler, Graz Technical University, 2011.
- [25] A. Fischereder, Graz Technical University, 2011.
- [26] H.E. Wagemann, *Photovoltaik*, Vieweg&Teubner, 2007.
- [27] <http://rredc.nrel.gov/solar/spectra/am1.5/>, accessed on 11.5.2010.

- [28] P. Würfel, "Thermodynamic limitations to solar energy conversion," *Physica E*, 14, 2002, S. 18-26.
- [29] W. Shockley und H.J. Queisser, "Detailed Balance Limit of Efficiency of p-n Junction Solar Cells," *J. Appl. Phys.*, 32, 1961, S. 510-519.
- [30] C.D. Mathers, "Upper limit of efficiency for photovoltaic solar cells," *J. Appl. Phys.*, 48, 1977, S. 3181-3182.
- [31] M.A. Green, K. Emery, Y. Hishikawa, und W. Warta, "Solar cell efficiency tables (Version 34)," *Progress in Photovoltaics: Research and Applications*, 17, 2009, S. 320-326.
- [32] G. Dennler, M.C. Scharber, und C.J. Brabec, "Polymer-Fullerene Bulk-Heterojunction Solar Cells," *Adv. Mater.*, 21, 2009, S. 1323-1338.
- [33] Y. Liang, Z. Xu, J. Xia, S. Tsai, Y. Wu, G. Li, C. Ray, und L. Yu, "For the Bright Future-Bulk Heterojunction Polymer Solar Cells with Power Conversion Efficiency of 7.4%," *Adv. Mater.*, doi: 10.1002/adma.200903528, 2010, S. NA.
- [34] S. Dayal, N. Kopidakis, D.C. Olson, D.S. Ginley, und G. Rumbles, "Photovoltaic Devices with a Low Band Gap Polymer and CdSe Nanostructures Exceeding 3% Efficiency," *Nano Lett.*, 10, 2010, S. 239-242.
- [35] A. Luque, *Handbook of photovoltaic science and engineering*, Wiley, 2003.
- [36] "ASTM E948, Standard Test Method for Electrical Performance of Non-Concentrator Photovoltaic Cells Using Reference Cells."
- [37] "CEC 101, Issue 2, EUR-7078 EN, Standard Procedures for Terrestrial Photovoltaic Measurements."
- [38] "Standard IEC 60904-1, Photovoltaic Devices Part 1: Measurement of Photovoltaic Current-Voltage Characteristics."
- [39] "Standard IEC 60904-3, Measurement Principles for Terrestrial PV Solar Devices with Reference Spectral Irradiance Data."
- [40] V. Shrotriya, G. Li, Y. Yao, T. Moriarty, K. Emery, und Y. Yang, "Accurate Measurement and Characterization of Organic Solar Cells," *Adv. Funct. Mater.*, 16, 2006, S. 2016-2023.
- [41] J.M. Kroon, M.M. Wienk, W.J.H. Verhees, und J.C. Hummelen, "Accurate efficiency determination and stability studies of conjugated polymer/fullerene solar cells," *Thin Solid Films*, 403-404, 2002, S. 223-228.

- [42] N. Koide, Y. Chiba, and L. Han, "Methods of Measuring Energy Conversion Efficiency in Dye-sensitized Solar Cells," *Jpn. J. Appl. Phys.*, 44, 2005, S. 4176-4181.
- [43] A. Cravino, P. Schilinsky, and C. Brabec, "Characterization of Organic Solar Cells: the Importance of Device Layout," *Adv. Funct. Mater.*, 17, 2007, S. 3906-3910.
- [44] M.Y. Chan, S.L. Lai, M.K. Fung, C.S. Lee, and S.T. Lee, "Doping-induced efficiency enhancement in organic photovoltaic devices," *Appl. Phys. Lett.*, 90, 2007, S. 023504.
- [45] K. Kim, J. Liu, M.A.G. Namboothiry, and D.L. Carroll, "Roles of donor and acceptor nanodomains in 6% efficient thermally annealed polymer photovoltaics," *Applied Physics Letters*, 90, 2007, S. 163511.
- [46] G. Dennler, "The value of values," *Mater. Today*, 10, 2007, S. 56 -56.
- [47] J.W. Gilot, "On the efficiency of Polymer Solar Cells," *Nat. Mater.*, 6, 2007, S. 704-705.
- [48] G.P. Smestad, F.C. Krebs, C.M. Lampert, C.G. Granqvist, K. Chopra, X. Mathew, und H. Takakura, "Reporting solar cell efficiencies in Solar Energy Materials and Solar Cells," *Sol. Energy Mater. Sol. Cells*, 92, 2008, S. 371 -373.
- [49] J.S. Umesh K. Mishra, *Semiconductor Device Physics and Design*, Springer, 2008.
- [50] P. Würfel, *Physics of solar cells*, Wiley-VCH Verl., 2005.
- [51] S.M.;N. Sze, *Physics of Semiconductor Devices*, Wiley, 2006.
- [52] C.K. Chiang, C.R. Fincher, Y.W. Park, A.J. Heeger, H. Shirakawa, E.J. Louis, S.C. Gau, und A.G. MacDiarmid, "Electrical Conductivity in Doped Polyacetylene," *Phys. Rev. Lett.*, 39, 1977, S. 1098.
- [53] M. Schwoerer, *Organische molekulare Festkörper*, Weinheim: Wiley-VCH, 2005.
- [54] V. Coropceanu, J. Cornil, D. daSilvaFilho, Y. Olivier, R. Silbey, und J. Bredas, "Charge Transport in Organic Semiconductors," *Chem. Rev.*, 107, 2007, S. 926-952.
- [55] J.J.M. Halls, K. Pichler, R.H. Friend, S.C. Moratti, und A.B. Holmes, "Exciton diffusion and dissociation in a poly(p-phenylenevinylene)/C[₆₀] heterojunction photovoltaic cell," *App.Phys.Lett.*, 68, 1996, S. 3120-3122.
- [56] R.R. Lunt, J.B. Benziger, und S.R. Forrest, "Relationship between Crystalline Order and Exciton Diffusion Length in Molecular Organic Semiconductors," *Adv. Mater.*, 22, 2009, S. 1233 - 1236.

- [57] A. Köhler und H. Bässler, "Triplet states in organic semiconductors," *Mater. Sci. Eng., R*, 66, 2009, S. 71-109.
- [58] X. Yang, C. Lee, S. Westenhoff, X. Zhang, und N.C. Greenham, "Saturation, Relaxation, and Dissociation of Excited Triplet Excitons in Conjugated Polymers," *Adv. Mater.*, 21, 2009, S. 916–919.
- [59] I.A. Howard, J.M. Hodgkiss, X. Zhang, K.R. Kirov, H.A. Bronstein, C.K. Williams, R.H. Friend, S. Westenhoff, und N.C. Greenham, "Charge Recombination and Exciton Annihilation Reactions in Conjugated Polymer Blends," *Jour. Am. Chem. Soc.*, 132, 2010, S. 328–335.
- [60] S.S. D.C. Olson, "Band-Offset Engineering for Enhanced Open-Circuit Voltage in Polymer-Oxide Hybrid Solar Cells," *Adv. Funct. Mater.*, 17, 2007, S. 264-269.
- [61] D. Veldman, S.C.J. Meskers, und R.A.J. Janssen, "The Energy of Charge-Transfer States in Electron Donor-Acceptor Blends: Insight into the Energy Losses in Organic Solar Cells," *Adv. Funct. Mater.*, 19, 2009, S. 1939-1948.
- [62] S. Sun, "Optimum energy levels and offsets for organic donor/acceptor binary photovoltaic materials and solar cells," *Mater. Sci. Eng., B*, 116, 2005, S. 251 -256.
- [63] C.J. Brabec, A. Cravino, D. Meissner, N.S. Sariciftci, T. Fromherz, M.T. Rispens, L. Sanchez, und J.C. Hummelen, "Origin of the Open Circuit Voltage of Plastic Solar Cells," *Adv. Funct. Mater.*, 11, 2001, S. 374-380.
- [64] L.C. Chen, D. Godovsky, O. Inganäs, J.C. Hummelen, R.A.J. Janssen, M. Svensson, und M.R. Andersson, "Polymer Photovoltaic Devices from Stratified Multilayers of Donor-Acceptor Blends," *Adv. Mater.*, 12, 2000, S. 1367–1370.
- [65] M. Granstrom, K. Petritsch, A.C. Arias, A. Lux, M.R. Andersson, und R.H. Friend, "Laminated fabrication of polymeric photovoltaic diodes," *Nature*, 395, 1998, S. 257–260.
- [66] K.S. Hisao Ishii, "Energy Level Alignment and Interfacial Electronic Structures at Organic/Metal and Organic/Organic Interfaces," *Adv. Mater.*, 11, 1999, S. 605-625.
- [67] C. Chen, T. Tien, B. Ko, Y. Chen, und C. Ting, "Energy Level Alignment at the Anode of Poly(3-hexylthiophene)/Fullerene-Based Solar Cells," *ACS App. Mater. Interfaces*, 1, 2009, S. 741–745.
- [68] F. Zhang, A. Vollmer, J. Zhang, Z. Xu, J. Rabe, und N. Koch, "Energy level alignment and morphology of interfaces between molecular and polymeric organic semiconductors," *Org. Electron.*, 8, 2007, S. 606 - 614.
- [69] C. Chen, T. Tien, B. Ko, Y. Chen, und C. Ting, "Energy Level Alignment at the Anode of Poly(3-hexylthiophene)/Fullerene-Based Solar Cells," *ACS Applied Materials & Interfaces*, 0, 2009.

- [70] N.R. Armstrong, P.A. Veneman, E. Ratcliff, D. Placencia, und M. Brumbach, "Oxide Contacts in Organic Photovoltaics: Characterization and Control of Near-Surface Composition in Indium-Tin Oxide (ITO) Electrodes," *Acc. Chem. Res.*, 42, 2009, S. 1748-1757.
- [71] J. Ivanco und D.R.T. Zahn, "Critical evaluation of band bending determination in organic films from photoemission measurements," *J. Vac. Sci. Technol., A*, 27, 2009, S. 1178-1182.
- [72] I.G. Hill, A.J. Makinen, und Z.H. Kafafi, "Distinguishing between interface dipoles and band bending at metal/tris-(8-hydroxyquinoline) aluminum interfaces," *Appl. Phys. Lett.*, 77, 2000, S. 1825-1827.
- [73] C.J.S. Brabec, "Plastic Solar Cells," *Adv. Funct. Mater.*, 11, 2001, S. 15-26.
- [74] M. Gruber, "Investigation of morphology effects on the performance of organic solar cells and hybrid cells by two-dimensional drift-diffusion simulations," Graz Technical University, 2009.
- [75] B. Stickler, "Theoretical Investigation of the Competition between Electron-Hole Generation and Recombination Effects in Organic and Organic-Inorganic Solar Cells," Graz Technical University, 2009.
- [76] V.M. P.W.M. Blom, "Device Physics of Polymer:Fullerene Bulk Heterojunction Solar Cells," *Adv. Mater.*, 19, 2007, S. 1551-1566.
- [77] C.J. Brabec, *Organic photovoltaics*, Springer, 2003.
- [78] S. Sun, *Organic photovoltaics*, Taylor & Francis, 2005.
- [79] M. Hallermann, I. Kriegel, E.D. Como, J.M. Berger, E. von Hauff, und J. Feldmann, "Charge Transfer Excitons in Polymer/Fullerene Blends: The Role of Morphology and Polymer Chain Conformation," *Adv. Funct. Mater.*, 19, 2009, S. 3662-3668.
- [80] V.D. Mihailetschi, L.J.A. Koster, J.C. Hummelen, und P.W.M. Blom, "Photocurrent Generation in Polymer-Fullerene Bulk Heterojunctions," *Phys. Rev. Lett.*, 93, 2004.
- [81] C.L. Braun, "Electric field assisted dissociation of charge transfer states as a mechanism of photocarrier production," *The Journal of Chemical Physics*, 80, 1984, S. 4157-4161.
- [82] D. Hertel, E.V. Soh, H. Bässler, und L.J. Rothberg, "Electric field dependent generation of geminate electron-hole pairs in a ladder-type [pi]-conjugated polymer probed by fluorescence quenching and delayed field collection of charge carriers," *Chem. Phys. Lett.*, 361, 2002, S. 99 - 105.

- [83] J. Lloyd-Hughes, T. Richards, H. Sirringhaus, M.B. Johnston, and L.M. Herz, "Exciton dissociation in polymer field-effect transistors studied using terahertz spectroscopy," *Physical Review B (Condensed Matter and Materials Physics)*, 77, 2008, S. 125203.
- [84] C.H.;V. Hamann, *Electrochemistry*, Weinheim: Wiley-VCH-Verl., 2007.
- [85] P. Würfel, "Photovoltaic Principles and Organic Solar Cells," *CHIMIA International Journal for Chemistry*, 61, S. 770–774.
- [86] J. Nelson, J.J. Kwiatkowski, J. Kirkpatrick, and J.M. Frost, "Modeling Charge Transport in Organic Photovoltaic Materials," *Acc. Chem. Res.*, 42, 2009, S. 1768-1778.
- [87] J. Nelson, S.A. Choulis, and J.R. Durrant, "Charge recombination in polymer/fullerene photovoltaic devices," *Thin Solid Films*, 451-452, 2004, S. 508-514.
- [88] I. Montanari, A.F. Nogueira, J. Nelson, J.R. Durrant, C. Winder, M.A. Loi, N.S. Sariciftci, and C. Brabec, "Transient optical studies of charge recombination dynamics in a polymer/fullerene composite at room temperature," *Appl. Phys. Lett.*, 81, 2002, S. 3001-3003.
- [89] V.D. Mihailetschi, J. Wildeman, and P.W.M. Blom, "Space-Charge Limited Photocurrent," *Phys. Rev. Lett.*, 94, 2005.
- [90] H. Hoppe und N.S. Sariciftci, "Morphology of polymer/fullerene bulk heterojunction solar cells," *J. Mater. Chem.*, 16, 2006, S. 45-61.
- [91] P.A. Troshin, H. Hoppe, J. Renz, M. Egginger, J.Y. Mayorova, A.E. Goryachev, A.S. Peregudov, R.N. Lyubovskaya, G. Gobsch, N.S. Sariciftci, und V.F. Razumov, "Material Solubility-Photovoltaic Performance Relationship in the Design of Novel Fullerene Derivatives for Bulk Heterojunction Solar Cells," *Adv. Funct. Mater.*, 9999, 2009.
- [92] K.J. F. Zhang, "Influence of Solvent Mixing on the Morphology and Performance of Solar Cells Based on Polyfluorene Copolymer/Fullerene Blends," *Adv. Funct. Mater.*, 16, 2006, S. 667-674.
- [93] K.M. A.J. Moule, "Controlling Morphology in Polymer-Fullerene Mixtures," *Adv. Mater.*, 9999, 2007.
- [94] J.H. Yan Yao, "Effects of Solvent Mixtures on the Nanoscale Phase Separation in Polymer Solar Cells," *Adv. Funct. Mater.*, 18, 2008, S. 1783-1789.

- [95] Z. Xu, L. Chen, G. Yang, C. Huang, J. Hou, Y. Wu, G. Li, C. Hsu, and Y. Yang, "Vertical Phase Separation in Poly(3-hexylthiophene): Fullerene Derivative Blends and its Advantage for Inverted Structure Solar Cells," *Adv. Funct. Mater.*, 9999, 2009.
- [96] J. Huang, Z. Ho, D. Kekuda, Y. Chang, C. Chu, and K. Ho, "Effects of nanomorphological changes on the performance of solar cells with blends of poly[9,9'-dioctyl-fluorene-co-bithiophene] and a soluble fullerene," *Nanotechnology*, 20, 2009, S. 025202 (9pp).
- [97] Y.D. Park, H.S. Lee, Y.J. Choi, D. Kwak, J.H. Cho, S. Lee, and K. Cho, "Solubility-Induced Ordered Polythiophene Precursors for High-Performance Organic Thin-Film Transistors," *Adv. Funct. Mater.*, 9999, 2009.
- [98] J. Zhao, A. Swinnen, G. Van Assche, J. Manca, D. Vanderzande, and B.V. Mele, "Phase Diagram of P3HT/PCBM Blends and Its Implication for the Stability of Morphology," *J. Phys. Chem. B*, 0, 2009.
- [99] A.O. Sevim und S. Mutlu, "Post-fabrication electric field and thermal treatment of polymer light emitting diodes and their photovoltaic properties," *Organic Electronics*, 10, 2009, S. 18-26.
- [100] C.Y. Kwong, A.B. Djuricic, P.C. Chui, K.W. Cheng, and W.K. Chan, "Influence of solvent on film morphology and device performance of poly(3-hexylthiophene):TiO₂ nanocomposite solar cells," *Chem. Phys. Lett.*, 384, 2004, S. 372 -375.
- [101] D. Chirvase, J. Parisi, J.C. Hummelen, and V. Dyakonov, "Influence of nanomorphology on the photovoltaic action of polymer–fullerene composites," *Nanotechnology*, 15, 2004, S. 1317-1323.
- [102] H.H. L.H. Nguyen, "Effects of Annealing on the Nanomorphology and Performance of Poly(alkylthiophene):Fullerene Bulk-Heterojunction Solar Cells," *Adv. Funct. Mater.*, 17, 2007, S. 1071-1078.
- [103] J.K. T.J. Savenije, "The Effect of Thermal Treatment on the Morphology and Charge Carrier Dynamics in a Polythiophene-Fullerene Bulk Heterojunction," *Adv. Funct. Mater.*, 15, 2005, S. 1260-1266.
- [104] L. Chen, Z. Hong, G. Li, and Y. Yang, "Recent Progress in Polymer Solar Cells: Manipulation of Polymer:Fullerene Morphology and the Formation of Efficient Inverted Polymer Solar Cells," *Adv. Mater.*, 9999, 2009, S. NA.
- [105] R.R. F. Padinger, "Effects of Postproduction Treatment on Plastic Solar Cells," *Adv. Funct. Mater.*, 13, 2003, S. 85-88.
- [106] C.G. Granqvist, "Transparent conductors as solar energy materials: A panoramic review," *Sol. Energy Mater. Sol. Cells*, 91, 2007, S. 1529–1598.

- [107] M. Fahlman und W. Salaneck, "Surfaces and interfaces in polymer-based electronics," *Surf. Sci.*, 500, 2002, S. 904-922.
- [108] X.G. W. Chen, "Surface-Transfer Doping of Organic Semiconductors Using Functionalized Self-Assembled Monolayers, VL-Shift," *Adv. Funct. Mater.*, 17, 2007, S. 1339-1344.
- [109] X. Cheng, Y. Noh, J. Wang, M. Tello, J. Frisch, R. Blum, A. Vollmer, J.P. Rabe, N. Koch, und H. Sirringhaus, "Controlling Electron and Hole Charge Injection in Ambipolar Organic Field-Effect Transistors by Self-Assembled Monolayers," *Adv. Funct. Mater.*, 19, 2009, S. 2407-2415.
- [110] S. Kirchmeyer und K. Reuter, "Scientific importance, properties and growing applications of poly(3,4-ethylenedioxythiophene)," *J. Mater. Chem.*, 15, 2005, S. 2077 -2088.
- [111] H. Bejbouji, L. Vignau, J.L. Miane, M. Dang, E.M. Oualim, M. Harmouchi, und A. Mouhsen, "Polyaniline as a hole injection layer on organic photovoltaic cells," *Sol. Energy Mater. Sol. Cells*, 94, 2010, S. 176 - 181.
- [112] N.A.Z. R. W. T. Higgins, "Emeraldine Base Polyaniline as an Alternative to Poly(3,4-ethylenedioxythiophene) as a Hole-Transporting Layer," *Adv. Funct. Mater.*, 11, 2001, S. 407-412.
- [113] B.H. Lee, H.C. Back, S.H. Park, und K. Lee, "Flexible polymer electronic devices using highly conductive polyaniline electrode," *Organic Photovoltaics X*, Z.H. Kafafi und P.A. Lane, Hrsg., SPIE, 2009, S. 74161F.
- [114] www.clevios.com, "accessed on 2010-05-16."
- [115] M.J. F. Zhang, "Polymer Photovoltaic Cells with Conducting Polymer Anodes," *Adv. Mater.*, 14, 2002, S. 662-665.
- [116] T. Ameri, G. Dennler, C. Waldauf, P. Denk, K. Forberich, M.C. Scharber, C.J. Brabec, und K. Hingerl, "Realization, characterization, and optical modeling of inverted bulk-heterojunction organic solar cells," *J. Appl. Phys.*, 103, 2008.
- [117] V.D. Mihailetschi, L.J.A. Koster, und P.W.M. Blom, "Effect of metal electrodes on the performance of polymer:fullerene bulk heterojunction solar cells," *Appl. Phys. Lett.*, 85, 2004, S. 970-972.
- [118] C.J. Brabec, S.E. Shaheen, C. Winder, N.S. Sariciftci, und P. Denk, "Effect of LiF/metal electrodes on the performance of plastic solar cells," *Appl. Phys. Lett.*, 80, 2002, S. 1288-1290.
- [119] Ma, W.;Yang, C.; Gong, X.; Lee, K.; Heeger, A.J., "Air-Stable Polymer Electronic Devices," *Adv. Mater.*, 19, 2007, S. 2445–2449.

- [120] B.V. Andersson, D.M. Huang, A.J. Moule, and O. Inganäs, "An optical spacer is no panacea for light collection in organic solar cells," *Appl. Phys. Lett.*, 94, 2009.
- [121] M. Niggemann, "Fundamental Investigations on Periodic Nanoand Microstructured Organic Solar Cells," Albert-Ludwigs-Universitaet Freiburg im Breisgau, 2005.
- [122] Z.R. Wessling RA, "Polyelectrolyte from bis(sulfonium salts)," U.S. Patent 3,401,152, 1968.
- [123] H.G. Gilch und W.L. Wheelwright, "Polymerization of alpha-halogenated p-xylenes with base," *J. Polym. Sci., Part A: Polym. Chem.*, 4, 1966, S. 1337-1349.
- [124] Y. Liu, P.M. Lahti, and F. La, "Synthesis of a regiospecific, soluble poly(2-alkoxy-1,4-phenylenevinylene)," *Polymer*, 39, 1998, S. 5241 -5244.
- [125] M. Pan, Z. Bao, and L. Yu, "Regiospecific, Functionalized Poly(phenylenevinylene) Using the Heck Coupling Reaction," *Macromolecules*, 28, 1995, S. 5151-5153.
- [126] S. Pfeiffer und H. Hörl, "Synthesis of soluble MEH-PPV and MEH-PPB by horner condensation polymerization," *Synth. Met.*, 101, 1999, S. 109 -110.
- [127] D. Gagnon, "Conductivity anisotropy in oriented poly(p-Phenylene vinylene)," *Polym. Bull.*, 12, 1984, S. 293-298.
- [128] J.D. Capistran, "Synthesis and electrical conductivity of high molecular weight poly(arylène vinlyenes)," *Polym. Prepr.*, 25, 1984, S. 282-283.
- [129] N. Tessler, N.T. Harrison, and R.H. Friend, "High Peak Brightness Polymer Light-Emitting Diodes," *Adv. Mater.*, 10, 1998, S. 64-68.
- [130] Y. Cao, I.D. Parker, G. Yu, C. Zhang, und A.J. Heeger, "Improved quantum efficiency for electroluminescence in semiconducting polymers," *Nature*, 397, 1999, S. 414-417.
- [131] J.D. Stenger-Smith, R.W. Lenz, und G. Wegner, "Spectroscopic and cyclic voltammetric studies of poly(p-phenylene vinylene) prepared from two different sulphonium salt precursor polymers," *Polymer*, 30, 1989, S. 1048-1053.
- [132] J. Roncali, "Molecular Engineering of the Band Gap of π -Conjugated Systems: Facing Technological Applications," *Macromol. Rapid Commun.*, 28, 2007, S. 1761-1775.
- [133] M.W. Suresh, C. Jain, *Conducting Organic Materials and Devices*, Elsevier, 2007.
- [134] S.E. Shaheen, C.J. Brabec, N.S. Sariciftci, F. Padinger, T. Fromherz, und J.C. Hummelen, "2.5% efficient organic plastic solar cells," *Applied Physics Letters*, 78, 2001, S. 841-843.

- [135] J.M.K. Martijn M. Wienk, "Efficient Methano[70]fullerene/MDMO-PPV Bulk Heterojunction Photovoltaic Cells," *Angew. Chem., Int. Ed.*, 42, 2003, S. 3371-3375.
- [136] G.G.M. Kwan-Yue Jen und R.L. Elsenbaumer, "Highly conducting, soluble, and environmentally-stable poly(3-alkylthiophenes)," *J. Chem. Soc., Chem. Commun.*, 1986, S. 1346-47.
- [137] T.A.R.J.R. Skotheim, Hrsg., *Handbook of Conducting Polymers*, CRC, 2007.
- [138] J. Roncali, "Conjugated poly(thiophenes): synthesis, functionalization, and applications," *Chem. Rev.*, 92, 1992, S. 711-738.
- [139] R.D. McCullough, "The Chemistry of Conducting Polythiophenes," *Adv. Mater.*, 10, 1998, S. 93-116.
- [140] A. Tsumura, H. Koezuka, und T. Ando, "Macromolecular electronic device: Field-effect transistor with a polythiophene thin film," *Appl. Phys. Lett.*, 49, 1986, S. 1210-1212.
- [141] G. Horowitz, "Organic Field-Effect Transistors," *Adv. Mater.*, 10, 1998, S. 365-377.
- [142] T.B. Singh und N.S. Sariciftci, "Progress in Plastic Electronic Devices," *Annu. Rev. Mater. Res.*, 36, 2006, S. 199-230.
- [143] J. Roncali, "Electrogenerated functional conjugated polymers as advanced electrode materials," *J. Mater. Chem.*, 9, 1999, S. 1875-1893.
- [144] B. Li, S. Santhanam, L. Schultz, M. Jeffries-EL, M.C. Iovu, G. Sauvage, J. Cooper, R. Zhang, J.C. Revelli, A.G. Kusne, J.L. Snyder, T. Kowalewski, L.E. Weiss, R.D. McCullough, G.K. Fedder, und D.N. Lambeth, "Inkjet printed chemical sensor array based on polythiophene conductive polymers," *Sens. Actuators, B*, 123, 2007, S. 651-660.
- [145] W. Ma, C. Yang, X. Gong, K. Lee, und A. Heeger, "Thermally Stable, Efficient Polymer Solar Cells with Nanoscale Control of the Interpenetrating Network Morphology," *Adv. Funct. Mater.*, 15, 2005, S. 1617-1622.
- [146] F.K. Jonas, "Neue Polythiophen-Dispersionen, ihre Herstellung und ihre Verwendung," U.S. Patent 0440957A2, 1990.
- [147] R.D. McCullough, R.D. Lowe, M. Jayaraman, und D.L. Anderson, "Design, synthesis, and control of conducting polymer architectures: structurally homogeneous poly(3-alkylthiophenes)," *J. Org. Chem.*, 58, 1993, S. 904-912.
- [148] R. Kline, M. McGehee, E. Kadnikova, J. Liu, J. Frechet, und M. Toney, "Dependence of Regioregular Poly(3-hexylthiophene) Film Morphology and Field-Effect Mobility on Molecular Weight," *Macromolecules*, 38, 2005, S. 3312-3319.

- [149] R.E. Peierls, *Quantum Theory of Solids*, Oxford University Press, 2001.
- [150] R. Hofman, *Solids and Surfaces*, VCH, 1989.
- [151] E. Bundgaard und F.C. Krebs, “Low band gap polymers for organic photovoltaics,” *Sol. Energy Mater. Sol. Cells*, 91, 2007, S. 954-985.
- [152] R. Kroon, M. Lenes, J.C. Hummelen, P.W.M. Blom, und B. de Boer, “Small Bandgap Polymers for Organic Solar Cells (Polymer Material Development in the Last 5 Years),” *Polymer Reviews*, 48, 2008, S. 531-582.
- [153] O. Inganäs, F. Zhang, und M.R. Andersson, “Alternating Polyfluorenes Collect Solar Light in Polymer Photovoltaics,” *Acc. Chem. Res.*, 42, 2009, S. 1731-1739.
- [154] M. Svensson, F. Zhang, S. Veenstra, W. Verhees, J. Hummelen, J. Kroon, O. Inganäs, und M. Andersson, “High-Performance Polymer Solar Cells of an Alternating Polyfluorene Copolymer and a Fullerene Derivative,” *Adv. Mater.*, 15, 2003, S. 988-991.
- [155] J. Chen und Y. Cao, “Development of Novel Conjugated Donor Polymers for High-Efficiency Bulk-Heterojunction Photovoltaic Devices,” *Acc. Chem. Res.*, 42, 2009, S. 1709-1718.
- [156] S.H. Park, A. Roy, S. Beaupre, S. Cho, N. Coates, J.S. Moon, D. Moses, M. Leclerc, K. Lee, und A.J. Heeger, “Bulk heterojunction solar cells with internal quantum efficiency approaching 100%,” *Nat Photon*, 3, 2009, S. 297-302.
- [157] D.D.C. Bradley, “Precursor-route poly(p-phenylenevinylene): polymer characterisation and control of electronic properties,” *J. Phys. D: Appl. Phys.*, 20, 1987, S. 1389-1410.
- [158] E. Lim, B. Jung, und H. Shim, “Synthesis and Characterization of a New Light-Emitting Fluorene-Thieno[3,2-b]thiophene-Based Conjugated Copolymer,” *Macromolecules*, 36, 2003, S. 4288-4293.
- [159] J. Huang, C. Yang, Z. Ho, D. Kekuda, M. Wu, F. Chien, P. Chen, C. Chu, und K. Ho, “Annealing effect of polymer bulk heterojunction solar cells based on polyfluorene and fullerene blend,” *Organic Electronics*, 10, 2009, S. 27-33.
- [160] O. Inganäs, F. Zhang, und M.R. Andersson, “Alternating Polyfluorenes Collect Solar Light in Polymer Photovoltaics,” *Acc. Chem. Res.*, 42, 2009, S. 1731-1739.
- [161] N. Blouin, A. Michaud, D. Gendron, S. Wakim, E. Blair, R. Neagu-Plesu, M. Belletête, G. Durocher, Y. Tao, und M. Leclerc, “Toward a Rational Design of Poly(2,7-Carbazole) Derivatives for Solar Cells,” *J. Am. Chem. Soc.*, 130, 2008, S. 732-742.

- [162] M. Prato, “[60] Fullerene chemistry for materials science applications,” *J. Mater. Chem.*, 7, 1997, S. 1097-1109.
- [163] P. Innocenzi und G. Brusatin, “Fullerene-based organic-inorganic nanocomposites and their applications,” *Chem. Mater.*, 13, 2001, S. 3126-3139.
- [164] R. Partha und J.L. Conyers, “Biomedical applications of functionalized fullerene-based nanomaterials,” *Int. J. Nanomed.*, 4, 2009, S. 261-275.
- [165] S. Bosi, T. Da Ros, G. Spalluto, und M. Prato, “Fullerene derivatives: an attractive tool for biological applications,” *Eur. J. Med. Chem.*, 38, 2003, S. 913-923.
- [166] D. Dubois, K.M. Kadish, S. Flanagan, und L.J. Wilson, “Electrochemical detection of fulleronium and highly reduced fulleride (C60⁻) ions in solution,” *J. Am. Chem. Soc.*, 113, 1991, S. 7773-7774.
- [167] A.B. Hirsch, *Fullerenes-Chemistry and Reactions*, Wiley-VCH, 2005.
- [168] N. S. Sariciftci, A. J. Heeger, “Conjugated polymer - acceptor heterojunctions, diodes, photodiodes and photovoltaic cells,” U.S. Patent WO001994005045A1, 1993.
- [169] N.S. Sariciftci, D. Braun, C. Zhang, V.I. Srdanov, A.J. Heeger, G. Stucky, und F. Wudl, “Semiconducting polymer-buckminsterfullerene heterojunctions: Diodes, photodiodes, and photovoltaic cells,” *Appl. Phys. Lett.*, 62, 1993, S. 585-587.
- [170] S. Backer, K. Sivula, D. Kavulak, und J. Frechet, “High Efficiency Organic Photovoltaics Incorporating a New Family of Soluble Fullerene Derivatives,” *Chem. Mater.*, 2007.
- [171] H. Ajie, M.M. Alvarez, S.J. Anz, R.D. Beck, F. Diederich, K. Fostiropoulos, D.R. Huffman, W. Kraetschmer, Y. Rubin, und et al, “Characterization of the soluble all-carbon molecules C60 and C70,” *J. Phys. Chem.*, 94, 1990, S. 8630–8633.
- [172] A. Krueger, *Neue Kohlenstoffmaterialien*, Vieweg, 2007.
- [173] L. Echegoyen und L.E. Echegoyen, “Electrochemistry of Fullerenes and Their Derivatives,” *Acc. Chem. Res.*, 31, 1998, S. 593-601.
- [174] D.R. Lide, *CRC Handbook of Chemistry and Physics*, CRC, 2003.
- [175] R. Waser, *Nanoelectronics and information technology*, Wiley-VCH, 2005.
- [176] T. Nakada und M. Mizutani, “18% Efficiency Cd-Free Cu(In,Ga)Se₂ Thin-Film Solar Cells\ Fabricated Using Chemical Bath Deposition (CBD)-ZnS Buffer Layers,” *Jpn. J. Appl. Phys.*, 41, 2002, S. L165-L167.

- [177] M. Bar, A. Ennaoui, J. Klaer, T. Kropp, R. Saez-Araoz, S. Lehmann, A. Grimm, I. Lauermann, C. Loreck, S. Sokoll, H. Schock, C. Fischer, M.C. Lux-Steiner, and C. Jung, "Intermixing at the heterointerface between ZnS/Zn(S,O) bilayer buffer and CuInS₂ thin film solar cell absorber," *J. Appl. Phys.*, 100, 2006, S. 064911.
- [178] B. Cushing, V. Kolesnichenko, and C. O'Connor, "Recent Advances in the Liquid-Phase Syntheses of Inorganic Nanoparticles," *Chem. Rev.*, 104, 2004, S. 3893-3946.
- [179] T. Rath, B. Kunert, R. Resel, G. Fritz-Popovski, R. Saf, and G. Trimmel, "Investigation of primary crystallite sizes in nanocrystalline ZnS powders: Comparison of microwave assisted with conventional synthesis routes," *Inorg. Chem.*, 47, 2008, S. 3014-3022.
- [180] N. Kumbhojkar, V.V. Nikesh, A. Kshirsagar, and S. Mahamuni, "Photophysical properties of ZnS nanoclusters," *J. Appl. Phys.*, 88, 2000, S. 6260-6264.
- [181] J.W. Orton, B.J. Goldsmith, J.A. Chapman, and M.J. Powell, "The mechanism of photoconductivity in polycrystalline cadmium sulphide layers," *Journal of Applied Physics*, 53, 1982, S. 1602-1614.
- [182] J.S. Meth, S.G. Zane, and J. G. Nunes, "Dual insulated-gate field-effect transistors with cadmium sulfide active layer and a laminated polymer dielectric," *Appl. Phys. Lett.*, 84, 2004, S. 2922-2924.
- [183] D.C. Reynolds, G. Leies, L.L. Antes, and R.E. Marburger, "Photovoltaic Effect in Cadmium Sulfide," *Phys. Rev.*, 96, 1954, S. 533.
- [184] R. Scheer, T. Walter, H.W. Schock, M.L. Fearheiley, and H.J. Lewerenz, "CuInS₂ based thin film solar cell with 10.2% efficiency," *Appl. Phys. Lett.*, 63, 1993, S. 3294-3296.
- [185] Y. Hashimoto, K. Takeuchi, and K. Ito, "Band alignment at CdS/CuInS₂ heterojunction," *Appl. Phys. Lett.*, 67, 1995, S. 980-982.
- [186] Y. Kang and D. Kim, "Well-aligned CdS nanorod/conjugated polymer solar cells," *Sol. Energy Mater. Sol. Cells*, 90, 2006, S. 166 -174.
- [187] H. Liao, S. Chen, and D. Liu, "In-Situ Growing CdS Single-Crystal Nanorods via P3HT Polymer as a Soft Template for Enhancing Photovoltaic Performance," *Macromolecules*, 42, 2009, S. 6558-6563.
- [188] I. Gur, N. Fromer, C. Chen, A. Kanaras, and A. Alivisatos, "Hybrid Solar Cells with Prescribed Nanoscale Morphologies Based on Hyperbranched Semiconductor Nanocrystals," *Nano Lett.*, 7, 2007, S. 409-414.
- [189] B. Sun and N.C. Greenham, "Improved efficiency of photovoltaics based on CdSe nanorods and poly(3-hexylthiophene) nanofibers," *Phys. Chem. Chem. Phys.*, 8, 2006, S. 3557-3560.

- [190] O. Madelung, "Copper indium sulfide (roquesite, CuInS₂) electronic properties," *Springer Materials - The Landolt-Börnstein Database*.
- [191] W. Shockley und H.J. Queisser, "Detailed Balance Limit of Efficiency of p-n Junction Solar Cells," *J. Appl. Phys.*, 32, 1961, S. 510-519.
- [192] S. Wagner, J.L. Shay, P. Migliorato, und H.M. Kasper, "CuInSe₂/CdS heterojunction photovoltaic detectors," *Appl. Phys. Lett.*, 25, 1974, S. 434-435.
- [193] J.L. Shay, S. Wagner, und H.M. Kasper, "Efficient CuInSe₂/CdS solar cells," *Appl. Phys. Lett.*, 27, 1975, S. 89-90.
- [194] H.J. Lewerenz, "Development of copperindiumdisulfide into a solar material," *Sol. Energy Mater. Sol. Cells*, 83, 2004, S. 395-407.
- [195] E. Arici, H. Hoppe, F. Schäffler, D. Meissner, M.A. Malik, und N.S. Sariciftci, "Hybrid solar cells based on inorganic nanoclusters and conjugated polymers," *Thin Solid Films*, 451-452, 2004, S. 612 - 618.
- [196] E.N.S. Arici, "Hybrid Solar Cells Based on Nanoparticles of CuInS₁₋₂ in Organic Matrices," *Adv. Funct. Mater.*, 13, 2003, S. 165-171.
- [197] A. Verheijen, L. Giling, und J. Bloem, "The region of existence of CuInS₂," *Mater. Res. Bull.*, 14, 1979, S. 237 -240.
- [198] H.Y. Ueng und H.L. Hwang, "The defect structure of CuInS₂. part III: Extrinsic impurities," *J. Phys. Chem. Solids*, 51, 1990, S. 11 -18.
- [199] H. Ueng und H. Hwang, "The defect structure of CuInS₂. part I: Intrinsic defects," *J. Phys. Chem. Solids*, 50, 1989, S. 1297 -1305.
- [200] H.Y. Ueng und H.L. Hwang, "The defect structure of CuInS₂. part II: Thermal annealing defects," *J. Phys. Chem. Solids*, 51, 1990, S. 1 -10.
- [201] H.J. Lewerenz und N. Dietz, "Defect identification in semiconductors by Brewster angle spectroscopy," *J. Appl. Phys.*, 73, 1993, S. 4975-4987.
- [202] W. Lehmann, "Emission Spectra of (Zn,Cd)S Phosphors," *J. Electrochem. Soc.*, 110, 1963, S. 754-758.
- [203] R. Scheer, I. Luck, M. Kanis, M. Matsui, T. Watanabe, und T. Yamamoto, "Incorporation of the doping elements Sn, N, and P in CuInS₂ thin films prepared by co-evaporation," *Thin Solid Films*, 392, 2001, S. 1 -10.
- [204] T. Yamamoto und H. Katayama-Yoshida, "P-Type Doping of the Group V Elements in CuInS₂," *Jpn. J. Appl. Phys.*, 35, 1996, S. L1562-L1565.

- [205] R.P.V. Lakshmi, R. Venugopal, D.R. Reddy, und B.K. Reddy, "Preparation and characterization of Mn doped sprayed p-CuInS₂ films," *Solid State Communications*, 82, 1992, S. 997 -1000.
- [206] T. Yamamoto, I.V. Luck, R. Scheer, und H. Katayama-Yoshida, "Differences in the electronic structure and compensation mechanism between n-type Zn- and Cd-doped CuInS₂ crystals," *Physica B*, 273-274, 1999, S. 927 -929.
- [207] S. Schorr, V. Riede, D. Spemann, und T. Doering, "Electronic band gap of Zn_{2x}(CuIn)_{1-x}X₂ solid solution series (X=?S, Se, Te)," *J. Alloys Compd.*, 414, 2006, S. 26 -30.
- [208] T. Enzenhofer, "Effect of Zn and Mg doping on CuInS₂ thin films and solar cells," *Mater. Res. Soc. Symp. Proc.*, 865, 2005, S. F11.3.1-F11.3.6.
- [209] G. Wagner, F. Fleischer, und S. Schorr, "Extension of the two-phase field in the system 2(ZnS)_x(CuInS₂)_{1-x} and structural relationship between the tetragonal and cubic phase," *J. Cryst. Growth*, 283, 2005, S. 356 -366.
- [210] M. Robbins und M.A. Miksovsky, "Preparation of and phase relationships in systems of the type ZnS--M(i)M(iii)S₂ where M(i) = Cu, Ag and M(iii) = In, Ga, Al," *J. Solid State Chem.*, 5, 1972, S. 462 -466.
- [211] L.L. Beecroft und C.K. Ober, "Nanocomposite Materials for Optical Applications," *Chem. Mater.*, 9, 1997, S. 1302-1317.
- [212] A.L. Rogach, A. Eychmuller, S.G. Hickey, und S.V. Kershaw, "Infrared-emitting colloidal nanocrystals: Synthesis, assembly, spectroscopy, and applications," *Small*, 3, 2007, S. 536-557.
- [213] P.E. Lippens und M. Lannoo, "Calculation of the band gap for small CdS and ZnS crystallites," *Phys. Rev. B*, 39, 1989.
- [214] D.D.C.B. Paul L. Burn und A. Kraft, "Precursor route chemistry and electronic properties of poly(p-phenylenevinylene), poly[(2,5-dimethyl-p-phenylene)vinylene] and poly[(2,5-dimethoxy-p-phenylene)vinylene]," *J. Chem. Soc., Perkin Trans.*, 1, 1992, S. 3225 -3231.
- [215] P. O'Brien und J. McAleese, "Developing an understanding of the processes controlling the chemical bath deposition of ZnS and CdS," *J. Mater. Chem.*, 8, 1998, S. 2309-2314.
- [216] K. Cheng, C. Huang, G. Pan, P. Chen, T. Lee, und T.C. Yang, "Physical properties of AgIn₅S₈ polycrystalline films fabricated by solution growth technique," *Mater. Chem. Phys.*, 108, 2008, S. 16 -23.
- [217] R. Williams, P. Yocom, und F. Stofko, "Preparation and properties of spherical zinc sulfide particles," *J. Colloid Interface Sci.*, 106, 1985, S. 388 -398.

- [218] R.S. Mane, B.R. Sankapal, und C.D. Lokhande, "A chemical method for the deposition of Bi₂S₃ thin films from a non-aqueous bath," *Thin Solid Films*, 359, 2000, S. 136 -140.
- [219] M. Krunk, V. Mikli, O. Bijakina, H. Rebane, A. Mere, T. Varema, und E. Mellikov, "Composition and structure of CuInS₂ films prepared by spray pyrolysis," *Thin Solid Films*, 361, 2000, S. 61-64.
- [220] D.L.P.S.L. Phillips, *Handbook of Inorganic Compounds*, CRC, 1995.
- [221] Y. Kuniya und M. Hosaka, "Vapor phase equilibria in the systems In-InCl₃ and Ga-GaCl₃," *Journal of Crystal Growth*, 28, 1975, S. 385 -391.
- [222] J.A. Dean, *LANGE'S HANDBOOK OF CHEMISTRY 15ed*, McGraw-Hill, 1999.
- [223] L. Chen, Z. Hong, G. Li, und Y. Yang, "Recent Progress in Polymer Solar Cells: Manipulation of Polymer:Fullerene Morphology and the Formation of Efficient Inverted Polymer Solar Cells," *Advanced Materials*, 21, 2009, S. 1434-1449.
- [224] J.H. Yan Yao, "Effects of Solvent Mixtures on the Nanoscale Phase Separation in Polymer Solar Cells," *Adv. Funct. Mater.*, 18, 2008, S. 1783-1789.
- [225] X.Y. J.K.J. van Duren, "Relating the Morphology of Poly(p-phenylene vinylene)/Methanofullerene Blends to Solar-Cell Performance," *Adv. Funct. Mater.*, 14, 2004, S. 425-434.
- [226] J.M.F. Barry C. Thompson, "Polymer-Fullerene Composite Solar Cells," *Angew. Chem., Int. Ed.*, 47, 2008, S. 58-77.
- [227] M. Klicker, R. Kline, D. DeLongchamp, D. Fischer, E. Lin, L. Richter, M. Chabiny, M. Toney, M. Heeney, und I. McCulloch, "Critical Role of Side-Chain Attachment Density on the Order and Device Performance of Polythiophenes," TUG, Inst. für Festkörperphysik, 2007.
- [228] B. Sun, H.J. Snaith, A.S. Dhoot, S. Westenhoff, und N.C. Greenham, "Vertically segregated hybrid blends for photovoltaic devices with improved efficiency," *Journal of Applied Physics*, 97, 2005, S. 014914.
- [229] P. Wang, A. Abrusci, H.M.P. Wong, M. Svensson, M.R. Andersson, und N.C. Greenham, "Photoinduced Charge Transfer and Efficient Solar Energy Conversion in a Blend of a Red Polyfluorene Copolymer with CdSe Nanoparticles," *Nano Letters*, 6, 2006, S. 1789-1793.
- [230] B. Sun und N.C. Greenham, "Improved efficiency of photovoltaics based on CdSe nanorods and poly(3-hexylthiophene) nanofibers.," *Phys. Chem. Chem. Phys.*, 8, 2006, S. 3557-3560.

- [231] I. Gur, N. Fromer, C. Chen, A. Kanaras, and A. Alivisatos, "Hybrid Solar Cells with Prescribed Nanoscale Morphologies Based on Hyperbranched Semiconductor Nanocrystals," *Nano Lett.*, 7, 2007, S. 409-414.
- [232] S.D. Oosterhout, M.M. Wienk, S.S. van Bavel, R. Thiedmann, L. Jan Anton Koster, J. Gilot, J. Loos, V. Schmidt, and R.A.J. Janssen, "The effect of three-dimensional morphology on the efficiency of hybrid polymer solar cells," *Nat. Mater.*, 8, 2009, S. 818-824.
- [233] W. Beek, M. Wienk, and R. Janssen, "Efficient Hybrid Solar Cells from Zinc Oxide Nanoparticles and a Conjugated Polymer," *Adv. Mater.*, 16, 2004, S. 1009–1013.
- [234] T. Zeng, H. Lo, C. Chang, Y. Lin, C. Chen, and W. Su, "Hybrid poly (3-hexylthiophene)/titanium dioxide nanorods material for solar cell applications," *Solar Energy Materials and Solar Cells*, 93, 2009, S. 952 - 957.
- [235] S. Wang, Q.Y. Gao, and J.C. Wang, "Thermodynamic analysis of decomposition of thiourea and thiourea oxides," *J. Phys. Chem. B*, 109, 2005, S. 17281-17289.
- [236] S. Wang, Q.Y. Gao, and J.C. Wang, "Thermodynamic analysis of decomposition of thiourea and thiourea oxides," *J. Phys. Chem. B*, 109, 2005, S. 17281-17289.
- [237] P.M. Schaber, J. Colson, S. Higgins, D. Thielen, B. Anspach, and J. Brauer, "Thermal decomposition (pyrolysis) of urea in an open reaction vessel," *Thermochim. Acta*, 424, 2004, S. 131 -142.
- [238] X. Hu und L. Xu, "Structure and properties of 3-alkoxy substituted polythiophene synthesized at low temperature," *Polymer*, 41, 2000, S. 9147-9154.
- [239] R. Ramani, J. Srivastava, and S. Alam, "Application of model-free kinetics to the thermal and thermo-oxidative degradation of poly(3-hexyl thiophene)," *Thermochim. Acta*, 499, 2010, S. 34 - 39.
- [240] Y. Ogawa, S. Uenishi, K. Tohyama, and K. Ito, "Preparation and properties of CuInS₂ thin films," *Sol. Energy Mater. Sol. Cells*, 35, 1994, S. 157-163.
- [241] S.D. Mittleman und R. Singh, "Electrical properties of cadmium and zinc doped CuInS₂," *Solid State Commun.*, 22, 1977, S. 659 -662.
- [242] O.V. Parasyuk, S.V. Voronyuk, L.D. Gulay, G.Y. Davidyuk, and V.O. Halka, "Phase diagram of the CuInS₂-ZnS system and some physical properties of solid solutions phases," *J. Alloys Compd.*, 348, 2003, S. 57 -64.
- [243] Greenwood und A. Earnshaw, *Chemistry of the Elements*, Butterworth Heinemann, 1997.
- [244] M. Jørgensen, K. Norrman, und F.C. Krebs, "Stability/degradation of polymer solar cells," *Solar Energy Materials and Solar Cells*, 92, 2008, S. 686-714.

- [245] T. Jeranko, H. Tributsch, N.S. Sariciftci, und J.C. Hummelen, "Patterns of efficiency and degradation of composite polymer solar cells," *Solar Energy Materials and Solar Cells*, 83, 2004, S. 247 -262.
- [246] S. Chambon, A. Rivaton, J. Gardette, und M. Firon, "Durability of MDMO-PPV and MDMO-PPV: PCBM blends under illumination in the absence of oxygen," *Solar Energy Materials and Solar Cells*, 92, 2008, S. 785-792.
- [247] A. Fischereder, Graz Technical University, 2011.
- [248] F.C. Krebs, J.E. Carle, N. Cruys-Bagger, M. Andersen, M.R. Lilliedal, M.A. Hammond, und S. Hvidt, "Lifetimes of organic photovoltaics: photochemistry, atmosphere effects and barrier layers in ITO-MEHPPV:PCBM-aluminium devices," *Sol. Energy Mater. Sol. Cells*, 86, 2005, S. 499-516.
- [249] M. Edler, "Novel Hybrid Solar Cells," Graz Technical University, 2011.
- [251] M. Wang und X. Wang, "P3HT/ZnO bulk-heterojunction solar cell sensitized by a perylene derivative," *Solar Energy Materials and Solar Cells*, 92, 2008, S. 766-771.
- [252] M. Lira-Cantu, K. Norrman, J.W. Andreasen, und F.C. Krebs, "Oxygen Release and Exchange in Niobium Oxide MEHPPV Hybrid Solar Cells," *Chemistry of Materials*, 18, 2006, S. 5684-5690.
- [253] J. Jo, D. Vak, Y. Noh, S. Kim, B. Lim, und D. Kim, "Effect of photo- and thermo-oxidative degradation on the performance of hybrid photovoltaic cells with a fluorene-based copolymer and nanocrystalline TiO₂," *Journal of Materials Chemistry*, 18, 2008, S. 654-659.
- [254] E.G. Katz und F. Krebs, "Out-door testing and long-term stability of plastic solar cells," *European Physical Journal Applied Physics*, 36, 2006, S. 307-311.
- [255] K. Lee, J. Kim, S. Park, S. Kim, S. Cho, und A. Heeger, "Air-Stable Polymer Electronic Devices," *Advanced Materials*, 19, 2007, S. 2445-2449.
- [256] S.K. Hau, H. Yip, N.S. Baek, J. Zou, K. O'Malley, und A.K. Jen, "Air-stable inverted flexible polymer solar cells using zinc oxide nanoparticles as an electron selective layer," *Appl. Phys. Lett.*, 92, 2008.
- [257] Y. Yoshida, S. Tanaka, Y. Fujita, und I. Hiromitsu, "Organic thin-film solar cells with a Cu anode: Improvement of the photovoltaic properties on aging in air," *J. Appl. Phys.*, 106, 2009.
- [258] H.C. Leventis, S.P. King, A. Sudlow, M.S. Hill, K.C. Molloy, und S.A. Haque, "Nanostructured Hybrid Polymer-Inorganic Solar Cell Active Layers Formed by Controllable in Situ Growth of Semiconducting Sulfide Networks," *Nano Lett.*, 10, 2010, S. 1253-1258.

15 List of Publications

Journal Papers:

2010:

Eugen Maier, Achim Fischereder, Wernfried Haas, Gernot Mauthner, Jörg Albering, Thomas Rath, Ferdinand Hofer, Emil J. W. List, and Gregor Trimmel: Organic-Inorganic Nanocomposite Thin Films Prepared by a Direct Formation Route; Submitted to Thin Solid Films in 02-2010

2009:

Fuchs, E. C.; Bitschnau, B.; Woisetschläger, J.; Maier, E.; Beuneu, B.; Teixeira, J.: Neutron Scattering of a Floating Heavy Water Bridge. - in: Journal of physics / D 42 (2009) S. 065502 - (4pp)

2007:

Fuchs, E. C.; Woisetschläger, J.; Gatterer, K.; Maier, E.; Pecnik, R.; Holler, G.; Eisenkölbl, H.: The floating water bridge. - in: Journal of applied physics Vol. 40 (2007) , S. 6112 – 6114

Patents:

2009:

Photoactive layers comprising quaternary and pentanary semiconducting nanoparticles; D. Meissner, T. Rath, E. Maier, G. Trimmel, F. Stelzer, A. Plessing; patent application submitted to the Austrian Patent Office, June 2, 2009.

Conference Proceedings:

2009:

Haas, W.; Zankel, A.; Rath, T.; Maier, E.; Santis Alvarez, A.; Fischereeder, A.; Trimmel, G.; Hofer, F.: Electron microscopy as a tool for morphology control in nanocomposite solar cells. - in: Materials Science (2009), S. 191 – 192; Multinational Congress on Microscopy; 9

2007:

Rath, T.; Maier, E.; Kuhlmann, J.-C.; Saf, R.; Meissner, D.; Stelzer, F.; Trimmel, G.: Application of ZnS-Nanoparticles in Photovoltaic Devices. - in: Proceedings of the 22nd European Photovoltaic Solar Energy Conference (2007), S. 72 - 74

Conference Presentations:

2009:

Maier, E.; Rath, T.; Werzer, O.; Larissegger, S.; Saf, R.; Resel, R.; Meissner, D.; Stelzer, F.; Trimmel, G.: Direct Formation of Sulfidic Nanoparticles in Semiconducting Organic Matrices for Hybrid Photovoltaics. - in: 2009 MRS Spring Meeting. San Francisco am: 16.04.2009

Maier, E.; Edler, M.; Fischereeder, A.; Fradler, C.; Haas, W.; Hofer, F.; Larissegger, S.; Mauthner, G.; Meischler, D.; Pein, A.; Rath, T.; Saf, R.; Santis Alvarez, A.; Trattinig, R.; Stelzer, F.; List, E.; Trimmel, G.: Hybrid Photovoltaic Cells via a Novel Direct Route. - in: NAWI Graz Workshop 2009. Graz am: 26.06.2009

Rath, T.; Maier, E.; Larissegger, S.; Fischereeder, A.; Edler, M.; Haas, W.; Fradler, C.; Moscher, S.; Santis Alvarez, A.; Saf, R.; Mauthner, G.; List, E.; Hofer, F.; Trimmel, G.: Application of Nanocomposite Layers of Sulfidic Nanoparticles and Electroactive Polymers in Hybrid Photovoltaics. - in: European Polymer Congress 2009 (EPF09). Graz am: 12.07.2009

Rath, T.; Maier, E.; Fischereeder, A.; Edler, M.; Haas, W.; Fradler, C.; Moscher, S.; Larissegger, S.; Santis Alvarez, A.; Meischler, D.; Saf, R.; Mauthner, G.; List, E.; Hofer, F.; Trimmel, G.: Application of Nanocomposite Layers consisting of Electroactive Polymers and Sulfidic Nanoparticles in Hybrid Photovoltaics. - in: SLONANO 2009. Ljubljana am: 19.10.2009

2008:

Maier, E.; Rath, T.; Meischler, D.; Saf, R.; Stelzer, F.; Trimmel, G.; Direct Routes towards Organic – Inorganic Semiconductor Blends. - in: 23rd European Photovoltaic Solar Energy Conference and Exhibition. Valencia am: 02.09.2008

2007:

Rath, T.; Maier, E.; Kuhlmann, J.-C.; Saf, R.; Meissner, D.; Stelzer, F.; Trimmel, G.: Application of ZnS-Nanoparticles in Photovoltaic Devices. - in: 22nd European Photovoltaic Solar Energy Conference and Exhibition. Mailand am: 03.09.2007

Fuchs, E. C.; Woisetschläger, J.; Gatterer, K.; Maier, E.; Holler, G.: Vom Cone-Jet zur Brücke: Wasser und seine seltsamen Eigenschaften im elektrischen Gleichfeld. - in: 57. Jahrestagung der Österreichischen Physikalischen Gesellschaft. Krems am: 24.09.2007

Poster Presentations:**2010:**

Eugen Maier, Wernfried Haas, Thomas Rath, Robert Saf, Ferdinand Hofer, Franz Stelzer, Dieter Meissner and Gregor Trimmel: Polymer – CuInS₂ Hybrid Solar Cells Obtained by Different In-Situ Formation Routes; in: 35th IEEE Photovoltaics Specialists Conference, Honolulu am 22.6.2010

2009:

Fischereder, A.; Maier, E.; Dunst, S.; Rath, T.; Haas, W.; Albering, J.; Hofer, F.; Trimmel, G.: Comparison of Metal Sulfides in Organic - Inorganic Nanocomposite Solar Cells by and In-Situ Formation Process. - in: E-MRS 2009. Strassbourg am: 08.06.2009

Trimmel, G.; Maier, E.; Rath, T.; Larissegger, S.; Fischereder, A.; Edler, M.; Haas, W.; Fradler, C.; Moscher, S.; Santis Alvarez, A.; Saf, R.; Mauthner, G.; List, E.; Hofer, F.: Direct Formation of Sulfidic Nanoparticles in Semiconducting Organic Matrices for Hybrid Photovoltaics. - in: E-MRS 2009. Strassbourg am: 08.06.2009

Fischereder, A.; Maier, E.; Rath, T.; Haas, W.; Hofer, F.; List, E.; Trimmel, G.: Preparation and Characterization of Metal Sulfides/ Polymer Nanocomposite Solar Cells. - in: European Polymer Congress 2009 (EPF09). Graz am: 12.07.2009

Haas, W.; Zankel, A.; Rath, T.; Maier, E.; Santis Alvarez, A.; Fischereeder, A.; Trimmel, G.; Hofer, F.: Electron microscopy as a tool for morphology control in nanocomposite solar cells. - in: Microscopy Conference MC2009. Graz am: 30.08.2009

Rath, T.; Maier, E.; Edler, M.; Fischereeder, A.; Larissegger, S.; Pein, A.; Haas, W.; Mauthner, G.; Hofer, F.; List, E.; Trimmel, G.: Organic-inorganic semiconductor blends for photovoltaic applications. - in: Nano and Photonics 2009. Mauterndorf am: 11.03.2009

Edler, M.; Fischereeder, A.; Maier, E.; Rath, T.; Haas, W.; Hofer, F.; Trimmel, G.: Comparison of Binary and Ternary Metal Sulfides as Acceptor Phase in Inorganic/Organic Hybrid Photovoltaics prepared by an In-situ Formation Process.. - in: 2009 MRS fall meeting. Boston am: 30.11.2009

Larissegger, S.; Rath, T.; Maier, E.; Edler, M.; Fischereeder, A.; Pein, A.; Haas, W.; Hofer, F.; List, E.; Trimmel, G.; Mauthner, G.: Organic-inorganic semiconductor blends for photovoltaic applications. - in: 24th European Photovoltaic Solar Energy Conference . Hamburg am: 21.09.2009

2008:

Maier, E.; Werzer, O.; Rath, T.; Larissegger, S.; Meischler, D.; Saf, R.; Resel, R.; Stelzer, F.; Trimmel, G.: Direct Formation of Organic – Inorganic Semiconductor Blends for Hybrid Photovoltaic Applications. – in: 8th International Symposium on Functional p-Electron Systems

Maier, E.; Trimmel, G.; Rath, T.; Pein, A.; Kremser, G.; Saf, R.; Stelzer, F.: Electroactive organic materials and hybrid materials for photovoltaic applications. - in: International Symposium TOWARDS ORGANIC PHOTOVOLTAICS. Linz am: 26.02.2008

2007:

Rath, T.; Maier, E.; Grießer, T.; Saf, R.; Meissner, D.; Trimmel, G.; Stelzer, F.: Size-Controlled Synthesis of ZnS-Nanoparticles in an Organic Solvent and their Application in Photovoltaic Devices. - in: MRS Spring Meeting 2007. San Francisco am: 09.04.2007

Fuchs, E. C.; Woisetschläger, J.; Gatterer, K.; Maier, E.; Eisenkölbl, H.: The floating water bridge revisited. - in: Österreichische Chemietage 2007. Klagenfurt am: 10.09.2007